Modeling and Simulation of Varistors

Modellierung und Simulation von Varistoren
Vom Fachbereich Elektrotechnik und Informationstechnik der Technischen Universität Darmstadt zur Erlangung des akademischen Grades Doktor-Ingenieur (Dr.-Ing.) genehmigte Dissertation von Dipl.-Wirtsch.-Ing. Frank Stefan Denz aus Frankfurt am Main
Tag der Einreichung: 22.04.2014, Tag der Prüfung: 08.09.2014
Darmstadt 2014 — D 17

1. Gutachten: Prof. Dr.-Ing. T. Weiland
2. Gutachten: Prof. Dr.-Ing. V. Hinrichsen

TECHNISCHE UNIVERSITÄT DARMSTADT

Modeling and Simulation of Varistors
Modellierung und Simulation von Varistoren

Genehmigte Dissertation von Dipl.-Wirtsch.-Ing. Frank Stefan Denz aus Frankfurt am Main

1. Gutachten: Prof. Dr.-Ing. T. Weiland
2. Gutachten: Prof. Dr.-Ing. V. Hinrichsen

Tag der Einreichung: 22.04.2014
Tag der Prüfung: 08.09.2014

Darmstadt — D 17

Bitte zitieren Sie dieses Dokument als:
URN: urn:nbn:de:tuda-tuprints-41971
URL: http://tuprints.ulb.tu-darmstadt.de/4197

Dieses Dokument wird bereitgestellt von tuprints,
E-Publishing-Service der TU Darmstadt
http://tuprints.ulb.tu-darmstadt.de
tuprints@ulb.tu-darmstadt.de

Erklärung laut §9 PromO

Ich versichere hiermit, dass ich die vorliegende Dissertation allein und nur unter Verwendung der angegebenen Literatur verfasst habe. Die Arbeit hat bisher noch nicht zu Prüfungszwecken gedient.

Darmstadt, den 22.04.2014

(Frank Denz)

Kurzfassung

Diese Arbeit befasst sich mit verschiedenen Problemen im Zusammenhang mit Varistoren und Mikrovaristoren, welche dank ihrer außergewöhnlichen, nichtlinearen elektrischen Leitfähigkeit zur Unterdrückung transienter Überspannungen eingesetzt werden. Diese Arbeit ist vor allem dadurch motiviert, dass man zum einen das Verhalten von Überspannungsableitern im Hochspannungsbereich simulieren möchte, zum anderen dasjenige von Mikrovaristoren für zukünftige Einsatzmöglichkeiten bei der nichtlinearen resistiven Feldsteuerung.

Die Untersuchung der Überspannungsableiter erfordert die numerische Berechnung wechselseitig gekoppelter elektrischer und thermischer Felder, wobei die Hauptschwierigkeit in der extremen Nichtlinearität des elektrischen Teilproblems zu finden ist. Zu diesem Zweck wird die Elektroquasistatik-Gleichung mittels der Finite-Elemente-Methode im Zeitbereich gelöst. Auf die Berechnung des thermisch-stationären Zustandes eines Überspannungsableiters und die Untersuchung eines Enveloppengleichungsmodells zur Simulation des Erwärmungs- und Kühlverhaltens von Ableitern wird näher eingegangen.

Diese Simulationen sind abhängig von hinreichend genauen Modellen zur Beschreibung der Materialeigenschaften. Die Schätzung der nichtlinearen Leitfähigkeit und Permittivität von Varistormaterialien ist ein essenzieller Bestandteil dieser Arbeit.

Des Weiteren werden nichtlineare Kapazitäts- und Leitfähigkeitsmatrizen eingeführt. Der hier vorgestellte Ansatz beruht auf einem Ersatzschaltungsmodell, dessen Parameter mithilfe von Feldsimulationsergebnissen bestimmt werden.

Abstract

This thesis treats various problems that arise in the context of varistors and microvaristors, which are are used for the suppression of transient overvoltages, due to their extraordinary nonlinear electrical conductivity. The present work is mainly motivated by the desire to simulate the behavior of high-voltage surge arresters used for lightning protection on the one hand and of microvaristors as materials for future applications in nonlinear resistive stress control on the other hand.

The analysis of surge arresters requires the numerical calculation of mutually-dependent electric and thermal fields, whereby the principal difficulty resides in the extreme nonlinearity of the electric problem. For this purpose, the electroquasistatics equation is solved in time domain by means of the finite-element method. The calculation of the thermally stationary state of a surge arrester and the

evaluation of an envelope equation model for simulating the heating and cooling behavior of arresters are discussed in more detail.

These simulations depend on sufficiently accurate models that describe the material properties. The estimation of nonlinear conductivity and permittivity of varistor materials is an inherent part of this thesis.

Furthermore, nonlinear capacitance and conductance matrices are introduced. The presented approach is based on an equivalent circuit model. Its parameters are determined from field-simulation results.

Contents

1 Introduction

In the last few decades scientists and engineers have increasingly turned towards computational methods to find solutions for their problems. This has been motivated by the continuous advance in computer technology. Over more than five decades the power of computers has tended to increase exponentially [68, 77]. Simultaneously, the cost of computer systems has come down to the extent that every mobile phone or washing machine can perform calculations, which few could have imagined a few years ago. When Argyris laid the foundations of the finite element method during World War II, he initially disposed of an electromechanical calculator to solve a structural design problem of an airplane with 64 linear equations [97]. Today it is possible to solve problems with hundreds of millions or more unknowns [80].

In the course of time, the numerical simulation of electromagnetic fields has become an important tool in many areas of electrical engineering from high frequency to low frequency, e.g., the design of machines and other components which are essential for generation, transport and utilization of electrical energy. In many cases, it is possible to reduce the number of experimental measurements or even to completely replace measurements by simulations. Generally, computer simulations require less time and money than the construction of new prototypes leading to faster and less expensive product development. Simulations may also offer insights, which can not be obtained from measurements. This may be the case, if the physical quantity, in which one is interested, is inaccessible from the outside or if the measurement device significantly affects the outcome of the measurement. Simulations are also nondestructive and reproducible, i.e., not influenced by uncontrolled factors. Finally, some experiments are avoided for ethical reasons (e.g., biological effects of radiation) or simply impossible.

However, there are still many problems which require a more traditional approach. The number of problems, for which perfectly appropriate methods exist, but which are simply 'too large' to be treated numerically, diminishes continuously as memory size and speed of computers increase. Yet, many problems remain outside of the scope of numerical methods either because the physical properties needed for a model are unknown or because the underlying physics can not be handled by readily available software. In these cases, *trial & error* coupled with experience and an intuitive understanding remains of greatest importance. Shifting the frontier between the experimental and simulation approaches by extending the

range of problems which can be treated numerically is one of the principal goals in computational electrodynamics.

This work is dedicated to a particular class of problems, the modeling and simulation of varistor-related problems. The initial objective was the simulation of high-voltage surge arrester behavior during lightning-surge impulses. The main functional component of such surge arresters are metal-oxide varistors (MOVs). Their behavior is not independent from temperature. During a lightning surge the thermal energy increases significantly. Therefore, the choice of a multiphysics approach combining electromagnetics, more precisely electro-quasistatics, with heat conduction is indispensable. However, the main challenge is the extreme nonlinearity of the varistor conductivity with respect to field strength. This nonlinearity leads to time steps, which are so small that the simulation of a lightning surge of several microseconds may take weeks, even when employing a computer cluster. Due to the high costs in computational power and time to obtain results of limited practical value, attention passed to other varistor-related problems, mainly connected with research group FOR 575 of the Deutsche Forschungsgemeinschaft (DFG). Ultimately, the author's work on the transient multiphysics simulation of lightning surge pulses is completely omitted from this document [16, 17].

The topics of research group FOR 575 include the research on means to filter traveling waves emanating from insulated-gate bipolar transistor (IGBT) inverters. One approach is the embedding of microvaristor materials into the insulation of wires to achieve a nonlinear resistive stress grading. As microvaristors are not fundamentally different from normal varistors, they can be simulated in the same way as normal varistor materials. However, it became apparent that the knowledge of their material properties was insufficient and that, prior to any simulation, one had to find a way to improve the quality of the material models. For that reason, a novel approach has been developed for the characterization of the nonlinear electrical properties, which is described in Ch. 5 along with the resulting observations for a specific microvaristor material.

While the transient simulation of surge arrester behavior during short current pulses is omitted, two more specialized kinds of surge arrester simulation are presented in Ch. 6. The first is concerned with the coupling of a transient electrical simulation with static heat conduction to obtain the thermally stationary state solution for a surge arrester. The second treats the applicability of an envelope equation model to simulate the heating/cooling behavior of surge arresters over time spans which are huge with respect to the period length of the exciting electrical signal.

While the two preceding chapters are dedicated to acquiring the model parameters for a simulation or the simulation itself, Ch. 7 goes one step further, towards post-

processing. It describes the generation of a nonlinear equivalent circuit model from the results of a numerical field simulation.

Finally, I wish to express my thanks to Siemens AG, the High-Voltage Laboratory at TU Darmstadt and its head, professor Hinrichsen, for kindly providing some photos and illustrations and granting me the permission to use them.

2 Surge Protection of Power Transmission Lines and Field Control

Today the protection of power transmission lines from transient overvoltages like lightning surges or switching voltages is assured by gapless metal-oxide surge arresters. Their history begins with the fortunate discovery of the nonlinear properties of zinc oxide (ZnO) ceramics by Japanese researcher Michio Matsuoka in July 1967. This discovery opened the way to the consequent development of ZnO varistors in the late 1970s [72].

The appearance of the ZnO varistor had a profound effect on surge protection, as the exploitation of their extraordinary properties made the construction of surge arresters possible that no longer require spark gaps. Due to the technical and economical advantages of the gapless metal-oxide surge arrester, this type of arrester has largely supplanted its older, silicon carbide (SiC)-based predecessors, even though some of them may still be in operation [40, 84].

The name varistor is an abbreviation of *variable resistor*. Varistors are also known as voltage-dependent resistors (VDRs), which describes perfectly their characteristic property: Their electrical conductivity depends on the applied voltage. In that respect they act like diodes. However, they do not share the asymmetry with respect to the direction of the applied voltage that is characteristic for diodes and, first of all, the energy absorption capability of MOVs is much higher than that of diodes. The combination of an extremely nonlinear electrical resistance with low leakage currents under normal operational conditions and a relatively large heat absorption capability are the principal factors which support their usage in surge-protective devices (SPDs).

In its most simple form (and without paying attention to physical units), the relationship between current I and voltage U of a varistor is described by

$$I = kU^{\alpha}, \tag{2.1}$$

with material constant k and factor of nonlinearity α [21, 24]. Alternatively, α is defined as elasticity of the function $I(U)$:

$$\alpha = \frac{\mathrm{d}I}{I} \Big/ \frac{\mathrm{d}U}{U}\,. \tag{2.2}$$

For varistors a high (maximum) value of α is desirable and seen as a figure of merit, because it guarantees a short transition interval between nonconducting and conducting state. The nonlinear electric behavior will be discussed in more detail in Sec. 3.3. The SiC varistors, which were generally used for higher voltage surge arresters before the arrival of the MOVs, exhibit a nonlinearity coefficient in the range of 2 to 7, whereas the values of early ZnO varistors laid in the range of 25 to 50. Clarke provides a range of 30 to 80 for commercially available varistors in 1999 [9]. Mahan et al. [69] report even an upper limit of 100 for the nonlinearity coefficient.

The first surge arrester devices were composed of simple spark gaps. At sufficiently high voltage differences across an air or gas gap a spark is initiated. While a spark gap limits the occurring overvoltages, it does not ensure a fast and reliable clearing of follow-up currents. As long as there is a voltage difference between the two terminals of the spark gap, current continues to flow. Therefore, an alternating current (a.c.) line-to-ground voltage signal is not interrupted until its next zero crossing.

Following the discovery of the nonlinear properties of SiC in the 1930s, this type of arrester has been succeeded by the valve-type arrester. The valve-type arrester was a significant improvement over the simple spark gap designs. It combines SiC varistors with spark gaps.

Although the elimination of the spark gaps would have been desirable to reduce the response time of the arresters, renouncing entirely on them was not possible, as the conductivity of the SiC varistors at normal operating voltages would have been too high and led to too high electric losses. In consequence, the sparkover has still been required to trigger the arrester, but the SiC varistor elements ensure a more reliable and faster clearance of follow up currents.

Only after the development of MOVs, the gapless surge arrester became possible. The concept of the gapless ZnO surge arrester, accompanied by experimental results, was presented by Matsushita and General Electric in 1977/78 [59, 86].

A group of three typical (silicone-housed) station-class high-voltage MOV surge arrresters is shown on the right-hand side of Fig. 2.1. Their design is relatively simple. As they require no spark gaps, their only electrically active element is the central resistor column. For practical purposes, arresters are divided into several units. One unit of a porcelain-housed arrester is shown in Fig. 2.2. The resistor column consists of varistors, some metallic spacers, and a supporting structure. The spacers are used to fit the length of the column to the size of the unit, ensure an evenly distributed contact pressure and operate as heat sinks [46]. In the figure a porcelain-housed surge arrester with a gas-filled volume, often air, between the central column and housing is shown. More modern arresters, especially at lower

Figure 2.1: Photograph with three two-unit silicone-housed surge arresters with grading ring standing on a pedestal. Source: Siemens AG. Printed with permission.

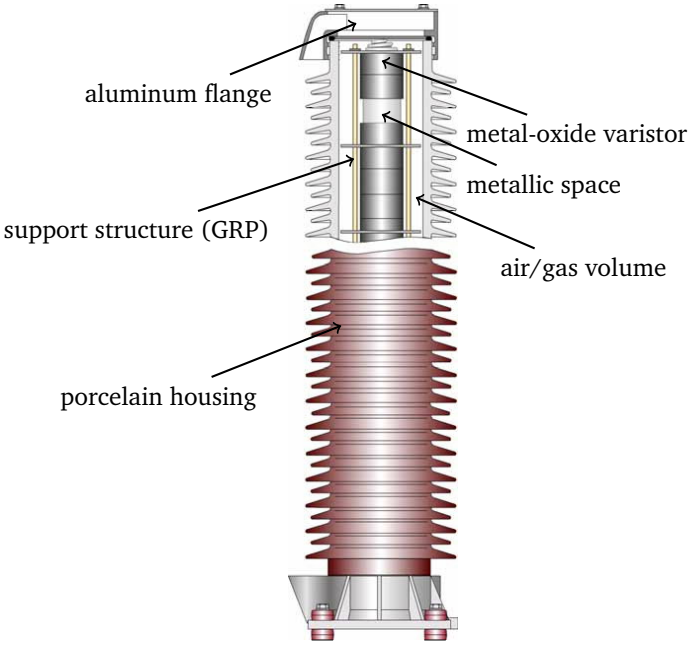

Figure 2.2: Annotated cross section of an arrester unit of a porcelain-housed surge arrester. The electrically active part is composed of the metal-oxide varistors, metallic spacers, and its glass-reinforced plastic (GRP) support structure. It is protected from the environment by a porcelain housing. At top and bottom, the active part is in contact with aluminum flanges. Between active part and the inner side of the housing a gas-filled volume is found, which is insulated from the air in the exterior. Source: Hinrichsen [46]. Adapted with permission.

voltage levels, possess a silicone-rubber housing, which is often in direct contact with the surface of the varistors by means of injection molding. Such an arrester has no gas-filled volume between active part and interior of the housing. Therefore, no attention has to be paid to gas pressure, humidity and leakage [46].

Basically, an arrester is supposed to behave like a voltage-controlled switch, which is normally closed and opens temporarily during a voltage surge to allow the transport of charges between its terminals, e.g., a transmission line and ground, and restrict the overvoltage of the line. For most of the time, the varistors show an insulator-like behavior and the resistive current is negligible. The measured current between the terminals of the arresters is predominantly capacitive. This changes during a transient voltage surge. In parallel with the voltage drop between the terminals of the arrester, the voltage at the individual varistors increases. As soon as the voltage reaches the strongly nonlinear region of the material characteristic, or equivalently the U-I-characteristic, the conductivity of the MOVs increases almost instantaneously by many orders of magnitude with response times in the nanosecond range [43, 90]. The change from insulating to conductive state of the varistors enables the electric charges to flow through the arrester towards ground, thereby restricting the extent of the possible overvoltage. The overvoltage is essentially kept from exceeding a so-called clamping voltage.

In practice, the surge arrester is designed to be operable under the maximum root mean squared (rms) voltage of a system U_s, which is higher than the nominal system voltage. Voltage U_s is defined as the *highest value of voltage which occurs under normal operating conditions at any time and at any point of the system* [50]. The peak system-to-ground voltage ($U_s/\sqrt{3}$) of such a three-phase system, plus an additional margin of at least 5 % for eventual harmonics, has to be smaller than the so-called maximum continuous operating voltage (MCOV) U_c of the arrester, i.e., the rms voltage at which the arrester can be operated continuously, demonstrated by passing standardized test procedures defined by IEC and IEEE of 30 minutes length [45]. Up to the MCOV of the arrester U_c, conductivity has to stay low to limit the heat generation by electric losses. Voltages that are higher than U_c are supposed to never occur, except for short periods during transient voltage surges. In such an event, the arrester should be highly conductive to keep the overvoltage as low as possible, but revert without delay to its original non-conductive state, once the surge has passed.

Ideally, the drop of the electric potential is equally distributed among the varistors and all of them experience the same load. However, the capacitive coupling between the varistors and ground depends on their location in the arrester because of stray capacitances between the resistor column and ground or nearby objects. The installation of one or several grading rings is intended to create a more homogeneous

field distribution along the resistor column. Even so, at elevated voltages, e.g., the test voltage for the accelerated aging procedure according to norm IEC 60099-4 [51], or for larger surge arresters the distribution becomes critical to the thermal stability of the system [39]. This problem is treated in more detail in the sections about the calculation of an equilibrium temperature distribution (Sec. 6.1) and the possible use of an envelope equation model to study thermal stability (Sec. 6.2).

Besides the question of thermal stability of a surge arrester after a surge, it is important to understand, how a surge arrester reacts during fast transients like lightning strokes or lightning test impulses. This problem has been treated by the author [17], but is excluded from this work.

In the last few years, varistors have become available in the form of microvaristor powder which opens up new fields for the application of ZnO varistor materials. In particular, the possibility of using microvaristors for nonlinear resistive field or stress control has attracted some interest.

In high-voltage engineering the stress caused by tangential electric fields at surfaces is often a critical design parameter, for example, for cable accessories, generator bar insulations or the fringes of a plate capacitor, as this causes discharges that damage the respective device.

To reduce the likelihood of discharges, one tries to influence the distribution of the electric fields by field grading. This can be done in various ways. Küchler [61] describes five types of field grading. Changing the geometry to obtain more favorable, rounded profiles, is known as geometric field grading. This approach is very common, but it significantly increases the size of the respective device. A popular and effective alternative, though not against direct current (d.c.) stress, is the so-called capacitive field grading, whereby several sheets work as a series of capacitors to modify the field in the desired way.

Field grading is also achieved by placing materials with appropriately chosen properties onto the relevant surface, which alters the field distribution. Refractive stress control is achieved by using materials with relatively high relative permittivity, whereas resistive stress control can be realized with materials of moderately high electric resistance, if their resistance is correctly chosen under consideration of the capacitance between material and insulated conductor.

When the material is not simply resistive, but possesses a nonlinear, field-dependent conductivity, one speaks of nonlinear (resistive) stress control. As the increase of local electric field strength is slowed by the increase in conductivity, nonlinear resistive stress control results in more homogeneous field distributions and lower peak field strengths inside the nonlinear material. It makes more compact designs possible than those which can be achieved with either geometric or capaci-

tive stress control. However, the higher conductivity leads also to higher Joulean heat losses.

Nonlinear resistive field control with ZnO microvaristors became an option about a decade ago, as microvaristor powders had become commercially available. Every particle of the powder is by itself a small varistor. Apart from a smaller grain size the structure is not fundamentally different from that of normal varistors, which will be described in Sec. 3.3 [19, 20].

Differences in the doping and sintering process allow for the production of microvaristor powders with largely different switching voltage and degree of nonlinearity.

Microvaristors can be used as functional fillers by embedding them in another material, e.g., a polymer material like silicone rubber. The electric properties of such a composite material are mainly determined by the type of microvaristor powder and to a lesser extent by the volume content of the microvaristors in the composite material. This offers an opportunity to tune the material properties to accommodate to specific needs.

For medium-voltage cable accessories nonlinear resistive field control is already commonly used, because of the achievable compactness of the devices and costs. However, silicon carbide or carbon black, an industrially-produced form of soot, are used as functional filling materials at present. The deficient reproducibility of the composite material properties constitutes an important disadvantage. For these materials the filler-content level has to be close to the percolation threshold, where the material properties are very sensitive [104]. If microvaristors are used instead, the material properties are more reproducible [30].

Beyond being a mere replacement for other materials in existing applications, microvaristors promise the opportunity to introduce nonlinear stress control to further areas, for which the nonlinearity of silicon carbide or carbon black has been insufficient. For example, until now nonlinear resistive stress control of cable accessories had been restricted to the medium voltage level, because for high-voltage (HV) cable accessories the heat generation due to Joulean losses would have been unacceptable. Thanks to their stronger degree of nonlinearity and high resistivity below their switching voltage, it may be possible to build more compact accessories, while heat development remains under control.

3 Physical Background

3.1 Maxwell's Equations

3.1.1 Field Equations

Maxwell's equations are the foundation of classical electrodynamics. They explain almost all phenomena related to electromagnetism apart from forces and quantum dynamical effects.

In his famous work *A Treatise on Electricity and Magnetism* of 1873, James Clerk Maxwell presents a coherent mathematical system that provides an explanation for all observed electric and magnetic phenomena and is generally known as Maxwell's equations. Apart from the until then unknown displacement current density, the equations constitute no completely new discovery, but they unite the existing knowledge contributed by various scientists into one unified mathematical model. Most notably, they predict the existence of electromagnetic waves propagating with a velocity similar to that of light, a prediction that was experimentally proved correct by H. Hertz in the late 1880s [73, 89]. Thus, light is a form of electromagnetic wave.

Today Maxwell's equations are usually presented as a set of four equations plus some auxiliary equations, which describe the influence of matter on the electromag-

Name	Differential Form	Integral Form
Gauss's law	$\operatorname{div}\mathbf{D} = \varrho$	$\oint_{\partial\Omega} \mathbf{D} \cdot \mathrm{d}\mathbf{A} = \int_{\Omega} \varrho \, \mathrm{d}\Omega$
Gauss's law for magnetism	$\operatorname{div}\mathbf{B} = 0$	$\oint_{\partial\Omega} \mathbf{B} \cdot \mathrm{d}\mathbf{A} = 0$
Faraday's law of induction	$\operatorname{curl}\mathbf{E} = -\frac{\partial \mathbf{B}}{\partial t}$	$\oint_{\partial A} \mathbf{E} \cdot \mathrm{d}\mathbf{s} = -\int_{A} \frac{\partial \mathbf{B}}{\partial t} \cdot \mathrm{d}\mathbf{A}$
Ampère's circuital law	$\operatorname{curl}\mathbf{H} = \mathbf{J} + \frac{\partial \mathbf{D}}{\partial t}$	$\oint_{\partial A} \mathbf{H} \cdot \mathrm{d}\mathbf{s} = -\int_{A} (\mathbf{J} + \frac{\partial \mathbf{D}}{\partial t}) \cdot \mathrm{d}\mathbf{A}$

Table 3.1: Maxwell's equations in differential and integral form.

netic fields. In Table 3.1 the equations are shown in differential and their equivalent integral forms (as given by Klingbeil [58]).

In these equations **D**, **B**, **E**, **H** and **J** are vector fields. The fields **D** and **E** are electric field strength and electric displacement flux density, whereas **H** and **B** are magnetic field strength and flux density. The vector **J** is known as current density.

3.1.2 Constitutive Equations

The set of Maxwell's equations is incomplete, insofar as it omits the interaction of the fields with matter. The vector fields in Maxwell's equations are not independent from each other. Their interaction depends on the environment.

In the case of vacuum, the coupling is described by the following set of constitutive equations:

$$\mathbf{D} = \varepsilon_0 \mathbf{E}, \tag{3.1}$$

$$\mathbf{B} = \mu_0 \mathbf{H}, \tag{3.2}$$

$$\mathbf{J} = \mathbf{0}. \tag{3.3}$$

The electric field strength **E** is proportional to the dielectric flux density **D**. The proportionality factor is often called electric constant and given the symbol ε_0. Similarly, the so-called permeability of free space μ_0 describes the proportionality between magnetic flux density **B** and field strength **H**.

For linear and isotropic media, one introduces material-dependent constant and scalar relative permittivity ε_r, relative permeability μ_r and electrical conductivity σ. The latter describes the relationship between current density **J** and electric field strength **E** known as Ohm's law.

$$\mathbf{D} = \varepsilon_\mathrm{r} \varepsilon_0 \mathbf{E}, \tag{3.4}$$

$$\mathbf{B} = \mu_\mathrm{r} \mu_0 \mathbf{H}, \tag{3.5}$$

$$\mathbf{J} = \sigma \mathbf{E}. \tag{3.6}$$

These relations provide a macroscopic description of the magnetic and electric field interactions with smoothed out fields [26]. They give an aggregate over volumes that are large relative to the size of individual atoms or molecules.

The relative permittivity is a consequence of the polarization of atoms and molecules. The dipole moments of the individual molecules $\mathbf{p}_n$ add up to a macroscopically averaged electric dipole moment, known as polarization density **P** [55]:

$$\mathbf{P}(\mathbf{r}, t) = \left\langle \sum_n \mathbf{p}_\mathrm{n} \delta(\mathbf{r} - \mathbf{r}_n) \right\rangle, \tag{3.7}$$

The polarization density $\mathbf{P}$ (and higher-order moments) influences the field density $\mathbf{D}$:

$$\mathbf{D} = \varepsilon_0 \mathbf{E} + \mathbf{P}. \tag{3.8}$$

For most materials and weaker field strengths, the polarization is proportional to field strength $\mathbf{E}$ and directed into the same direction. Therefore, the influence of polarization can be subsumed into a constant relative permittivity

$$\varepsilon_\mathrm{r} = 1 + P/E. \tag{3.9}$$

Sometimes the relationship between the field quantities is not sufficiently well described by a constant proportionality factor, e.g., in the case of magnetic field strength $\mathbf{H}$ and flux density $\mathbf{B}$ for ferromagnetic materials. This case is of particular practical importance, because the hysteretic behavior of ferromagnetic materials is decisive for the functioning of most electric machines. However, this work does not treat problems related to permeability.

The phenomenon of nonlinear conductivity σ and especially permittivity ε_r is of somewhat less importance, but it is essential for the discussed varistor materials. The field-strength dependence of the conductivity of a varistor is evident, as this is what defines a varistor, while the nonlinearity of relative permittivity ε_r of a varistor is shown to be of importance in Sec. 5.4.3.

$$\sigma = \sigma(\mathbf{E}), \tag{3.10}$$

$$\varepsilon_\mathrm{r} = \varepsilon_\mathrm{r}(\mathbf{E}). \tag{3.11}$$

Other cases, for which the coupling between the fields is not linear, are dispersive and anisotropic media, the presence of impressed currents or materials with observable hysteresis effects [41]. In the case of inert materials a material property, e.g., electric conductivity, depends not only on present field values, but also on the past evolution of the field. This case will become the subject of Sec. 5.5.

Inert material behavior is a common phenomenon and the observation of dispersive, i.e., frequency-dependent, material behavior is directly connected with the delayed reaction of a material with respect to the applied fields. In his book about electromagnetics, Balanis [2] even presents the constitutive equations starting directly from

$$\mathbf{D}(t) = \hat{\varepsilon}(t) * \mathbf{E}(t), \tag{3.12}$$

$$\mathbf{J}_\mathrm{r}(t) = \hat{\sigma}(t) * \mathbf{E}(t), \tag{3.13}$$

where $*$ is used as symbol for the convolution operation. This convolution incorporates the potentially inert behavior of a medium. Present flux and current depend on past electric fields.

Since convolution in time-domain is equivalent to multiplication in frequency-domain, the constitutive equations in frequency domain are

$$\mathbf{D}(j\omega) = \hat{\varepsilon}(j\omega)\mathbf{E}(j\omega), \tag{3.14}$$

$$\mathbf{J}_\mathrm{r}(j\omega) = \hat{\sigma}(j\omega)\mathbf{E}(j\omega). \tag{3.15}$$

Therefore, the above constitutive equations describe materials that are dispersive or frequency-dependent due to the delayed influence of the excitation.

This delayed response is known as relaxation. For $\mathbf{D}$ it can be written in the form

$$\mathbf{D}(t) = \varepsilon_0 \left(\varepsilon_\infty \mathbf{E}(t) + \int_0^\infty \dot{\Phi}(\tau)\mathbf{E}(t-\tau)\,\mathrm{d}\tau \right), \tag{3.16}$$

which splits the current flux density into two parts [28]. The first part is the contribution of the momentary electrical field and the second part describes the influence of past field values.

In the most simple case, $\Phi(t)$ is proportional to an exponential function with relaxation time constant τ_0:

$$\Phi(t) \propto e^{-t/\tau_0}. \tag{3.17}$$

This approach is known as Debye relaxation. The exponential decay represents the reasonable expectation of a monotonously diminishing influence of past field values.

Other models for dispersive material behavior include the Cole-Cole and Cole-Davidson relaxation model as well as their generalization, the Havriliak-Negami relaxation model

$$\varepsilon(j\omega) = \varepsilon_\infty + \frac{\varepsilon_\mathrm{s} - \varepsilon_\infty}{(1 + (j\omega\tau_0)^\alpha)^\beta}. \tag{3.18}$$

Further well-known approaches are the (stretched exponential) Kohlrausch-Williams-Watts relaxation model (with $\Phi(t) = e^{-(t/\tau_0)^\beta}$) and also the superposition of multiple Debye relaxation models.

In Sec. 5.5 the characterization of field-strength materials with inert behavior will be discussed introducing another generalization of the Debye model to field-strength dependent materials.

3.1.3 Electro-Quasistatic Approximation

It is not always necessary to solve the full set of Maxwell's equations. Sometimes it is possible to neglect some part of the equations that has only a minor influence on the solution. Whenever this is possible, the respective problem is likely much easier to solve. We are interested in a case which we call electro-quasistatics (EQS) and which is applicable to many problems of high-voltage engineering and micro-electronics [83].

In electro-quasistatics, the magnetic fields are either negligibly small or they change only slowly in time. In either case, the term $\frac{\partial \mathbf{B}}{\partial t}$ in Faraday's law becomes negligible. This implies that there are no eddy currents and that the electric field strength $\mathbf{E}$ can be regarded as irrotational. Given that $\mathbf{E}$ is irrotational, it can be represented as the gradient of a scalar potential φ:

$$\mathbf{E} = -\operatorname{grad}\varphi. \tag{3.19}$$

Applying the divergence operator to Ampère's circuital law leads to:

$$\operatorname{div}\operatorname{curl}\mathbf{H} = \operatorname{div}\left(\mathbf{J} + \frac{\partial \mathbf{D}}{\partial t}\right) \tag{3.20}$$

$$= \operatorname{div}\left(\sigma\mathbf{E} + \frac{\partial}{\partial t}(\varepsilon_\mathrm{r}\varepsilon_0\mathbf{E})\right) \tag{3.21}$$

$$= -\operatorname{div}\left((\sigma \operatorname{grad}\varphi + \frac{\partial}{\partial t}(\varepsilon_\mathrm{r}\varepsilon_0 \operatorname{grad}\varphi)\right). \tag{3.22}$$

Since $\operatorname{div}\operatorname{curl}(\cdot) = 0$, the equation becomes:

$$\operatorname{div}\left(\sigma \operatorname{grad}\varphi + \frac{\partial}{\partial t}(\varepsilon_\mathrm{r}\varepsilon_0 \operatorname{grad}\varphi)\right) = 0, \tag{3.23}$$

or:

$$\operatorname{div}(\sigma \operatorname{grad}\varphi) + \operatorname{div}\left(\frac{\partial}{\partial t}(\varepsilon_\mathrm{r}\varepsilon_0 \operatorname{grad}\varphi)\right) = 0. \tag{3.24}$$

It is this last equation that is being solved for EQS problems.

Applicability of quasistatics

While the equation used for electroquasistatics simulations has been derived in the preceding section, it is not obvious, in which cases it can be applied. One needs some indicators to decide, if it is appropriate for a specific problem or not.

At first, one can look at the energy of the electric and magnetic fields. If the energy stored in the magnetic field w_m is much smaller than the energy stored in the electric field w_e, i.e.,

$$w_\mathrm{m} \ll w_\mathrm{e}, \tag{3.25}$$

then the choice of electro-quasistatics is probably more appropriate than magneto-quasistatics [100]. The energies are given by [44]:

$$w_\mathrm{m} = \int_0^B \mathbf{H} \cdot \mathrm{d}\mathbf{B}, \tag{3.26}$$

$$w_\mathrm{e} = \int_0^D \mathbf{E} \cdot \mathrm{d}\mathbf{D}. \tag{3.27}$$

If the inverse holds true and the magnetic energy is much larger, then the problem tends to be magneto-quasistatic.

Time constants are another, more relevant help to decide whether a problem is magneto- or electro-quasistatic [91]. There are three time constants that have to be considered:

- characteristic time τ,
- dielectric relaxation time τ_relax,
- magnetic diffusion time τ_diff.

The first time constant, the characteristic time τ determines whether the full Maxwell system has to be solved or if a simplification is possible. The other two time constants decide over the kind of simplification that can be made.

If the characteristic time τ does not fulfill the condition

$$\tau \ll \frac{L}{c}, \tag{3.28}$$

then neither the electro-quasistatic nor the magneto-quasistatic simplification is valid. The characteristic time τ of the equation above is defined as

$$\tau = \frac{1}{\omega} = \frac{1}{2\pi f}, \tag{3.29}$$

where f is the frequency of a sine-like excitation. L is the typical length of the considered geometry and c is the wave propagation speed in the medium. Essentially, equation 3.28 requires that phase differences in the model are negligible, since:

$$\tau \ll \frac{L}{c} \implies \lambda \gg L, \tag{3.30}$$

with wave length $\lambda = c/f$.

The presented inequality relations follow from an estimation of the maximum relative error for the electric field strength $\mathbf{E}$, when the term $\frac{\partial}{\partial t}\mathbf{B}$ is neglected in electro-quasistatics, and of the error for the magnetic field strength $\mathbf{H}$ due to the disregard of $\frac{\partial}{\partial t}\mathbf{D}$ in magneto-quasistatics. U. van Rienen [99] deduces the condition by substituting the time derivatives by a factor $1/\tau$ and the space derivatives by $1/L$ in Faraday's law of induction and Ampère's circuital law.

The maximum estimated induced electric field strength $\mathbf{E}$ due to magnetic field strength $\mathbf{H}$ is

$$\mathbf{E} = \frac{\mu_\mathrm{r}\mu_0 L}{\tau}\mathbf{H}. \tag{3.31}$$

Similarly, Ampère's circuital law leads to

$$\mathbf{H} = \frac{\varepsilon_\mathrm{r}\varepsilon_0 L}{\tau}\mathbf{E}. \tag{3.32}$$

The degree to which an original electric field strength $\mathbf{E}$ retroacts on itself, if no simplification is made, can be estimated by inserting equation 3.32 into equation 3.31. The retroactive change of field strength $\mathbf{E}^\mathrm{r}$ becomes

$$\mathbf{E}^\mathrm{r} = \frac{\mu_\mathrm{r}\mu_0 L}{\tau}\frac{\varepsilon_\mathrm{r}\varepsilon_0 L}{\tau}\mathbf{E} = \frac{L^2}{c^2\tau^2}\mathbf{E}. \tag{3.33}$$

The electro-quasistatic approach is only valid if $\mathbf{E}^\mathrm{r} \ll \mathbf{E}$. The condition of equation 3.28 arises as a direct consequence. For magneto-quasistatics, the same argument is made, except that equation 3.31 is inserted into equation 3.32 and $\mathbf{H}^\mathrm{r} \ll \mathbf{H}$ has to be fulfilled.

The characteristic time constant τ helps to decide, if a quasistatic approach is valid. But it gives no answer to the question, if a problem is electro- or magneto-quasistatic.

There are two other time constants that have to be considered. The first one is the dielectric relaxation time τ_relax [65],

$$\tau_\mathrm{relax} = \frac{\varepsilon}{\sigma}, \tag{3.34}$$

which describes how fast a group of charges is dispersed in space:

$$\varrho(t) = \varrho_0 e^{-t/\tau_\mathrm{relax}}. \tag{3.35}$$

The dielectric relaxation time is a consequence of the continuity equation, which is itself derived from Ampère's and Gauss's law. In a homogeneous medium, one has:

$$0 = \operatorname{div}\left(\mathbf{J} + \frac{\partial}{\partial t}\mathbf{D}\right) \tag{3.36}$$

$$= \operatorname{div}\mathbf{J} + \operatorname{div}\left(\frac{\partial}{\partial t}\mathbf{D}\right) \tag{3.37}$$

$$= \operatorname{div}\left(\frac{\sigma}{\varepsilon}\mathbf{D}\right) + \operatorname{div}\left(\frac{\partial}{\partial t}\mathbf{D}\right) \tag{3.38}$$

$$= \frac{\sigma}{\varepsilon}\operatorname{div}\mathbf{D} + \frac{\partial}{\partial t}\operatorname{div}\mathbf{D} \tag{3.39}$$

$$= \frac{\sigma}{\varepsilon}\varrho + \frac{\partial \varrho}{\partial t}. \tag{3.40}$$

By solving Eq. 3.40, one obtains Eq. 3.35 with dielectric relaxation time τ_{relax}.
The other time constant is called magnetic diffusion time τ_{diff},

$$\tau_{\text{diff}} = \mu\sigma L^2, \tag{3.41}$$

with $\mu = \mu_r\mu_0$. It provides an estimate of the time that an external magnetic field needs to diffuse into a previously field-free domain of characteristic length L, e.g., a cube with side length L.

Starting from Ampère's circuital law with displacement currents and assuming a homogeneous medium, the magnetic diffusion time can be derived as follows:

$$\operatorname{curl}\mathbf{H} = \sigma\mathbf{E}, \tag{3.42}$$

$$\operatorname{curl}\operatorname{curl}\mathbf{H} = \operatorname{curl}(\sigma\mathbf{E}), \tag{3.43}$$

$$\frac{1}{\mu}\operatorname{curl}\operatorname{curl}\mathbf{B} = \sigma\operatorname{curl}\mathbf{E}, \tag{3.44}$$

$$\frac{1}{\mu}(\operatorname{grad}(\operatorname{div}\mathbf{B}) - \Delta\mathbf{B}) = -\sigma\frac{\partial\mathbf{B}}{\partial t}, \tag{3.45}$$

$$\Delta\mathbf{B} = \mu\sigma\frac{\partial\mathbf{B}}{\partial t}. \tag{3.46}$$

Faraday's law of induction and Gauss' law for magnetism are invoked in equations 3.44 and 3.45.

As previously done for characteristic time τ, the space and time derivative operators are substituted by factors $1/L$ and $1/\tau_{\text{diff}}$. It follows directly that $\tau_{\text{diff}} = \mu\sigma L^2$.

Finally, one may observe that the characteristic time τ, the dielectric relaxation time τ_{relax} and the magnetic diffusion time τ_{diff} are not mutually independent. The characteristic time τ is the geometric average of the other two time constants:

$$\tau = \sqrt{\tau_{\text{relax}} \tau_{\text{diff}}}. \tag{3.47}$$

Therefore, the dielectric relaxation time has to be much larger than the magnetic diffusion time for an electro-quasistatic problem:

$$\tau_{\text{relax}} \gg \tau \gg \tau_{\text{diff}}. \tag{3.48}$$

3.2 Heat Conduction

3.2.1 Heat Conduction Equation

In thermodynamics, heat is defined as the energy that is delivered to or dissipated from a body without work and which is caused by temperature differences [82].

The heat conduction equation, which describes the transport of heat in solids, was formulated and presented to the members of the Institut National at Paris by Jean Baptiste Joseph Fourier in 1807 [32]. Thus, it precedes Maxwell's treatise, which laid the foundations of electromagnetic theory, by 60 years.

However, it took more than fifteen years until Fourier's theory became widely accepted. In 1808 Poisson presented Fourier's results and the relevant heat conduction equation in an article in the bulletin of the Societé philomathique, but the theory was rejected by its reviewers, among them Lagrange and Laplace, due to ostensible gaps in the application of trigonometric series. Only after the publication of Fourier's book *Théorie analytique de la chaleur* in 1822 his theory gained momentum [31, 78].

In vector calculus notation, the equation can be presented as [1]

$$c_p \varrho \frac{\partial \vartheta}{\partial t} - \operatorname{div}(\lambda \operatorname{grad} \vartheta) = 0. \tag{3.49}$$

In this equation, ϑ represents temperature. The parameter c_p is the specific heat capacity per mass of a medium, ϱ is the mass density, and λ is known as thermal conductivity. The product of c_p and ϱ may be combined into volumetric heat

[1] In general, the change of heat capacity is neglected. although, in principle, the first term should be $\frac{\partial}{\partial t}\left(c_p \varrho \vartheta\right)$.

capacity $c_v = c_p \varrho$. Introducing a diffusivity $\alpha = \frac{\lambda}{c_v}$ the equation can be simplified even further [37].

Physically, the equation represents an energy balance. The term $c_p \varrho \frac{\partial \vartheta}{\partial t}$ describes the rate of change of the energy stored per volume, while the second term stands for the heat flowing into or out of the volume. Fourier's law posits that the heat flux density $\dot{\mathbf{q}}$ is proportional to the gradient of temperature:

$$\dot{\mathbf{q}} = -\lambda \operatorname{grad} \vartheta. \tag{3.50}$$

Therefore, $\operatorname{div} \dot{\mathbf{q}}$ is the net heat flow out of an infinitesimally small volume. An eventual increase or decrease of the local thermal energy has to be accompanied by the net inflow or outflow of energy through the boundary of the volume, as the original version of the heat conduction equation does not consider local heat sources.

By including local heat sources, e.g., Joulean losses, nuclear fission or exothermic chemical reaction, the heat conduction equation becomes [12]

$$c_p \varrho \frac{\partial \vartheta}{\partial t} - \operatorname{div}(\lambda \operatorname{grad} \vartheta) = \dot{w}_{\text{gen}}. \tag{3.51}$$

In this equation, $\dot{w}_{\text{gen}}$ designates heat generation density.

3.2.2 Convection and Radiation Conditions

The heat conduction equation describes the propagation of heat inside of solid materials. In fluids and gases the principal mechanism for the transportation of heat is not conduction, but either convection or radiation. Therefore, the heat conduction equation may not be applied in these cases. Its field of application is restricted to solid bodies. By contrast, convection and radiation can be neglected in the context of heat propagation in solids.

Nevertheless, convection and radiation are important boundary conditions to heat propagation problems. Additionally, one may remark that the individual heat transportation mechanisms are not mutually exclusive. Heat conduction, convection and radiation can take place at the same time, even if typically one mechanism is dominant.

Convection

Heat conduction is related to the interaction of particles in the molecular range, for example, lattice vibrations and diffusion of electrons in solids. Macroscopically there

is no displacement of matter [63]. By contrast, in fluids and gases the molecules, carrying energy in the form of enthalpy, move over much greater distances, leading to convective heat transfer.

If this heat transfer occurs naturally, one speaks of free or natural convection. Otherwise, if the heat transfer is sustained by technical means or other external factors, one speaks of forced convection [53].

In principle, the determination of the velocity field of the particles and of the convective heat transfer requires the solution of the Navier-Stokes equation. However, Newton's law of cooling is much simpler and often sufficient to describe the heat transfer between the surface of a solid and a fluid or gas:

$$\dot{q} = h\,(\vartheta - \vartheta_\infty)\,. \tag{3.52}$$

In this empirically derived equation ϑ is the temperature at the surface of the solid body and ϑ_∞ is the far-field temperature in the gas or fluid, i.e., the temperature at a sufficiently large distance from the thermal boundary layer [57]. Unlike heat conductivity λ, the heat transfer coefficient h is not exclusively material-dependent, but it depends also on geometry, solid-surface characteristics (e.g., roughness) and other flow structure aspects.

For special cases, values for the heat transfer coefficient h can be found in tables with experimental results, otherwise one has to solve some boundary layer equation or even the Navier-Stokes equations.

Radiation

Contrary to conduction and convection, radiation is not linear in temperature. Instead it increases with the fourth power, so that it tends to become the predominant mechanism of heat transfer at higher temperatures [76, 82].

It is related to changes of molecular energy levels. When an electron drops from a higher level to a lower one, a photon, or equivalently electromagnetic radiation, is emitted, mostly at wavelengths between 100 nm and 1 mm. Because of its nature as electromagnetic wave, radiative heat transfer can take place over large distances and through vacuum, in contrast to conduction and convection.

Radiative heat transfer is not easy to model, because, as stated by Modest [76], *radiative properties are usually difficult to measure and often display erratic behavior. For liquids and solids the properties normally depend only on a very thin surface layer, which may vary strongly with surface preparation and often even from day to day. All radiative properties (in particular for gases) may vary strongly with wavelength, [...].*

The heat flux density emitted from a gray surface is given by

$$\dot{q} = \epsilon \sigma_{\mathrm{SB}} \vartheta^4, \tag{3.53}$$

with emissivity ϵ, Stefan-Boltzmann constant σ_{SB} and surface temperature ϑ. A black emitter is an idealized emitter with an emissivity of one. It absorbs all radiation and emits heat radiation of a specific frequency spectrum. Real materials have a emissivity lower than one and are frequently modeled as so-called gray emitters. A gray emitter is an idealized material with the spectrum of a black emitter, but which absorbs and emits proportionally less radiation ($0 < \epsilon < 1$) [1].

In practice, one is interested in the net heat flux between a body and its environment. The net heat flux between two non-transmissive surfaces that can be considered as grey and diffuse emitters has the following form

$$\dot{Q} = \Sigma_{12}\left(T_1^4 - T_2^4\right), \tag{3.54}$$

with coefficient Σ_{12}. Non-transmissive means that the incident radiation is completely absorbed or reflected at the surface. Diffuse means that the photons are emitted in all directions with the same probability.

The coefficient Σ_{12} is a function of the two emissivity values and geometry. The value for two large parallel plates is

$$\Sigma_{12} = \frac{\sigma_{\mathrm{SB}}}{\frac{1}{\epsilon_1} + \frac{1}{\epsilon_2} - 1} A. \tag{3.55}$$

In the case of two concentric cylinders, which will arise in Sec. 6.1, the situation becomes still more complicated than for two parallel plates, as one has to take into account the kind of reflection on the surfaces. One distinguishes between specular and diffuse reflection. Specular reflection means that the incident radiation is reflected according to the law of reflection, like light at a mirror, while ideal diffuse reflection means, as explained above, that the radiation is reflected into all directions equally. For two concentric cylindrical surfaces, the value for Σ_{12} depends entirely on the kind of reflection of the outer surface, which determines the outcome of the re-reflections [48]:

$$\Sigma_{12} = \begin{cases} \frac{A_1 \sigma_{\mathrm{SB}}}{\frac{1}{\epsilon_1} + \frac{1}{\epsilon_2} - 1} & \text{if } A_2 \text{ specular} \\ \frac{A_1 \sigma_{\mathrm{SB}}}{\frac{1}{\epsilon_1} + \frac{A_1}{A_2}\left(\frac{1}{\epsilon_2} - 1\right)} & \text{if } A_2 \text{ diffuse,} \end{cases} \tag{3.56}$$

where the index 1 is used for the inner and 2 for the outer surface. It is noteworthy that the area A_2 has no influence on Σ_{12} in the case of a specular surface A_2. In practice, the real heat exchange is most often a combination of the models as a surface is rarely perfectly specular or diffuse.

3.3 Metal-Oxide Varistors

3.3.1 Microstructure, Manufacturing and Destruction Mechanisms

In Ch. 2 Metal-oxide varistors have already been introduced as materials with extraordinarily nonlinear electrical conductivity. This behavior has been observed for various metal oxides, for example, aluminum and titanium oxides, but the ZnO varistor is the oldest and by far most common type of varistor.

ZnO varistors are heterogeneous ceramic materials. They consist of about 90 % or more of ZnO. Their manufacturing process is described extensively by Einzinger [24] and more recently by Clarke [9] or Haddad [40]. First, very fine powders of almost pure ZnO and of doping materials like Bi_2O_3 are mixed and ball milled over many hours to obtain a homogeneous mixture. After addition of a binder material the aqueous slurry is calcinated at about 700 °C. During this process the dopants dissolve homogeneously in the solution.

Then the resulting granulate is compacted, molded into varistor shape and sintered in a furnace at temperatures above 1000 °C. During the sintering process the particles of the ZnO granulate grow together and form larger grains.

After sintering the material cools slowly and in controlled way to influence the chemical processes that take place at the shared surface of two grains and at the multi-grain junctions. At the boundary between two grains a thin, dopant-enriched intergranular layer forms. This inter-grain boundary is decisive for the electrical properties of the future varistor.

The final steps of the varistor manufacturing process include the coating to reduce the risk of surface sparkovers and the deposition of metals, e.g., aluminum, at the contact surfaces.

Since the beginning of research on varistors, its nonlinear electrical behavior has been attributed to the grain boundaries [71]. While the grains, which have a diameter in the order of 10 μm, fill a great part of the volume, they are composed of almost pure, crystallized ZnO, which is known to be a moderately good, linear electrical conductor ($\sigma \approx 100\,\mathrm{S/m}$). Therefore, the explanation for the nonlinear varistor behavior has be found at the boundaries. Notwithstanding the achieved progress, the actual mechanism remains not completely understood [56]. Over the years, many different mechanisms have been proposed, spanning from diffusion theory, avalanche theory and tunneling to more refined models like double Schottky barriers with thin layers or depletion layers with recombination of holes [40].

Measurements show that the grain boundaries are insulating up to a switching voltage of about 3.5 V. Published values for different dopant additives and manufacturing processes lie in the range between 2 V and 4 V [38]. Furthermore,

the conductivity may vary between different boundaries of the same varistor, as confirmed by Tao et al., who divided the grain junctions into "good" and "bad" [96]. Above switching voltage the boundary becomes conductive and the bulk conductivity approaches the value of the ZnO grains.

The varistor microstructure with its grains and boundaries of different size and electrical properties affects also the observed failure mechanisms of varistors, notably the so-called puncturing. In that case, privileged current paths develop between the contact surfaces of the varistor, where current has to pass through less, or less resistive, boundaries to reach the opposite side. Visually, this failure mode can be identified by looking for small spots on the electrodes, where the highly localized current reaches the surface. This failure mode is associated with long-duration, low-amplitude impulses and the melting of the Bi_2O_3 additive at temperatures of about 820 K [22, 85]. It has to be noted that this temperature may be reached at the grain boundaries during an impulse, while the temperature of the grains is still much lower.

If the impulse is shorter and of larger amplitude, the predominantly observed failure mode becomes cracking. In that case, thermal stress causes the varistor to crack, possibly bursting apart in pieces and requiring measures to protect nearby objects or persons. A third observed reason for failure are surface flashovers. The above mentioned coating of the surface serves to reduce the probability of this kind of failure.

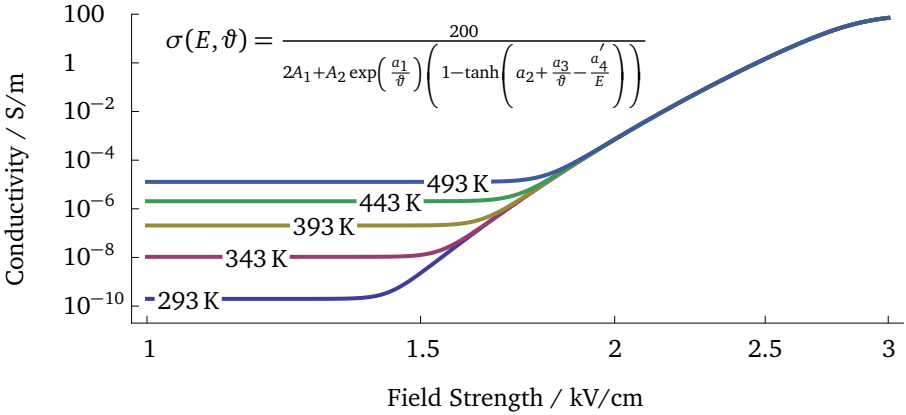

Figure 3.1: Electrical conductivity of a varistor according to an I-V characteristic by Bartkowiak [5]. The electrical conductivity varies by a factor of up to $1 \cdot 10^{12}$ at normal ambient temperatures (≈ 293 K).

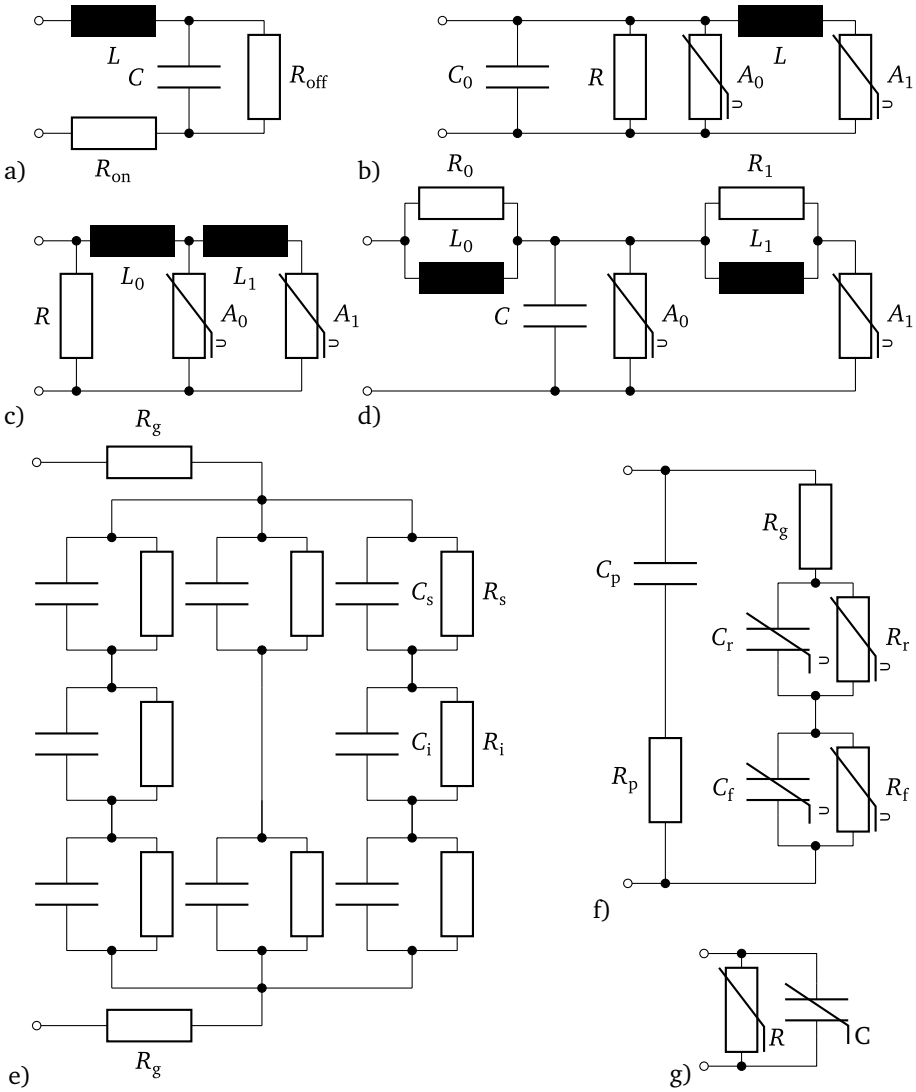

Figure 3.2: Some varistor equivalent circuit models: a) Harnden et al. (1972, [43]), b) Fernández and Díaz (2001, [29]), c) Pinceti and Giannettoni (1999, [81]), d) IEEE frequency-dependent model (1992, [52]), e) Eda two-grain model (1989, [21]), f) Einzinger (1978, [23]), g) parallel nonlinear resistor and capacitor.

The fourth and possibly most important destruction mechanism is the so-called thermal runaway. Due to the temperature dependence of the electrical conductivity of the varistors, after one or multiple voltage surges a surge arrester may reach a state, from which it does not return to normal operational conditions. Instead, the arrester continues to heat up leading to the destruction of the varistors.

3.3.2 Constitutive Relations

The macroscopic material properties of a varistor follow from its above-described microstructure. In Fig. 3.1 the electrical conductivity is shown as a function of electric field strength and temperature. The diagram is derived from an empirical I-U-characteristic presented by Bartkowiak [4]. While the characteristics of varistors vary significantly, the diagram illustrates clearly the extreme nonlinearity typical for varistors. At high field strengths the conductivity is up to $1 \cdot 10^{12}$ times higher than at low field strengths.

Another important property, which can be seen in Fig. 3.1, is the temperature dependence. The conductivity increases, as temperature rises. Equivalently, resistivity decreases. Materials with decreasing resistivity as temperature increases possess a negative temperature coefficient (NTC) and are known as NTC resistors. Often, as in the case of surge arresters, this property is undesired, as it may facilitate heat and stability problems, known as thermal runaway. The thermal stability of surge arresters is an important problem, which will be discussed in more detail in Sec. 6.2.

ZnO varistors possess also a surprisingly high relative permittivity. The macroscopic permittivity is much higher than the permittivity of its composing materials. A varistor is largely filled with ZnO which has a relative permittivity in the range of 8 to 10. The relative permittivity of the dopant materials does not exceed 25. Nevertheless, measurements show that the relative permittivity lies in the range of several hundreds. Haddad [40] or Levinson and Philipp [67] even give values in the range of 1000 to 1600 for the calculated relative permittivity from capacitance measurements. These surprisingly high values are only partially explained by the structure of the material, where the charges are separated by very thin grain boundaries. In addition, depletion layers adjacent to the intergranular layer and trapped electrons are cited as explanation.

Numerous equivalent circuit models have been proposed for modeling the electrical behavior of ZnO varistors. Fig. 3.2 presents a non-complete list of equivalent circuit models. The circuit elements labeled with A_0 or A_1 are idealized, purely resistive voltage-dependent resistors or varistors. Model *f*) of Fig. 3.2 deserves some special attention, as it does not only include a nonlinear resistor element but also a nonlinear capacitor. The results of the (micro-)varistor characterization in Sec. 5.4.3

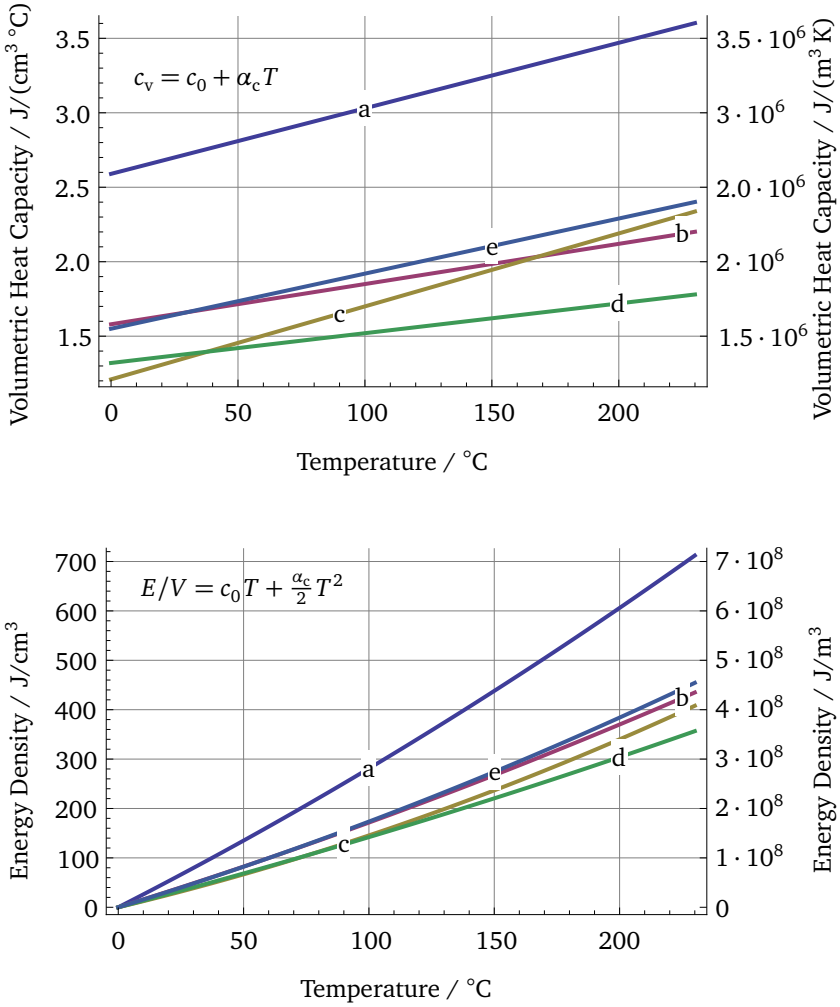

Figure 3.3: The two diagrams show the nonlinear volumetric heat capacity of some surge arrester materials as given by Lat [64] and the required energy to reach another temperature starting from 0 °C. (a: ZnO; b: porcelain, c: epoxy with SiO_2; d/e: grey/black EPR rubber.)

will show that permittivity is indeed field-strength dependent. Yet, an explicitly nonlinear capacitor is not necessary for a macroscopically nonlinear, field-dependent permittivity. At the terminals the imaginary part of the impedance is nonlinear for the other models, too. The finite element model according to the description in Sec. 4.2 corresponds to a network of parallel, nonlinear resistors and conductors. The coupling between the surfaces of the individual elements can be represented by a resistor and capacitor in parallel as shown in the model of Fig. 3.2 *g*). This model is necessarily macroscopic, as the geometric size of the elements is many times larger than the ZnO grains.

While the thermal properties of ZnO varistors are not as extraordinary as the electrical conductivity, they are nonetheless noteworthy and relevant for the functioning of varistors and surge arresters. ZnO possesses a very high thermal conductivity. It is for this reason that ZnO is used as additive in rubber tires [56]. A study on the thermal conductivity of ZnO varistors is found in Barrado et al. [3]. Another property is the high heat absorption capability of ZnO varistors. Both properties are beneficial for the operation of MOV surge arresters. In Fig. 3.3 the heat capacity of a ZnO varistor according to Lat [64] is shown along to those of various other surge arrester materials. It can be seen that ZnO exhibits a comparatively high heat capacity and absorbs, in consequence, significantly more thermal energy for the same effective increase in temperature.

4 Finite Element Method

4.1 Introduction to the Finite Element Method

The finite element method is a popular approach for the numerical solution of partial differential equations. Other well-known methods are the finite differences method [94, 103], finite integration technique [101], finite volume method [27] or boundary element method [34].

The name finite element method was introduced by Clough in 1960 [10]. However, the method can be traced back to the 1940s and the pioneering work of Hrennikoff, McHenry, Courant and others, who began to apply the method for structural analysis problems of airplanes [11, 49, 74].

Notwithstanding its successful application and the advances made by Argyris, Turner and many others, the method remained for many years a tool exclusively used in mechanical engineering. In 1965 its wider scope was remarked by Zinkiewicz [108], who wrote that the method could *be interpreted in terms of variational procedures* and that the *minimization of the total potential energy functional leads naturally to its extension to other boundary value field problems*.

He pointed explicitly to problems of heat conduction, for which Wilson and Nickell [102] applied the method in the following year. The first known application of the finite elements method in electromagnetics dates to 1969 and the analysis of a waveguide by Silvester [88].[1]

Today the finite element method is applied in many areas of physics and beyond. Its application requires the execution of several steps:

1. The physical problem has to correspond to a partial differential equation, for which a finite element formulation can be applied.

2. The computational domain is divided in non-overlapping finite elements with locally defined basis and weighting functions.

3. The entries of the local matrix and force vector are calculated for each element. A global system matrix and right-hand side vector, often called force vector, are assembled from the local data.

[1] Overviews over important contributions to the finite element method can be found in an article by Zinkiewicz [107] and several books, e.g., [13, 106].

4. After the assembly of a global system matrix and force vector, the system is solved.

5. Post-processing and output of the results.

In many cases, some of the previous steps are executed repeatedly, e.g., for a transient analysis or for mesh refinement.

When applying the finite element method, one is interested in some unknown function $u(\mathbf{x})$, which is the solution of a differential equation. Instead of the analytical solution, one searches a vector $\tilde{u}(\mathbf{x})$ to approximate the true solution:

$$u(\mathbf{x}) \approx \tilde{u}(\mathbf{x}) = \sum_i \tilde{u}_i N_i(\mathbf{x}), \tag{4.1}$$

with basis functions $N_i(\mathbf{x})$.

Depending on the choice of approach for obtaining $\tilde{u}(\mathbf{x})$, one distinguishes between variational and weighted residual method. The variational method is based on the minimization or maximization of a scalar functional Π, which reaches its extremal value for the solution of the considered differential equation. The functional Π is described by an integral of the form

$$\Pi = \int_\Omega F\left(u, \frac{\partial u}{\partial x_i}, \ldots\right) \mathrm{d}\Omega + \int_\Gamma E\left(u, \frac{\partial u}{\partial x_i}, \ldots\right) \mathrm{d}\Gamma. \tag{4.2}$$

with differential operators $F(\ldots)$ and $E(\ldots)$. Often the functional has a physical meaning, representing energy or another relevant property [106].

After insertion of Eq. 4.1 into the functional Π, the functional is differentiated with respect to all components of vector $\tilde{\mathbf{u}}$ and the result is set to zero to find a stationary point:

$$\frac{\partial \Pi}{\partial \tilde{\mathbf{u}}} = \begin{bmatrix} \frac{\partial \Pi}{\partial \tilde{u}_1} \\ \vdots \\ \frac{\partial \Pi}{\partial \tilde{u}_n} \end{bmatrix} = 0. \tag{4.3}$$

If neither the function nor its derivatives occur in powers exceeding two, $\frac{\partial \Pi}{\partial \tilde{\mathbf{u}}} = 0$ provides a linear system of equations that can be solved to get a finite elements solution of the differential equation.

Alternatively, a weighted residual method can be applied. Since this requires neither knowledge nor existence of a variational formulation, it is much more generally applicable. If the differential equation can be written as

$$\mathscr{L} u = f, \tag{4.4}$$

then the residual of its numerical solution $\tilde{u}$ is

$$r = \mathscr{L}\tilde{u} - f. \tag{4.5}$$

For the exact solution, the residual is zero everywhere. Thus, integration over an arbitrary domain Ω gives

$$\int_{\Omega} r \, \mathrm{d}\Omega = 0. \tag{4.6}$$

Obviously, the result is not affected, when the residual is weighted by a multiplicative factor w:

$$\int_{\Omega} r w \, \mathrm{d}\Omega = 0. \tag{4.7}$$

If the exact solution u is replaced by the numerical solution $\tilde{u}$, then the residual is no longer zero, except for some points in space or in exceptional cases. Still, one can require that the residual becomes zero in the weak sense of equation 4.7 for a set of specified functions w_i. In that case, the numerical solution is no longer exact, but one may expect that it is still similar to the true solution. One speaks of a weak form.

Depending on the choice of functions (or distributions) w_i, several well-known methods can be classified as weighted residual methods [6, 106]:

- (Bubnov-)Galerkin method: The same functions are chosen as basis functions for $\tilde{u}$ and weighting functions ($w_i = N_i$).
- Point collocation method: The Dirac delta distribution $\delta(\mathbf{r})$ is chosen as weighting function, i.e., the residual at certain points must be zero.
- Subdomain collocation method: The solution domain is divided into subdomains. In the j-th subdomain w_j assumes value one and is zero elsewhere.
- Least-squares method: The residual itself is used as weighting function.

Among the above-mentioned methods the Bubnov-Galerkin method is the most popular choice and is used for the simulations in the later sections. A great advantage of this method is that the mass and stiffness matrices are symmetric, which is an important property for iterative and direct solvers.

The finite element standard procedure is based on the individual treatment of each element. Assuming that a weighted residual method has been chosen, so that

one can start from Eq. 4.7 and that the residuals are linear in $\tilde{u}_i$, the condition related to the j-th weighting function can be written as

$$0 = \int_\Omega r(\tilde{u}) w_j \, \mathrm{d}\Omega \tag{4.8}$$

$$= \sum_i \int_\Omega r_i(\tilde{u}_i) w_j \, \mathrm{d}\Omega \tag{4.9}$$

$$= \sum_k \sum_i \int_{\Omega^k} r_i(\tilde{u}_i) w_j \, \mathrm{d}\Omega^k, \tag{4.10}$$

with Ω^k denoting the subdomain of the k-th element. Therefore, the integrals have to be evaluated for all combinations of (i, j, k). However, if the basis and weighting functions are zero on most elements, the computational effort is much lower. For this reason, one chooses functions that are nonzero on only a few neighboring elements. Thanks to their compactness, only a few combinations of i and j have to be evaluated for any element k. Generally, the functions $\tilde{u}_i$ and w_j are defined as polynomials inside the elements, in which they are nonzero.

Typically, the evaluation of the integrals in Eq. 4.10 is executed locally. This means that the global system of equations is not assembled directly, but that one iterates through all elements. For every element, a local element matrix A^k and vector b^k is constructed as first step. This local matrix and vector depend only on the local basis and weighting functions and are of much lower dimension than the global system. After construction of A^k and b^k, the entries are inserted into the global system matrix A and force vector b requiring a translation of the local row and column number to the global ones. The resulting global system will be sparse due to the limited coupling between the basis and weighting functions.

The following explanations for the cases of electro-quasistatics and heat conduction are presented in a way that avoids the discussion of all aspects related to individual elements. However, one has to be aware that the mass and stiffness matrices, as well as other matrices and vectors, are at first built locally, i.e., for individual elements, but that the equations are solved at the global level.

4.2 Application to Electro-Quasistatic Problems

4.2.1 Discrete Equations

According to Eq. 3.24 of Sec. 3.1.3 the electro-quasistatics equation is

$$\operatorname{div}(\sigma \operatorname{grad} \varphi) + \operatorname{div}\left(\frac{\partial}{\partial t} (\varepsilon_\mathrm{r} \varepsilon_0 \operatorname{grad} \varphi) \right) = 0. \tag{4.11}$$

Therefore, a Galerkin finite element solution is obtained by solving

$$\int_\Omega \operatorname{div}(\sigma \operatorname{grad}\varphi)\, w_i \,\mathrm{d}\Omega + \int_\Omega \operatorname{div}\left(\frac{\partial}{\partial t}(\varepsilon_\mathrm{r}\varepsilon_0 \operatorname{grad}\varphi)\right) w_i \,\mathrm{d}\Omega = 0, \tag{4.12}$$

with weighting functions w_i. By application of the divergence theorem and Stokes' theorem, the first integral, which is related to resistive currents, becomes

$$\begin{aligned}\int_\Omega \operatorname{div}(\sigma \operatorname{grad}\varphi) w_i \,\mathrm{d}\Omega & \\ = \int_\Omega \operatorname{div}(\sigma \operatorname{grad}\varphi w_i)\,\mathrm{d}\Omega - \int_\Omega \sigma\,(\operatorname{grad}\varphi)^T \operatorname{grad} w_i \,\mathrm{d}\Omega & \quad (4.13)\\ = \int_\Gamma \sigma \frac{\partial \varphi}{\partial \mathbf{n}} w_i \,\mathrm{d}\Gamma - \int_\Omega \sigma\,(\operatorname{grad}\varphi)^T \operatorname{grad} w_i \,\mathrm{d}\Omega. & \quad (4.14)\end{aligned}$$

Γ denotes the surface of space Ω and the corresponding integral represents the weighted current flowing through the surface. This integral is of importance for the imposition of boundary conditions, but for the moment, it may be ignored. It will be discussed in Sec. 4.2.3. By choosing the Bubnov-Galerkin approach ($w_i = N_i$) and substituting φ by the numerical potential $\tilde{\varphi} = \sum_j \tilde{\varphi}_j N_j$, the second integral on the right-hand side becomes

$$\sum_j \tilde{\varphi}_j \int_\Omega \sigma \left(\operatorname{grad} N_j\right)^T \operatorname{grad} N_i \,\mathrm{d}\Omega. \tag{4.15}$$

As a result of the preceding operations, one spatial differentiation has been transferred from the basis function N_j to weighting function N_i, so that the requirements on the continuity of the basis functions are reduced. The evaluation of the integral for a combination of i and j gives the coefficient of the so-called stiffness matrix K_σ in row i and column j. The name stiffness matrix and the letter K are a testimony to the origins of the finite element method in structural dynamics. Because of the interchangeability of N_i and N_j, the matrix is symmetric.

The second integral of Eq. 4.12, which is related to displacement currents, is transformed in the same way as the first integral. However, we will assume that the relative permittivity ε_r is a function of the absolute value of field strength, i.e., $\varepsilon_\mathrm{r} = \varepsilon_\mathrm{r}(|\mathbf{E}|)$. This is done with respect to the observations that will be discussed in Ch. 5 and leads to

$$\int_\Omega \operatorname{div}\left(\frac{\partial}{\partial t}\left(\varepsilon_r\varepsilon_0 \operatorname{grad}\varphi\right)\right) w_i \,\mathrm{d}\Omega \tag{4.16}$$
$$= \int_\Omega \operatorname{div}\left(\frac{\partial}{\partial t}\left(\varepsilon_r\varepsilon_0 \operatorname{grad}\varphi\right) w_i\right) \mathrm{d}\Omega - \int_\Omega \left(\frac{\partial}{\partial t}\left(\varepsilon_r\varepsilon_0 \operatorname{grad}\varphi\right)\right)^T \operatorname{grad} w_i \,\mathrm{d}\Omega$$
$$= \int_\Gamma \mathbf{n}\cdot\left(\frac{\partial}{\partial t}\left(\varepsilon_r\varepsilon_0 \operatorname{grad}\varphi\right)\right) w_i \,\mathrm{d}\Gamma - \varepsilon_0 \int_\Omega \left(\frac{\partial}{\partial t}\left(\varepsilon_r\left(|E(t)|\right)\operatorname{grad}\varphi\right)\right)^T \operatorname{grad} w_i \,\mathrm{d}\Omega.$$

Again, the surface integral may be ignored for the moment. The stiffness matrix $\mathbf{K}_\varepsilon$ is obtained from the remaining term in the same way that $\mathbf{K}_\sigma$ was obtained.

Neglecting the boundary integrals, the electro-quasistatics equation can be written in the form

$$\mathbf{K}_\varepsilon \frac{\partial \tilde{\varphi}}{\partial t} + \mathbf{K}_\sigma \tilde{\varphi} = 0, \tag{4.17}$$

or alternatively

$$\frac{\partial \tilde{\varphi}}{\partial t} = -\mathbf{K}_\sigma{}^{-1}\mathbf{K}_\sigma \tilde{\varphi}. \tag{4.18}$$

4.2.2 Solution in Time Domain

Both electric conductivity σ and relative permittivity ε_r are allowed to be nonlinear. This assumption is made to correctly simulate the behavior of (micro-)varistor materials. It has important implications on the approach for time integration.

First, the problems involving the simulation of varistor behavior are highly nonlinear. The conductivity of a varistor increases by many orders of magnitude, once a threshold value, usually called switching voltage, is reached. Relatively small changes of field strength result in a considerable change of the conductivity value. Therefore, the problem becomes stiff and one has to use an implicit time-integration scheme.

The meaning of stiffness is not precisely defined and there exists no universally accepted definition. Deuflhard [18] clarifies:

> *"There are initial value problems, for which [...] explicit one-step methods require a* too small *[length of time step]* τ_Δ *and thus* too high *an effort [...]. Such initial value problems are called* stiff *in the literature, all other initial value problems are called* nonstiff. *This* definition *has to*

remain necessarily *vague, because an assessment like* too small *can only be done pragmatically by estimating the computational costs and then taking the decision for or against a class of methods. Here, it is not the problem class that leads to the choice of a method, but a class of methods classifies the problems!*" [2]

Second, ideally one solves an initial value problem of the form

$$x' = f(t, x), \quad x(t_0) = x_0. \tag{4.19}$$

Eq. 4.18 has this form. However, it requires knowledge of matrix K_ε^{-1}. This matrix is a priori unknown and has to be obtained by inversion of K_ε. As the finite element stiffness matrix K_ε is nondiagonal, one incurs high computational costs by this operation. Furthermore, the sparsity pattern is not maintained. Unless the matrix can be reused frequently, one prefers to avoid the matrix inversion. In our case matrix K_ε is needed many times during time integration, at every time step, but it is not constant. K_ε depends on field strength and has to be recalculated frequently, as the electric fields change in time.

To avoid this problem, one can opt for solving first for $K_\varepsilon \frac{\partial \tilde{\varphi}}{\partial t}$ and then solve the resulting linear system of equations to get $\tilde{\varphi}^{n+1}$:

$$y = = \frac{\mathbf{K_\varepsilon}^n}{\Delta t}\tilde{\varphi}^n + f(\mathbf{K_\sigma}^n, \tilde{\varphi}^n, \mathbf{K_\sigma}^{n+1}, \tilde{\varphi}^{n+1}) \tag{4.20}$$

$$\frac{\mathbf{K_\varepsilon}^{n+1}}{\Delta t}\tilde{\varphi}^{n+1} = y \tag{4.21}$$

The price of avoiding the matrix inversion is the need for solving an additional system of linear equations.

There exist several methods for the implicit integration in time, which can be divided into one- and multi-step methods. Runge-Kutta methods are a prominent example of one-step methods, while Rosenbrock-Wanner methods are a popular choice among multi-step methods.

In our simulations the θ-Method was used instead, as singly-diagonally implicit Runge-Kutta (method) (SDIRK) methods, which belong to the family of Runge-Kutta

[2] Translation by the author. Original text: "Es gibt nun Anfangswertprobleme, für welche die [...] expliziten Einschrittverfahren *zu kleine* τ_Δ und damit *zu großen* Aufwand benötigen [...]. Solche Anfangswertprobleme werden in der Literatur *steif* genannt, alle anderen Anfangswertprobleme heißen *nichtsteif*. Diese *Definition* muss notwendigerweise vage bleiben, da Einschätzungen wie *zu klein* nur pragmatisch erfolgen können, indem der Rechenaufwand bewertet wird und sodann die Entscheidung für oder wider die Verfahrensklasse getroffen wird. Hier führt also nicht eine Problemklasse zur Wahl von Verfahren, sondern eine Verfahrensklasse klassifiziert die Probleme!"

methods, with or without Jacobian matrix delivered at best comparable simulation times. The θ-method can be written as

$$\frac{\tilde{\varphi}^{n+1}-\tilde{\varphi}^{n}}{\Delta t}=\theta F(t^{n+1},\tilde{\varphi}^{n+1})+(1-\theta)F(t^{n},\tilde{\varphi}^{n}), \tag{4.22}$$

or

$$\tilde{\varphi}^{n+1}=\tilde{\varphi}^{n}+\Delta t(\theta F(t^{n+1},\tilde{\varphi}^{n+1})+(1-\theta)F(t^{n},\tilde{\varphi}^{n})). \tag{4.23}$$

In this equation $\tilde{\varphi}^{n}$ is the present solution and $\tilde{\varphi}^{n+1}$ the subsequent solution after advancing in time by a time step of length Δt. A comparison with equation 4.18 shows that in our case

$$F(t^{n},\tilde{\varphi}^{n})=-(K_{\varepsilon}^{-1})^{n}K_{\sigma}^{n}\tilde{\varphi}^{n}. \tag{4.24}$$

Several choices of θ lead to methods that are known under special names. In particular, $\theta=0$ is the explicit or forward Euler method and $\theta=1$ is known as implicit or backward Euler method. The second-order accurate Crank-Nicolson method is obtained by the choice $\theta=\frac{1}{2}$ and the value $\theta=\frac{2}{3}$ is related to the name Galerkin [8].

A slightly different equation is obtained from Eq. 4.12 by integration over one time step:

$$\int_{t^{n}}^{t^{n+1}}\left(\int_{\Omega}\operatorname{div}(\sigma\operatorname{grad}\tilde{\varphi})N_{i}\mathrm{d}\Omega\right)\mathrm{d}t+\left[\int_{\Omega}\operatorname{div}(\varepsilon_{\mathrm{r}}\varepsilon_{0}\operatorname{grad}\tilde{\varphi})N_{i}\mathrm{d}\Omega\right]_{t^{n}}^{t^{n+1}}=0. \tag{4.25}$$

This leads to

$$K_{\varepsilon}^{n+1}\tilde{\varphi}^{n+1}-K_{\varepsilon}^{n}\tilde{\varphi}^{n}=-\int_{t^{n}}^{t^{n+1}}K_{\sigma}(t)\tilde{\varphi}(t)\mathrm{d}t \tag{4.26}$$

$$\approx-\Delta t\left(\theta\left(K_{\sigma}^{n+1}\tilde{\varphi}^{n+1}\right)+(1-\theta)\left(K_{\sigma}^{n}\tilde{\varphi}^{n}\right)\right). \tag{4.27}$$

The resulting scheme without boundary conditions or relaxation is

$$\left(K_{\varepsilon}^{n+1}+\theta\Delta tK_{\sigma}^{n+1}\right)\tilde{\varphi}^{n+1}=\left(K_{\varepsilon}^{n}-(1-\theta)\Delta tK_{\sigma}^{n}\right)\tilde{\varphi}^{n}. \tag{4.28}$$

4.2.3 Boundary Conditions

Up to now, boundary conditions were omitted from the presentation, notwithstanding their importance. The two basic boundary conditions for electro-quasistatics are the Dirichlet and Neumann boundary conditions.. By Senior and Volakis [87], these conditions are labeled the classical boundary conditions for scalar fields. As the Robin boundary condition is not very different and is needed anyway in the context of heat conduction, it will be included in the following presentation of electric boundary conditions.

- Dirichlet: The values of the potential $\tilde{\varphi}$ are directly imposed.
- (von) Neumann: A current density J is imposed on the boundary.
- Robin (or third-type boundary condition): A current density is imposed that depends linearly on potential $\tilde{\varphi}$.

These three types of boundary conditions are sufficient for all the problems, which will be discussed in the following. However, it has to be stated that this is no exhaustive list of boundary conditions in computational electromagnetics. For example, corresponding boundary conditions are applied with respect to the magnetic field. In addition, several boundary conditions have been developed to approximate the field close to the surface of materials, which remain intentionally outside of the computational domain, so-called impedance boundary conditions (IBCs). Another extremely important type of boundary condition are non-reflective or absorbing boundary conditions (ABCs), including the perfectly matched layer (PML). They are used to terminate the computational domain for problems of waves that propagate in unbounded regions [95].

The application of Dirichlet boundary conditions is straightforward. The potential $\tilde{\varphi}$ is known in some parts of the domain and the corresponding degrees of freedom can be eliminated from the system of equations. Sometimes one prefers not to change the dimension of the system and keeps the entry on the diagonal of the system matrix and sets the value on the right-hand side to the value needed to impose the Dirichlet condition.

The Neumann and Robin boundary conditions enter the mathematical model through the boundary integrals that result from the application of the divergence theorem in Sec. 4.2.1. Neglecting the surface integral in Eq. 4.14 is equivalent to imposing the so-called homogeneous Neumann boundary condition, whereby no current flows through the boundary.

In principle, a Neumann boundary condition prescribes the normal derivative of the unknown field on the boundary, i.e., the field strength in normal direction, but

this is almost equivalent to the practically more important imposition of a current density. Both conditions can be implemented through evaluation of the boundary integrals:

$$\int_\Gamma \sigma \frac{\partial \varphi}{\partial \mathbf{n}} w_i \, \mathrm{d}\Gamma = -\int_\Gamma \sigma \left(\mathbf{E}^\mathrm{T} \cdot \mathbf{n}\right) w_i \, \mathrm{d}\Gamma \tag{4.29}$$

$$= -\int_\Gamma \left(\mathbf{J}_\mathrm{r}^\mathrm{T} \cdot \mathbf{n}\right) w_i \, \mathrm{d}\Gamma. \tag{4.30}$$

Here, $\mathbf{E}$ designates the electric field strength and $\mathbf{J}_\mathrm{r}$ the resistive current density. The products $\mathbf{E}^\mathrm{T} \cdot \mathbf{n}$ and $\mathbf{J}_\mathrm{r}^\mathrm{T} \cdot \mathbf{n}$ are the normal components of the electric field and current density with respect to the boundary.

If the displacement current boundary integrals are disregarded, $\mathbf{J}_\mathrm{r}$ is the total current flowing through the boundary. However, formally a similar expression arises for the displacement current density $\mathbf{J}_\mathrm{c}$:

$$\int_\Gamma \frac{\partial}{\partial t} \left(\varepsilon_\mathrm{r} \varepsilon_0 \frac{\partial \varphi}{\partial \mathbf{n}} \right) w_i \, \mathrm{d}\Gamma = -\int_\Gamma \frac{\partial}{\partial t} \left(\varepsilon_\mathrm{r} \varepsilon_0 \left(\mathbf{E}^\mathrm{T} \cdot \mathbf{n} \right) \right) w_i \, \mathrm{d}\Gamma \tag{4.31}$$

$$= -\int_\Gamma \left(\mathbf{J}_\mathrm{c} \cdot \mathbf{n}\right) w_i \, \mathrm{d}\Gamma. \tag{4.32}$$

This term will be disregarded and we will assume that a current is only imposed, where its capacitive part is negligible, as is the case for the examined models. By evaluation of the integrals for all i with weighting functions that are non-zero on the concerned boundary, one obtains a vector $\mathbf{b}$, which will modify only the right-hand side of the global linear system.

The Robin boundary condition is similar to the Neumann boundary condition, but it will also influence the left-hand side as it depends on the local field. A Robin boundary condition can be written in the form:

$$\frac{\partial u}{\partial \mathbf{n}} = \alpha u + \beta. \tag{4.33}$$

This is inserted into the boundary integral:

$$\int_\Gamma \sigma \frac{\partial \tilde{\varphi}}{\partial \mathbf{n}} N_i \, \mathrm{d}\Gamma = \int_\Gamma \sigma \left(\alpha \tilde{\varphi} + \beta\right) N_i \, \mathrm{d}\Gamma \tag{4.34}$$

$$= \sum_j \tilde{\varphi}_j \int_\Gamma \sigma \alpha N_j N_i \, \mathrm{d}\Gamma + \int_\Gamma \sigma \beta N_i \, \mathrm{d}\Gamma. \tag{4.35}$$

The evaluation of equation 4.35 for all i is equivalent to

$$\mathbf{B}\tilde{\varphi} + \mathbf{b}, \tag{4.36}$$

with a Matrix $\mathbf{B}$ and vector $\mathbf{b}$. In principle, $\mathbf{B}$ is a mass matrix. Its dimension is not that of domain Ω but of its surface Γ, though.

If the boundary conditions are included into the Θ-method scheme described by equation 4.28, then the linear system of equations becomes:

$$\begin{aligned}\left(\mathbf{K}_\varepsilon{}^{n+1} + \theta\Delta t\left(\mathbf{K}_\sigma{}^{n+1} - \mathbf{B}^{n+1}\right)\right)\tilde{\varphi}^{n+1} = &\left(\mathbf{K}_\varepsilon{}^{n} - (1-\theta)\Delta t\left(\mathbf{K}_\sigma{}^{n} - \mathbf{B}^{n}\right)\right)\tilde{\varphi}^{n} \\ &+ \Delta t\left(\theta\mathbf{b}^{n+1} + (1-\theta)\mathbf{b}^{n}\right).\end{aligned} \tag{4.37}$$

In the last equation the matrices $\mathbf{B}^{(\cdot)}$ and vectors $\mathbf{b}^{(\cdot)}$ are global, however, whereas the previous equations describe an evaluation at the local level.

4.3 Application to Heat-Conduction Problems

4.3.1 Discrete Equations

In Sec.3.2.1 the relevant differential equation for heat conduction problems has been presented in the form:

$$c_p\varrho\frac{\partial\vartheta}{\partial t} - \operatorname{div}(\lambda\operatorname{grad}\vartheta) = \dot{w}_{\text{gen}}. \tag{4.38}$$

Thus, the weighted-residual Galerkin method leads to equation:

$$\int_\Omega\left(c_p\varrho\frac{\partial\vartheta}{\partial t} - \operatorname{div}(\lambda\operatorname{grad}\vartheta)\right)w_i\,\mathrm{d}\Omega = \int_\Omega \dot{w}_{\text{gen}}w_i\,\mathrm{d}\Omega. \tag{4.39}$$

This equation consists of three parts that will be considered separately:

$$\underbrace{\int_\Omega c_p\varrho\frac{\partial\vartheta}{\partial t}w_i\,\mathrm{d}\Omega}_{①} - \underbrace{\int_\Omega \operatorname{div}(\lambda\operatorname{grad}\vartheta)w_i\,\mathrm{d}\Omega}_{②} = \underbrace{\int_\Omega \dot{w}_{\text{gen}}w_i\,\mathrm{d}\Omega}_{③}. \tag{4.40}$$

The first integral ① becomes:

$$\int_\Omega c_p\varrho\frac{\partial\vartheta}{\partial t}w_i\,\mathrm{d}\Omega \approx \int_\Omega c_p\varrho\frac{\partial\left(\sum_j\tilde{\vartheta}_jN_j\right)}{\partial t}w_i\,\mathrm{d}\Omega \tag{4.41}$$

$$= \sum_j\frac{\partial\tilde{\vartheta}_j}{\partial t}\int_\Omega c_p\varrho N_jw_i\,\mathrm{d}\Omega. \tag{4.42}$$

The evaluation of this equation for all i can be written as a matrix-vector product:

$$\mathbf{M}_{c_p \varrho} \frac{\partial \tilde{\vartheta}}{\partial t}. \tag{4.43}$$

The heat capacity or mass matrix $\mathbf{M}_{c_p \varrho}$ is composed of the coefficients from evaluating the integral for the corresponding combination of i and j. If the Bubnov-Galerkin method with $w_i = N_i$ is chosen, the mass matrix is symmetric, as index i and j can be interchanged freely.

The second integral ② is similar to the integrals in Sec. 4.2.1. As before, a stiffness matrix is obtained, which will be called $\mathbf{K}_\lambda$. Depending on the boundary conditions, we may also get a matrix $\mathbf{B}$ and vector $\mathbf{b}$. The evaluation of the third integral ③ with heat sources $\dot{w}_{\text{gen}}$ leads to a vector, which we will call $\mathbf{w}_\text{V}$.

Thus, the heat conduction equation can be represented algebraically as:

$$\mathbf{M}_{c_p \varrho} \frac{\partial \tilde{\vartheta}}{\partial t} + \mathbf{K}_\lambda \tilde{\vartheta} - \mathbf{B} \tilde{\vartheta} = \mathbf{w}_\text{V} + \mathbf{b}. \tag{4.44}$$

If the θ-method is chosen for time integration, the following linear system is solved:

$$\begin{aligned} \left(\mathbf{M}_{c_p \varrho}{}^{n+1} + \Delta t \theta \left(\mathbf{K}_\lambda{}^{n+1} - \mathbf{B}^{n+1}\right)\right) \tilde{\vartheta}^{n+1} = &\left(\mathbf{M}_{c_p \varrho}{}^{n} - \Delta t (1-\theta)(\mathbf{K}_\lambda{}^{n} - \mathbf{B}^{n})\right) \tilde{\vartheta}^{n} \\ &+ \Delta t \theta \left(\mathbf{w}_\text{V}{}^{n+1} + \mathbf{b}^{n+1}\right) \\ &+ \Delta t (1-\theta)(\mathbf{w}_\text{V}{}^{n} + \mathbf{b}^{n}). \end{aligned} \tag{4.45}$$

4.3.2 Boundary Conditions

In the case of electro-quasistatics the presentation of boundary conditions had been restricted to Dirichlet, Neumann and Robin boundary condition. These conditions can also be applied to problems of heat conduction. The Dirichlet boundary condition is equivalent to imposing the temperature on some parts of the domain.

The other boundary conditions are applied through matrix $\mathbf{B}_\lambda$ and vector $\mathbf{b}$. The surface integral obtained together with $\mathbf{K}_\lambda$ is equivalent to a weighted heat flux through the surface:

$$\int_\Gamma \mathbf{n} \cdot (\lambda \operatorname{grad} \vartheta)\, w_i \,\mathrm{d}\Gamma = \int_\Gamma \mathbf{n} \cdot \dot{q}\, w_i \,\mathrm{d}\Gamma = \int_\Gamma \dot{q}_\text{n} w_i \,\mathrm{d}\Gamma. \tag{4.46}$$

Hence, the Neumann boundary condition is equivalent to the imposition of a normal heat flux density $\dot{q}_\mathrm{n}$. It results in a vector b with component b_i:

$$b_i = \int_\Gamma \dot{q}_\mathrm{n} w_i \,\mathrm{d}\Gamma. \tag{4.47}$$

The convection and radiation boundary conditions impose a normal heat flux density, too. However, the flux depends on the temperature at the boundary and is not known beforehand. Therefore, the convection boundary condition and the linearized radiation boundary condition can be considered as special cases of the Robin boundary condition.

In the case of convection, one has $\dot{q}_\mathrm{n} = h\,(\vartheta - \vartheta_\infty)$:

$$\int_\Gamma \dot{q}_\mathrm{n} w_i \,\mathrm{d}\Gamma = \int_\Gamma h\left(\tilde{\vartheta} - \vartheta_\infty\right) w_i \,\mathrm{d}\Gamma \tag{4.48}$$

$$= \sum_j \tilde{\vartheta}_j \int_\Gamma \alpha N_j w_i \,\mathrm{d}\Gamma + \int_\Gamma (-\alpha\vartheta_\infty) w_i \,\mathrm{d}\Gamma \tag{4.49}$$

If this integral is evaluated for all w_i and N_j, one obtains a linear expression that enters $\mathbf{B}_\lambda\tilde{\vartheta} + \mathbf{b}$.

The radiative heat flux boundary condition is imposed similarly:

$$\int_\Gamma \dot{q}_\mathrm{n} w_i \,\mathrm{d}\Gamma = \int_\Gamma \epsilon\sigma_\mathrm{SB}\left(\tilde{\vartheta}^4 - \vartheta_\mathrm{sur}^4\right) w_i \,\mathrm{d}\Gamma \tag{4.50}$$

$$\approx \int_\Gamma \epsilon\sigma_\mathrm{SB}\left(\left(4\,\tilde{\vartheta}^{(-1)\,3}\tilde{\vartheta} - 3\,\tilde{\vartheta}^{(-1)\,4} - \vartheta_\mathrm{sur}^4\right) w_i \,\mathrm{d}\Gamma\right. \tag{4.51}$$

$$\approx 4\epsilon\sigma_\mathrm{SB}\int_\Gamma \tilde{\vartheta}^{(-1)\,3}\tilde{\vartheta} w_i \,\mathrm{d}\Gamma - \epsilon\sigma_\mathrm{SB}\int_\Gamma \left(3\,\tilde{\vartheta}^{(-1)\,4} + \vartheta_\mathrm{sur}^4\right) w_i \,\mathrm{d}\Gamma. \tag{4.52}$$

In this equation ϑ_sur is supposed to be the temperature of the surrounding space, which determines the irradiated heat. After linearization in the second line, the radiation boundary condition has the form of a Robin boundary condition that contributes to matrix $\mathbf{B}_\lambda$ and vector $\mathbf{b}$ The temperature $\tilde{\vartheta}^{(-1)}$ designates the best known value for $\tilde{\vartheta}$, i.e., the solution of the previous iteration, when available.

5 Characterization of Nonlinear Materials

5.1 Nonlinear Capacitances

In most materials electric field strength and field density are proportional, as dielectric saturation does not occur before the breakdown of the dielectric [70]. Whenever these two fields are non-proportional, dielectric permittivity and electrical capacitance become nonlinear. Varactor diodes are the classic example of a nonlinear capacitor. They are exploited as such to tune resonant circuits. The width of their depletion layer, which determines the capacity, depends on the applied voltage [66]. Another example are ferroelectric materials, which are not only nonlinear but show in addition hysteresis effects.

Often one looks at the relationship between electric charge and voltage, their q-u-characteristic $q = f(u)$ [93]. For linear materials $f(u)$ is simply described by capacitance C as proportionality factor, i.e.:

$$q = C\,u. \tag{5.1}$$

In analogy, one can use a voltage-dependent static capacitance $C(u)$, such that

$$q(u) = C(u)\,u \tag{5.2}$$

holds for a static voltage u.

The electric current i is equal to the time derivative of the charge $\dot{q}$:

$$i = \dot{q} = \frac{\mathrm{d}\,q}{\mathrm{d}\,u}\,\frac{\mathrm{d}\,u}{\mathrm{d}\,t} = C_\mathrm{d}(u)\,\dot{u}. \tag{5.3}$$

C_d can be called differential capacitance. It describes the increase of charge for an infinitesimally small voltage increase. When materials are linear, it is equal to the static capacitance C. For nonlinear materials, C and C_d are distinct:

$$i = \frac{\mathrm{d}}{\mathrm{d}\,t}\left(C(u)\,u\right) = \frac{\mathrm{d}\,C}{\mathrm{d}\,t}\,u + C\dot{u} = \underbrace{\left(\frac{\partial\,C}{\partial\,u}\,u + C\right)}_{C_\mathrm{d}}\dot{u}. \tag{5.4}$$

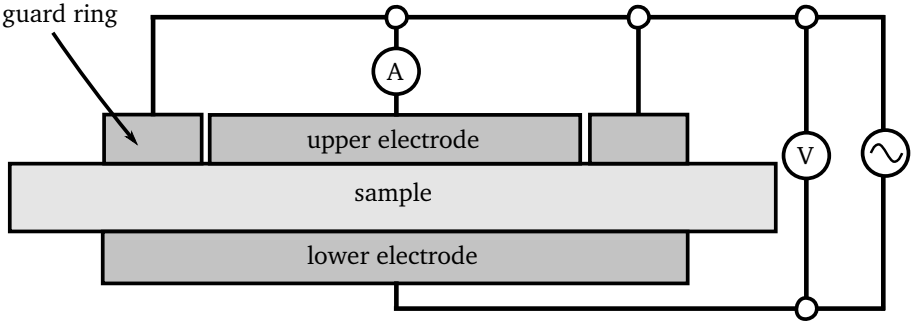

Figure 5.1: Schematic diagram of the measurement setup. The system is excited by an AC voltage signal. A guard ring surrounds the upper electrode to eliminate the influence through stray fields on the current measured by the ammeter. In consequence, the electric field is almost homogeneous and the material parameters can be calculated, when the surface area of the electrode and the thickness of the sample are known.

These definitions are not shared by all authors. For example, the above-cited book by Lerch [66], prefers to define the nonlinear capacitance C in such a way that the relationship $i = C\dot{u}$ holds. For this reason the differential capacitance C_d of Eq. 5.3 is sometimes called nonlinear capacitance. One can also find the designation small-signal capacitance.

In the context of this thesis, the definition of Eq. 5.2 is preferred. In particular, it seems to be the more natural choice, because it maintains the connection between MAXWELL's equations and circuit elements for the nonlinear case. This will be shown in the following section (Sec.5.2).

5.2 Measurement Data

The materials are characterized using voltage and current data from a measurement setup that is shown schematically in Fig. 5.1. The material sample, for example, a disk of silicone rubber filled with microvaristors (in Sec. 5.4.3), is placed between two cylindrical electrodes, which are connected to an a.c. voltage source. The upper electrode is divided into an inner electrode and a surrounding guard ring. While the current through the guard ring is affected by fringe effects, the field between the inner part of the upper electrode and the lower electrode, which determines the current measured with the ammeter, is almost homogeneous and perpendicular

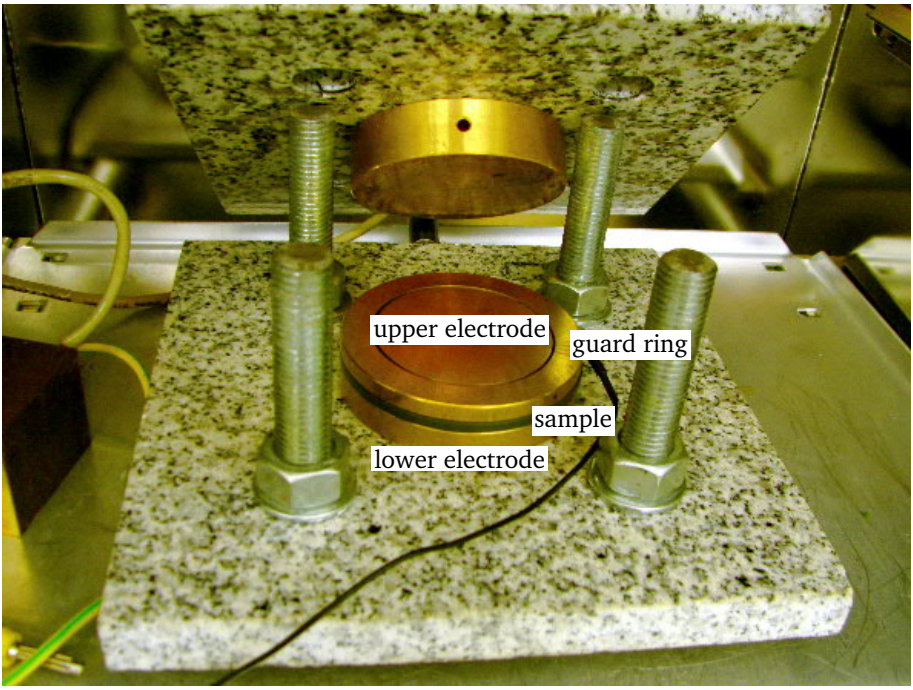

Figure 5.2: Photograph of the most relevant part of the described measurement setup. It shows the electrodes and a silicone rubber sample used for microvaristor measurements by M. Draude at the High-Voltage Laboratory. Printed with permission.

to the electrode surfaces. The guard ring configuration, which has been used for the characterization of microvaristor samples at the High Voltage Laboratory of TU Darmstadt, is shown in the photograph of Fig. 5.2.

Inside the sample, the current between the two electrodes flows in almost vertical direction. The total current density J is the sum of resistive and capacitive current density J_r and J_c:

$$J = J_\mathrm{r} + J_\mathrm{c} \tag{5.5}$$

$$= \sigma(E)E + \frac{\partial}{\partial t}\Big(\varepsilon_\mathrm{r}(E)\varepsilon_0 E\Big). \tag{5.6}$$

In this equation, both conductivity σ and relative permittivity ε_r are allowed to be nonlinear and depend on present field strength. The scalar field strengths and current densities correspond to the non-zero component of the field strength vector.

Since the field is almost homogeneous, the voltage difference u is equal to $u = Ed$ with thickness of the sample d. The measured current i corresponds to the relevant surface area A (of the upper electrode in Fig. 5.1) times current density J, i.e., $i = JA$.

Based on these assumptions one can derive the voltage-dependent conductance and capacitance:

$$i = (J_\mathrm{r} + J_\mathrm{c})A \tag{5.7}$$

$$= \left(\sigma(u/d)\,\frac{u}{d} + \frac{\partial}{\partial t}\left(\varepsilon_\mathrm{r}(u/d)\,\varepsilon_0\,\frac{u}{d}\right)\right)A \tag{5.8}$$

$$= \sigma(u/d)\,\frac{A}{d}\,u + \frac{\partial}{\partial t}\left(\varepsilon_\mathrm{r}(u/d)\;\varepsilon_0\,\frac{A}{d}\,u\right) \tag{5.9}$$

$$= G(u)\,u + \frac{\mathrm{d}}{\mathrm{d}\,t}\left(C(u)\,u\right). \tag{5.10}$$

Thus, the capacitance $C(u)$ is equal to the capacitance of a parallel-plate capacitor with surface area A and distance d between the plates. The only particularity is that the relative permittivity ε_r is allowed to depend on electric field strength:

$$C(u) = \varepsilon_\mathrm{r}(u/d)\varepsilon_0\frac{A}{d}. \tag{5.11}$$

Similarly, the conductance $G(u)$ is that of a straight wire with uniform cross-section area A and length d:

$$G(u) = \sigma(u/d)\frac{A}{d}. \tag{5.12}$$

$$\tag{5.13}$$

Inversely, if the above equations hold for $G(u)$ and $C(u)$, then:

$$\varepsilon_\mathrm{r}(E) = C(Ed)\frac{d}{\varepsilon_0 A}, \tag{5.14}$$

$$\sigma(E) = G(Ed)\frac{d}{A}. \tag{5.15}$$

These two equations show how the material properties are related to the properties of the bulk material that are measured.

5.3 Conventional Characterization Method

This section presents an approach to deduce electrical conductivity and permittivity from measurements of voltage u_i and current i_i. A measurement setup like the above-described is excited by an a.c. voltage signal. Both voltage and current are recorded. Given that the geometry corresponds to that of Sec. 5.2, the relationships of Eqs. 5.11 to 5.15 hold.

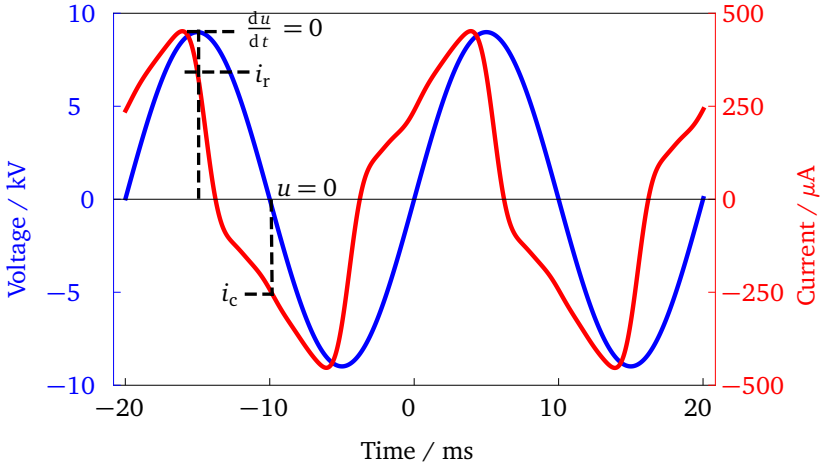

Figure 5.3: Illustration for the method of chosen points. At zeros and local extrema of the voltage signal, the current can be considered either completely resistive ($i = i_\mathrm{r}$) or capacitive ($i = i_\mathrm{r}$). The shown electric field strength (blue) and current density (red) are derived from the measured voltage and current of a silicone rubber specimen filled with microvaristors at high peak voltage.

For a linear material, the unknown values for linear conductance G and capacitance C can be derived from two data points $P_1 = (u_1, \dot{u}_1, i_1)$ and $P_2 = (u_2, \dot{u}_2, i_2)$ by solving the linear system of equations

$$i_1 = Gu_1 + C\dot{u}_1 \tag{5.16}$$

$$i_2 = Gu_2 + C\dot{u}_2, \tag{5.17}$$

with measured voltage u_i and current i_i.

This kind of approximation can be called *method of chosen points* [92]. The choice of points, for which either $u_i = 0$ or $\dot{u}_i = 0$ is fulfilled, makes the evaluation particularly simple. When voltage reaches its peak value, the entire current is resistive, implying $G = i/u$. At voltage zero-crossings, the current is exclusively capacitive, such that $C = i/\dot{u}$.

Although in practice more points might be used to reduce noise, it is in principle possible to obtain the material parameters simply by evaluating

$$G = i_1/u_1 \quad \text{with } \dot{u}_1 = 0 \tag{5.18}$$

$$C = i_2/\dot{u}_2 \quad \text{with } u_2 = 0. \tag{5.19}$$

Fig. 5.3 illustrates this approach which can still be applied in the case of a voltage-dependent electrical conductance, even though one searches a number of conductance values $G(u_i)$ that are valid for n different voltages u_i instead of one constant value G:

$$G(u_i) = i_i/u_i \qquad \text{with } \dot{u}_i = 0 \tag{5.20}$$

$$C = i_{n+1}/\dot{u}_{n+1} \qquad \text{with } u_{n+1} = 0. \tag{5.21}$$

However, the application of this method to materials with equally nonlinear permittivity leads to erroneous results like those discussed in Sec. 5.4.3. The error between observed and predicted currents due to the nonlinearity of relative permittivity amounts to:

$$i_{\text{err}} = \left(C(u) - C(0) + \frac{\partial C}{\partial u} u \right) \dot{u}. \tag{5.22}$$

The interesting point about this error is that it does not only depend on the excitation voltage, but it matters, if voltage is rising or falling. If one plots the difference between measured and calculated current as function of voltage, on may observe loops suggesting the presence of a hysteresis phenomenon, even if that is not the case.

Instead of extending the described method to materials with nonlinear conductivity and permittivity, another, more general approach was developed that will be presented in the following section (Sec. 5.4).

5.4 Least-Squares Based Method

5.4.1 Description of the Method

As alternative to the method of Sec. 5.3, another approach has been tried and resulted in more than satisfactory results for the characterization of materials with nonlinear permittivity and conductivity (see Sec. 5.4.3). In this alternative approach the material parameters are not obtained by comparison of data from individual sampling points which fulfill specific conditions. The data are instead used collectively to obtain nonlinear material characteristics that minimize statistically the error between observed and predicted currents. Although the approach proves its usefulness and is relatively trivial, the approach seems not to have been used earlier in electrical engineering. It can be compared to the identification of spatially-varying material properties that is used for many years in soil hydrodynamics, e.g., [60].

The method seeks to obtain a solution that directly satisfies:

$$i = G(u)\,u + \frac{\mathrm{d}}{\mathrm{d}\,t}\left(C(u)\,u\right). \tag{5.23}$$

Because of Equations 5.14 and 5.15 one can write equivalently:

$$J = \sigma(E)E + \frac{\partial}{\partial\, t}\left(\varepsilon_{\mathrm{r}}(E)\varepsilon_0 E\right). \tag{5.24}$$

The estimated electric conductivity $\tilde{\sigma}$ is characterized by a number of unknown coefficients $\tilde{\sigma}_k$ and their corresponding basis functions $w_k^{\sigma}(E)$:

$$\sigma \approx \tilde{\sigma} = \sum_k \tilde{\sigma}_k w_k^{\sigma}(E). \tag{5.25}$$

Analogously:

$$\varepsilon_{\mathrm{r}} \approx \tilde{\varepsilon} = \sum_k \tilde{\varepsilon}_k w_k^{\varepsilon}(E). \tag{5.26}$$

Using this approach the estimated resistive current density $\tilde{J}^{\mathrm{r}}$ becomes:

$$\tilde{J}^{\mathrm{r}} = \sum_k \tilde{\sigma}_k w_k^{\sigma}(E)\,E. \tag{5.27}$$

This can be rewritten in the form of a matrix-vector product. If the field strength was measured for n sampling moments and k coefficients are used to describe $\tilde{\sigma}_i$, then:

$$\begin{pmatrix} \tilde{J}_1^{\mathrm{r}} \\ \tilde{J}_2^{\mathrm{r}} \\ \vdots \\ \tilde{J}_n^{\mathrm{r}} \end{pmatrix} = \underbrace{\begin{pmatrix} w_1^\sigma(E_1)E_1 & w_2^\sigma(E_1)E_1 & \cdots & w_k^\sigma(E_1)E_1 \\ w_1^\sigma(E_2)E_2 & w_2^\sigma(E_2)E_2 & & \vdots \\ \vdots & & \ddots & \vdots \\ w_1^\sigma(E_n)E_n & \cdots & \cdots & w_k^\sigma(E_n)E_n \end{pmatrix}}_{[G]} \begin{pmatrix} \tilde{\sigma}_1 \\ \tilde{\sigma}_2 \\ \vdots \\ \tilde{\sigma}_k \end{pmatrix}. \tag{5.28}$$

For the capacitive current density, one has

$$\tilde{J}^{\mathrm{c}} = \frac{\partial}{\partial t}\left(\varepsilon_{\mathrm{r}}\,\varepsilon_0\,E\right) \tag{5.29}$$

$$= \frac{\partial}{\partial t}\left(\sum_k \tilde{\varepsilon}_k\, w_k^\varepsilon(E)\,\varepsilon_0\,E\right) \tag{5.30}$$

$$= \sum_k \tilde{\varepsilon}_k \left(w_k^\varepsilon(E) + \frac{\partial\, w_k^\varepsilon(x)}{\partial\, x}\bigg|_{x=E} \cdot E\right) \frac{\partial\, E}{\partial\, t}. \tag{5.31}$$

The resulting linear system stretches over more than the width of a column. Thus, it is not displayed in the same way as Eq. 5.28. Nevertheless, a comparable linear system is obtained:

$$\tilde{\mathbf{J}}^{\mathrm{c}} = \left[\mathbf{C}\right]\tilde{\varepsilon}_{\mathrm{r}}. \tag{5.32}$$

The total estimated current $\tilde{\mathbf{J}} = \tilde{\mathbf{J}}^{\mathrm{r}} + \tilde{\mathbf{J}}^{\mathrm{c}}$ becomes

$$\tilde{\mathbf{J}} = \mathbf{A}\begin{pmatrix} \tilde{\sigma} \\ \tilde{\varepsilon} \end{pmatrix}, \tag{5.33}$$

where $\mathbf{A}$ is a matrix composed of the submatrices $\left[\mathbf{G}\right]$ and $\left[\mathbf{C}\right]$, i.e., $\mathbf{A} = \left[\mathbf{G}|\mathbf{C}\right]$. The subvectors $\tilde{\sigma}$ and $\tilde{\varepsilon}$ contain the unknown coefficients, which describe the material.

The matrix $\mathbf{A}$ is asymmetric and possesses generally much more rows than columns. While the number of rows corresponds to the potentially very large number of retained sampling points, the number of columns is equal to the number of coefficients deemed necessary to characterize conductivity and relative permittivity. Furthermore, the system may be sparse, depending on the choice of basis functions.

The goal is getting a set of coefficients for $\tilde{\sigma}$ and $\tilde{\varepsilon}$, for which the difference between observed and estimated current is minimized:

$$\underset{\tilde{\sigma},\tilde{\varepsilon}}{\text{minimize}} \left\| \tilde{\mathbf{J}}(\tilde{\sigma},\tilde{\varepsilon}) - \mathbf{J}_{\text{obs}} \right\| \tag{5.34}$$

This can be achieved by solving the so-called normal equation:

$$\mathbf{A}^{\mathrm{T}}\mathbf{A}\begin{pmatrix}\tilde{\sigma}\\ \tilde{\varepsilon}\end{pmatrix} = \mathbf{A}^{\mathrm{T}}\mathbf{J}, \tag{5.35}$$

which provides an ordinary least squares (OLS) estimate of the coefficients [36, 98]. In practice, one often prefers not to solve this equation and uses a singular value decomposition (SVD) or QR decomposition of matrix **A**, because of the increased condition number of the normal equation.

5.4.2 Implementation

The implementation of this least-squares approach is based on the further assumption that the material parameters do not depend on the direction of the electric field, but only on its absolute value. Furthermore, non-uniform B-splines, or basis splines, of arbitrary order were chosen as basis functions. Following de Boor [14, 15], the B-spline of order 1 for a sequence of knots $x := (x_i)$ is defined by

$$B_{i1}(x) := \begin{cases} 1, & \text{if } x_i \le x < x_{i+1} \text{ or } x = \max_j(x_j) \\ 0, & \text{otherwise.} \end{cases} \tag{5.36}$$

B-splines of higher order k can be constructed through the recurrence relation:

$$B_{ik} := \frac{x - x_i}{x_{i+k-1} - x_i} B_{i(k-1)} + \frac{x_{i+k-1} - x}{x_{i+k-1} - x_i} B_{(i+1)(k-1)}. \tag{5.37}$$

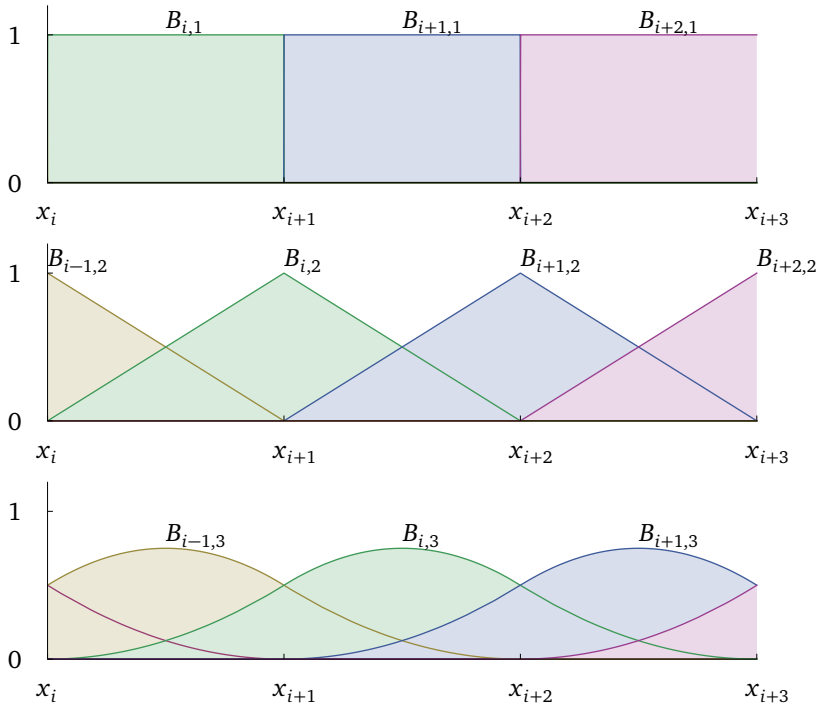

Figure 5.4: The diagram shows B-splines B_{ik} of orders one to three, according to the definition by de Boor, for the same n knots x_i. The upper part shows B-splines of order 1, which are piecewise constant. In the middle part, one sees B-splines of order 2, which are also known as hat functions or linear B-splines. The lower part shows B-Splines of order 2, or quadratic B-splines.

Some splines of different degree are shown in Fig. 5.4. If the sequence of knots is allowed to contain some knots multiple times, this special case has to be treated differently. However, we will require that the nodes are in strictly ascending order Multiple knots are equivalent with reduced continuity requirements at these knots, but for the numerical field simulations continuity of the material characteristics at least up to their first derivative is desired, even if the material possessed indeed some discontinuity. In this case, one obtains a spline curve $s(x)$ as weighted sum of the B-splines with weights a_i:

$$s(x) = \sum_i a_i B_{ik}(x). \tag{5.38}$$

This curve is piecewise-polynomial of degree $k-1$ between two neighboring knots. At the knots themselves, the curve is continuous up to its $(k-2)$-th derivative.

In our context, $s(x)$ corresponds to either $\tilde{\sigma}(|E|)$ or $\tilde{\varepsilon}_\mathrm{r}(|E|)$. For the purpose of estimating the material parameters, the set of knots spans the interval between 0 V/m and the maximum observed field strength $\hat{E}$. This interval is subdivided into n smaller intervals, which form a set of $(n+1)$ knots [33]:

$$\Delta = \{0 = x_0 < x_1 < \ldots < x_n = \hat{E}\}. \tag{5.39}$$

Not requiring a uniform distribution, the knots can be chosen freely as long as they are sorted in ascending order. By default the nodes are placed at equal distance between minimum and maximum value. During the calculation of the B-splines, some additional knots are adjoined temporarily, to remove the imposition of continuity at the upper and lower limits of the estimation interval, which unnecessarily restricts the shape of the material characteristics.

Using B-splines of order k as basis functions, some set of knots Δ and materials that depend on the present absolute value of field strength, the resistive and capacitive current densities become

$$\tilde{J}^\mathrm{r} = \sum_i \tilde{\sigma}_i B_{ik}^{\sigma}(|E|)\, E \tag{5.40}$$

and

$$\tilde{J}^\mathrm{c} = \sum_i \tilde{\varepsilon}_k \left(B_{ik}^{\varepsilon}(|E|) + \frac{\partial\, B_{ik}^{\varepsilon}(x)}{\partial\, x}\bigg|_{x=|E|} |E| \right) \frac{\partial\, E}{\partial\, t}\,. \tag{5.41}$$

The two equations are the equivalent of Equations 5.27 and 5.31 and the rest of the procedure is the same as described above.

The time-derivative of field strength $\frac{\partial E}{\partial t}$ is of critical importance. Calculation by means of finite differences from measured time and voltage leads to large oscillations. The application of moving averages and low-pass filters reduces the problem. However, the best results were obtained by calculating an approximating polynomial spline curve and evaluating its analytical derivative at the sampling points [42, 25]. The estimation of this spline curves is done in essentially the same way as the subsequent estimation of the material parameters.

5.4.3 Characterization of a Microvaristor-Filled Silicone-Rubber Material

This section presents some results for the characterization of a microvaristor-filled silicone rubber material. S. Blatt, who had realized the measurements and kindly

provided his data, observed that the characteristics, that he obtains with the method of Sec. 5.3, deliver an unsatisfactory explanation of the material behavior and questioned the linearity of permittivity. Others have suggested a nonlinear permittivity of varistor materials, too [20], but without providing strong enough arguments.

As mentioned above, the conventional method, according to Sec. 5.3 faces difficulties for materials with nonlinear conductivity and permittivity. These difficulties have been the motivation for the present approach. In the following, an OLS-based method will be applied to estimate conductivity and permittivity. The resulting material characteristics offer a much better agreement between observed and expected current. Furthermore, they confirm the argument for a nonlinear permittivity of varistor materials.

Fig. 5.5 illustrates the deficiency of the model with field-dependent conductivity and constant permittivity. Normally, the measured current should closely resemble

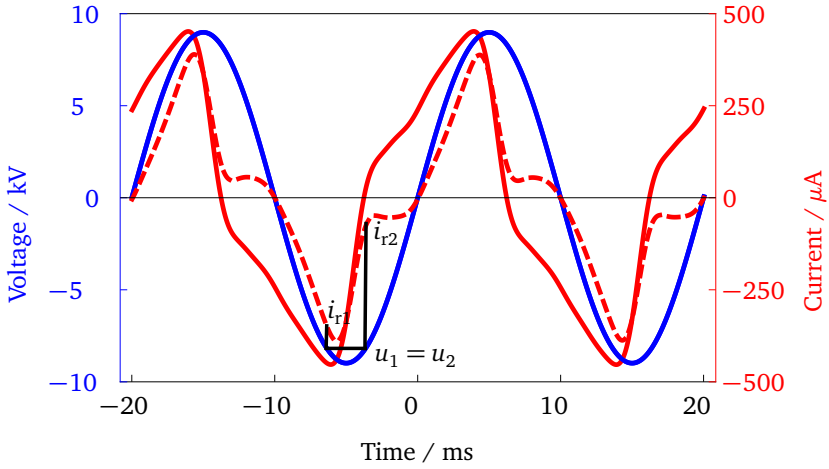

Figure 5.5: This figure shows that the assumption of a constant permittivity and a field-dependent conductivity can not be upheld for the microvaristor-filled specimen. The currents and the slope of the voltage signal at the voltage zero crossings in Figure 5.3 lead to a relative permittivity of about $\varepsilon_r = 18.35$. The corresponding capacitive current is subtracted from the observed current to obtain the resistive current (dashed line). If the model was valid, the same currents should be observed for identical voltages. Notwithstanding $u_1 = u_2$, the current i_{r1} is much larger than i_{r2}.

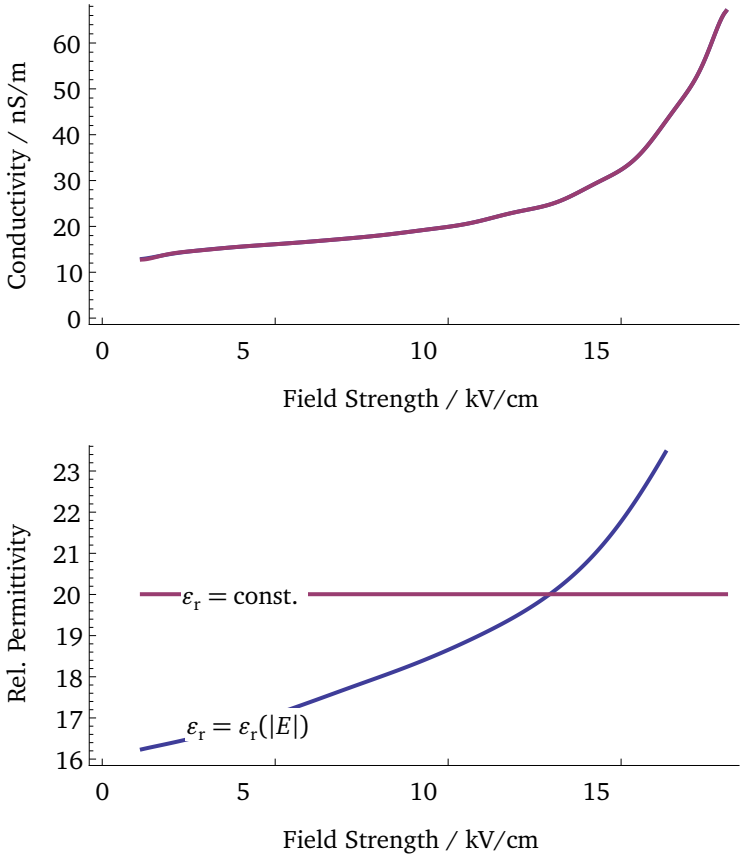

Figure 5.6: Estimated electrical conductivity σ and relative permittivity ε_r of a microvaristor sample. The characteristics have been obtained using the OLS approach for two different cases: a constant relative permittivity (violet), and a field-dependent relative permittivity (blue). The estimated conductivity seems to be independent from the assumption on permittivity, so that the violet and blue characteristics are almost identical. Conductivity increases sixfold. By contrast, permittivity is shown to grow by almost 50 % as field strength increases and differs clearly from the curve for a relative permittivity.

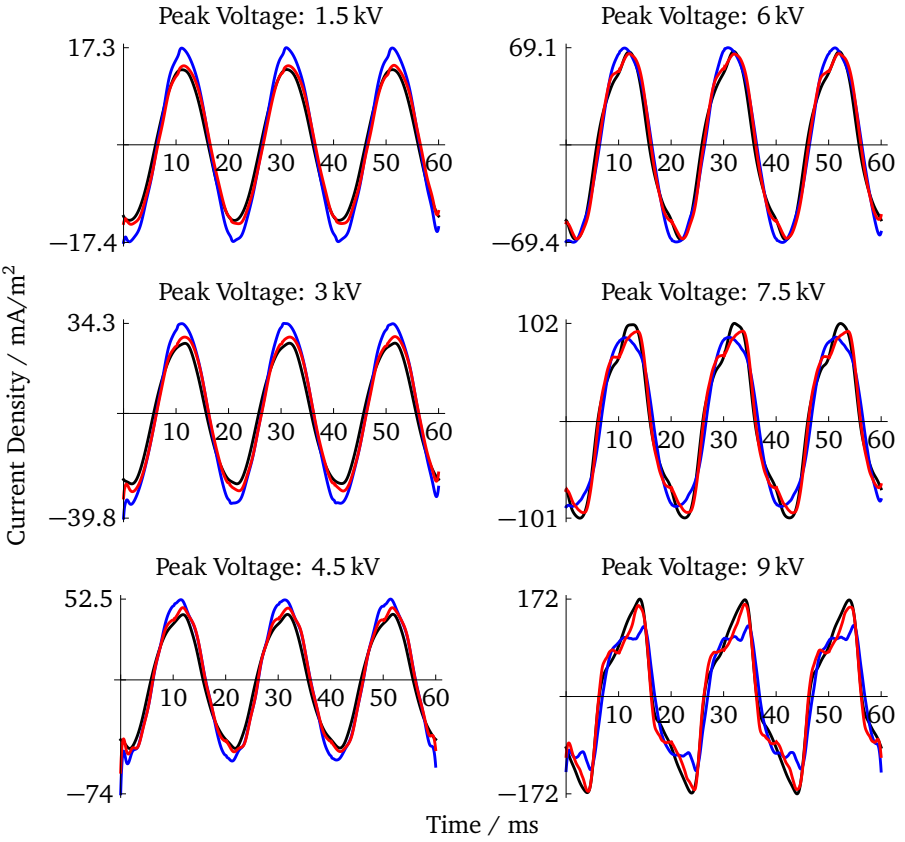

Figure 5.7: The diagrams show measured (black) and predicted current densities according to the characteristics of Fig. 5.6. The blue curves represent the predicted current densities for a constant relative permittivity ε_r, whereas the predicted current densities for a nonlinear relative permittivity are drawn in red. The assumption of a nonlinear permittivity leads to a much better agreement between observed and predicted behavior.

the sum of resistive and capacitive currents. After subtraction of the estimated capacitive current, the residual current has completely different values for the same voltage. This is contradictory to an interpretation of the remaining part as resistive current. Therefore, the model with constant permittivity and field-strength dependent conductivity poorly explains the observations.

The measured data, for which results are presented, comprise time, voltage and current for a series of thirty-five measurements with different peak voltage. The setup corresponds to that described in Sec. 5.2. The peak a.c. voltage of the individual measurements varies in steps of 250 V between 500 V and 9000 V . Since the examined specimen has a thickness of about 5 mm, the maximum field strength is 18 kV/cm. For every voltage level, the data consist of 2000 sampling points that span over two periods.[1]

The upper part of Figure 5.6 shows the characteristic curves for electrical conductivity, while the lower part of the figure depicts the corresponding curves for relative permittivity. The two parts of the figure plot the characteristics under the alternative assumptions of a constant relative permittivity (in violet) and of a field-strength dependent permittivity (in blue). The blue and violet curve are almost identical in the upper part of the figure. Apparently the estimated conductivity is independent from the assumptions made about relative permittivity. In both cases, conductivity increases approximately sixfold with rising field strength.

The lower part of the figure shows relative permittivity. Requiring a constant relative permittivity, its value is estimated to be close to 20. If permittivity is allowed to vary with field strength, the blue curve is obtained. It shows that relative permittivity increases by almost 50 %.

In Fig. 5.7 it is shown how good the different models fare in explaining the observed data. Given the evolution of field strength, derived from the measured voltage difference between the two electrodes, and the estimated characteristics for conductivity and relative permittivity, one can calculate the respective predicted current densities. Both models reproduce up to a certain point the observed current or current density. However, the difference between measured and predicted behavior is much larger for the model with constant relative permittivity. The assumption of a nonlinear permittivity allows a significantly better prediction of the observed currents. This is noticeable in the reduced overestimation of peak current density for the measurements with low peak voltage and the better approximation of the signal shape at very high field strengths.

[1] Actually, the input data are already post-processed data from measurement data over a larger time span.

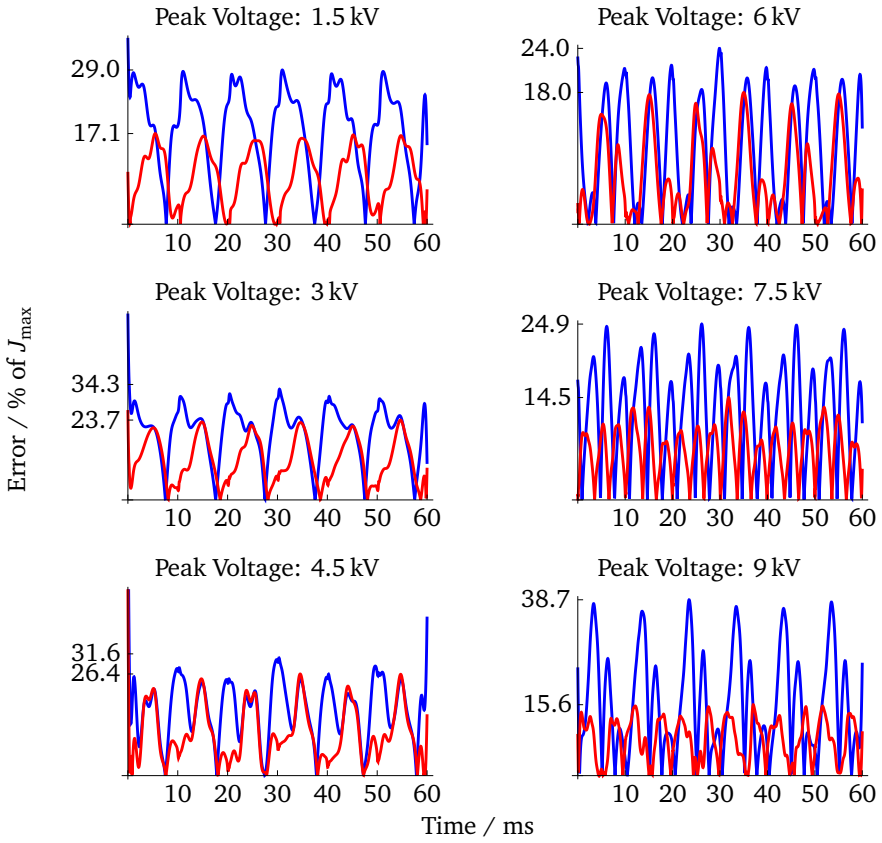

Figure 5.8: Difference between calculated and measured current density (see Fig. 5.7) with respect to maximum measured current density, i.e., $\left|\tilde{J}_i(t) - \tilde{J}_i(t)\right| / \max_t \left(\left|J_i^{\text{obs}}(t)\right|\right)$. The error of the model with constant permittivity is drawn in blue, while the significantly lower error of the model with nonlinear permittivity is shown in red.

In Fig. 5.8, the difference between predicted and actually observed current density is presented as a percentage value with respect to the respective maximum observed current density, which has been chosen as a reference to avoid spikes close to the

zero crossings. This difference or error is calculated according to the following equation from the data already shown in the last figure:

$$\text{error}_i(t) = \frac{\left|\tilde{J}_i(t) - J_i^{\text{obs}}(t)\right|}{\max_t\left(\left|J_i^{\text{obs}}(t)\right|\right)}. \tag{5.42}$$

The plots show that the prediction error for the current density has been reduced significantly for the measurements with low and high peak voltages. For the measurement with 1.5 kV peak voltage, the predicted current density differs by up to 29 % of its maximum observed value. This value decreases to about 17.1 %, which constitutes an improvement of more than 40 %. The prediction quality increases by an even larger value, almost 60 %, for the measurement with the highest peak voltage. This is particularly important, as understanding the behavior at high field strengths is critical to manage electrical losses and the dissipation of heat. In the middle range of peak voltages the improvement of the prediction quality is smaller, but still substantial.

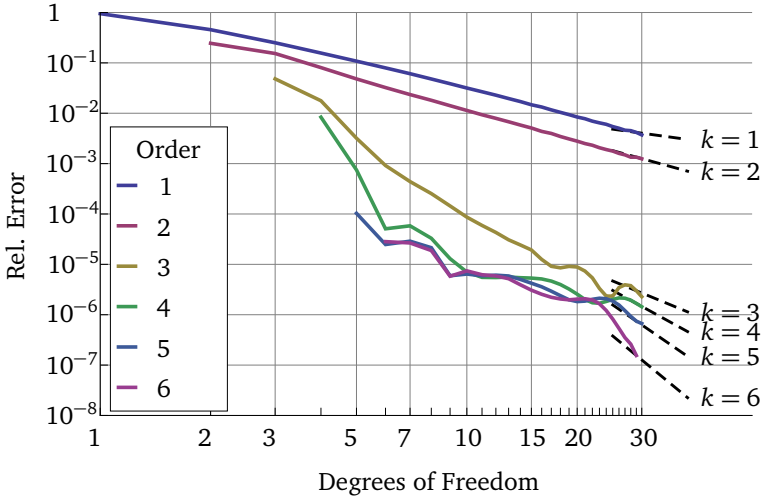

Figure 5.9: Convergence of the material characteristics obtained with B-splines of different order for increasing number of degrees of freedom. In all cases the material model converges to the same relative error of about 12.07 % according to Eq. 5.43. The value obtained for 30 B-splines of order six constitutes the reference solution.

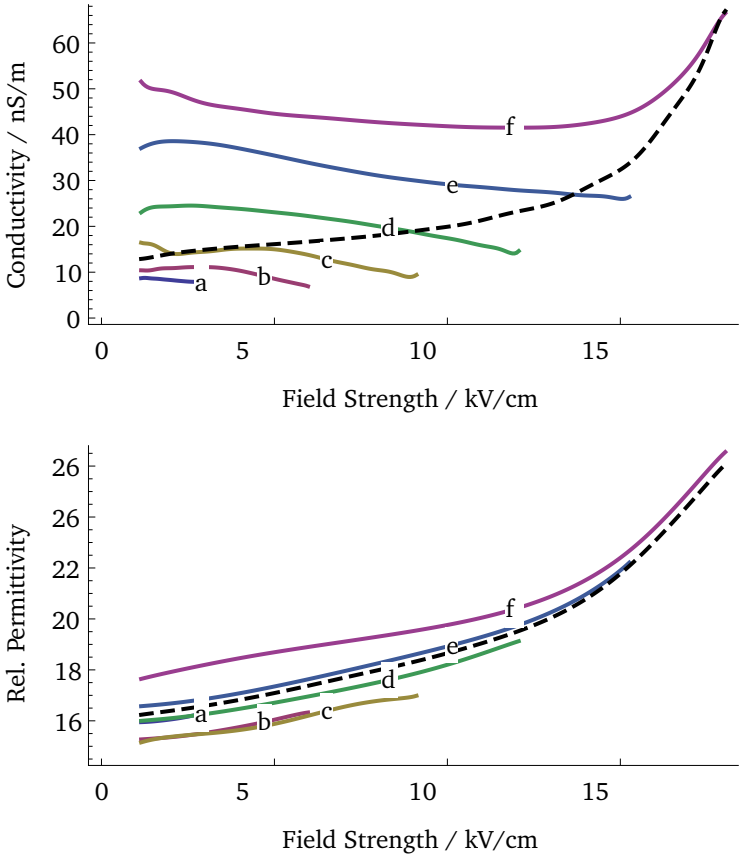

Figure 5.10: Characteristics for conductivity σ and relative permittivity ε_r of a microvaristor sample. The characteristics were obtained from measurements with different AC peak voltage (a: 1500 V, b: 3000 V, c: 4500 V, d: 6000 V, e: 7500 V, f: 9000 V). For comparison, the nonlinear characteristics of Fig. 5.6 have been added as dashed line. Except at very high field strength, the conductivity seems to depend more on peak voltage than on the present field value, which suggests the presence of a relaxation process.

Finally, Fig. 5.9 shows the convergence of the estimates with increasing number of degrees of freedom for different B-spline orders. While Fig. 5.8 has already given us some means to judge the error of the individual measurements, one can define another global measure of the total error. For a constant permittivity the relative error η over all observations, given by

$$\eta = \frac{\left\|\mathbf{J}_{\text{obs}} - \tilde{\mathbf{J}}\right\|}{\|\mathbf{J}_{\text{obs}}\|}, \tag{5.43}$$

converges towards 23.53 % with increasing number of degrees of freedom and spline order. Accepting a nonlinear permittivity the relative error decreases quickly towards a final value $\eta_0 \approx 12.07\%$. The convergence diagram displays the convergence to this value:

$$\frac{|\eta(d,k) - \eta_0|}{\eta_0}, \tag{5.44}$$

with chosen number of degrees of freedom d and splines of order k. As d is the number of degrees of freedom for both conductivity and permittivity, the total number of estimated parameters is twice that value. Not knowing the precise value of η_0, the supposedly most accurate estimate $\eta(30,6)$ is used as reference value. This leads to the convergence behavior shown in the figure and is in good agreement with the expected behavior, which is indicated by the dashed lines.

The results prove that the least-squares based method is applicable to estimate the electrical properties of nonlinear materials and provides good results. The obtained characteristics indicate strongly that relative permittivity is indeed nonlinear and that this effect plays an important role in explaining the observable behavior during measurements.

These significant results have been the point of departure for further studies after realizing that the material is not only nonlinear, but that there is also some kind of memory effect involved. One should expect that the residual difference between predicted and observed values is random and that the exclusion of individual measurements does not affect the estimated characteristics in the covered field-strength range. However, this is not the case. It is shown in Fig. 5.10 that the obtained characteristics differ significantly with respect to the retained measurement data. For example, if one uses the data from the measurement with peak voltage 9000 V, one estimates characteristic curves for conductivity and relative permittivity that lie substantially higher than those obtained from the other measurements.

If only the measurement data for the corresponding signal are used to estimate the material characteristics, the resulting characteristic curves for conductivity and permittivity explain the observed behavior consistently better than the previously

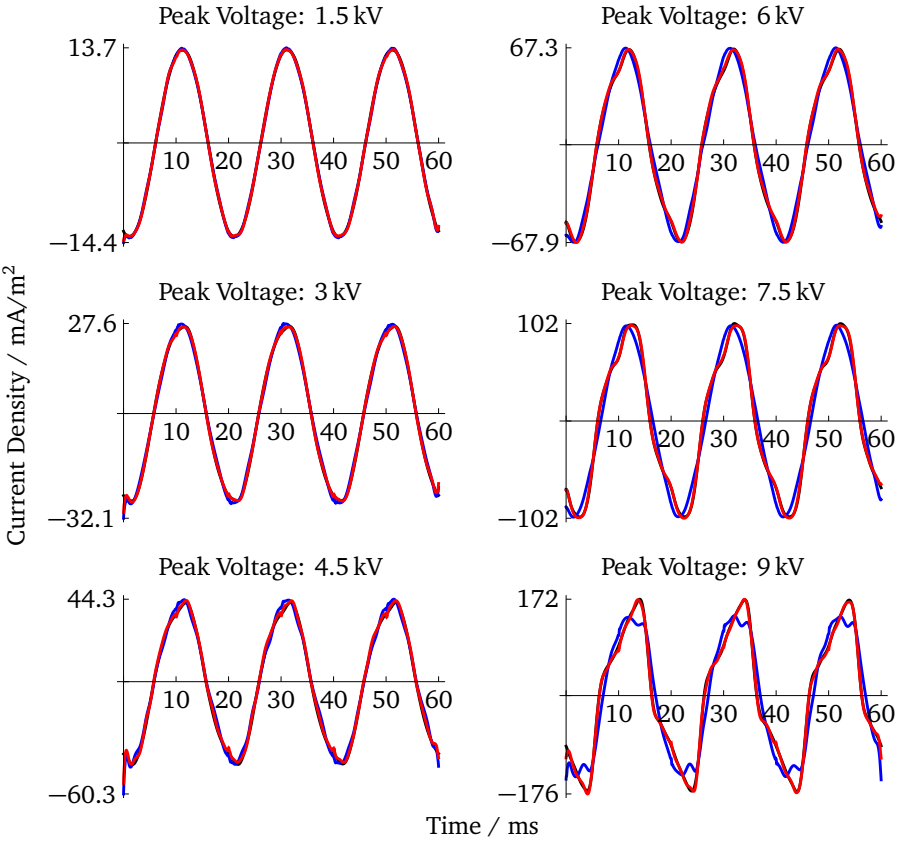

Figure 5.11: Measured and predicted current density for the characteristics of Fig. 5.10. The application of different characteristics depending on the respective peak Voltage leads to an important improvement of the prediction quality. It has become difficult to spot the measured current density (black) behind the current density calculated for the model with peak-voltage dependent nonlinear permittivity and conductivity (red). The blue curves show the predicted current density under the assumption of a constant permittivity.

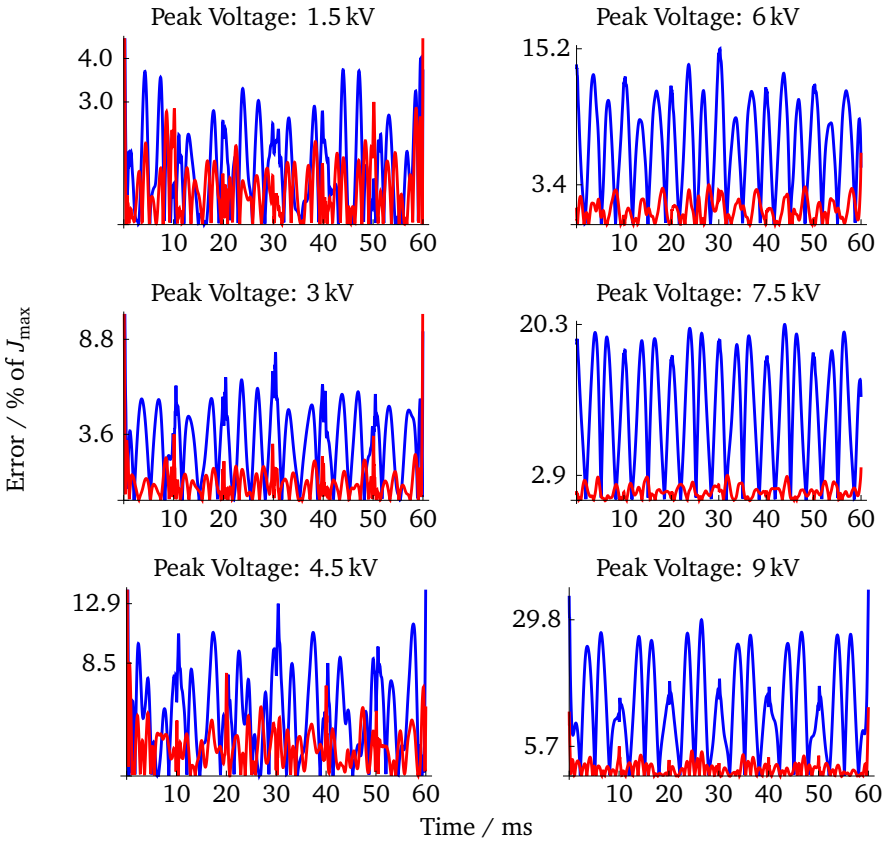

Figure 5.12: The individual figures provide an illustration of the error between observed and predicted currents in Fig. 5.11. The model with nonlinear conductivity and permittivity (red) proves to provide a much better prediction than the model with nonlinear conductivity and constant permittivity. The values should be compared with the previous Fig. 5.8, which gives the same representation, though for the case of a common characteristic irrespective of peak voltage.

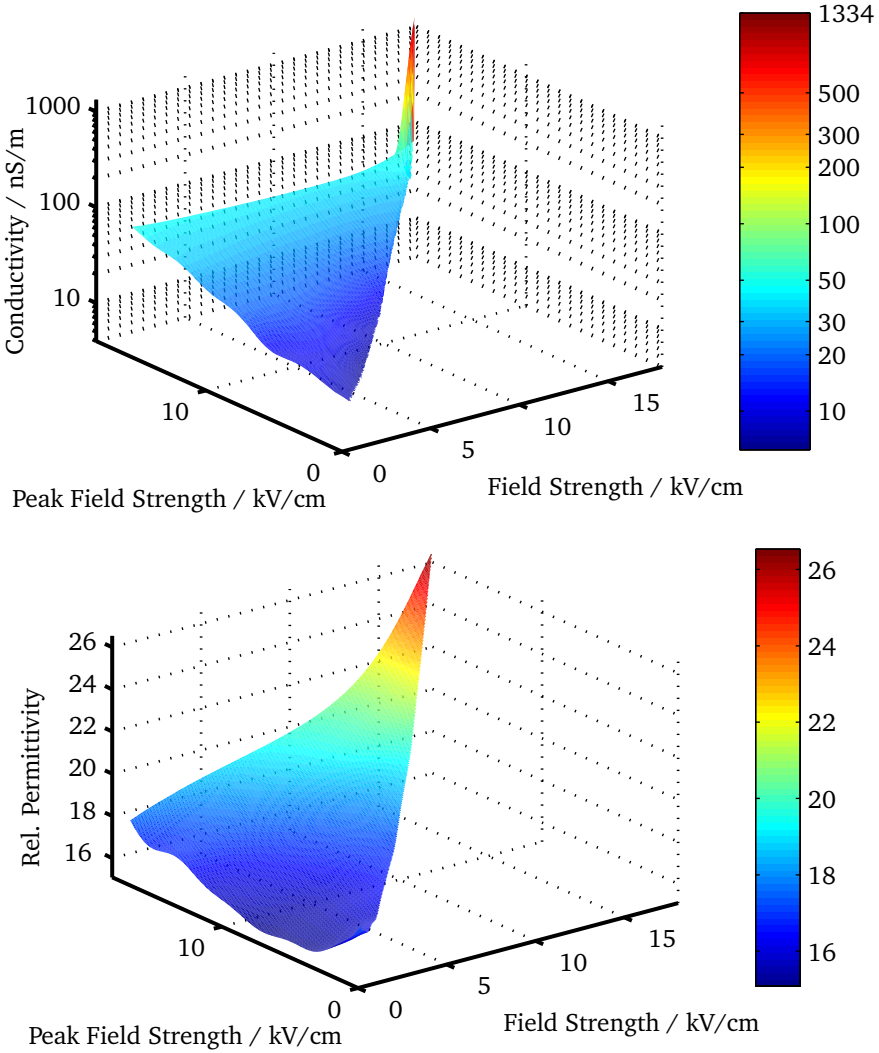

Figure 5.13: Electrical conductivity and relative permittivity of a microvaristor-filled silicone rubber as function of present and peak field strength, as derived from a series of 50 Hz measurements. The conductivity is shown to depend not only on present field strength, but also exponentially on the observed peak field strength of the respective measurement.

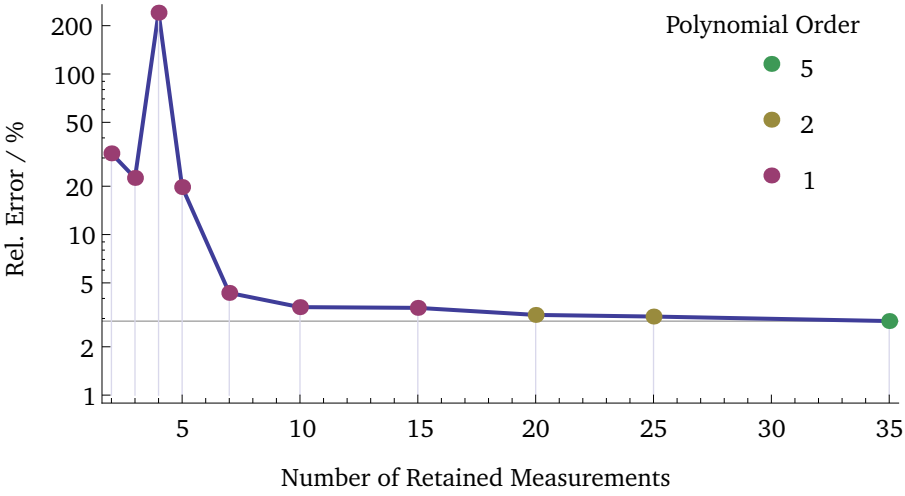

Figure 5.14: Visualization of results for the interpolation of material characteristics. The horizontal axis shows how many of the 35 measurements are used for the characterization of the material, while the vertical axis gives an error (see Eq. 5.43) for the whole group of measurements. The color of the points indicates the polynomial degree in peak voltage direction for the given data point.

presented characteristics. This is shown in Fig. 5.11. While the difference between red and black curves has already been small in Fig. 5.7, the two curves are now almost indiscernible. It has become difficult to spot the black curve behind the red one.

As before, the error is shown more explicitly in a second figure. Fig. 5.12 shows that the relative error with respect to the peak current density of the measurement is significantly reduced by taking into account present field strength and peak voltage. For example, one can observe that the error is reduced from up to 15.6 % to values below 5.7 %, if one looks at the critically important behavior at highest field strengths, i.e., the measurement data for 9000 V peak voltage.

It has already been observed that the adoption of a nonlinear relative permittivity leads to material characteristics which are in much better agreement with the experimental observations than those obtained under the assumption of constant permittivity. Nevertheless, the explanation of the material behavior is still incomplete, as the influence of peak voltage, respectively peak field strength, shows. The

observed material behavior can be explained even better, if peak voltage is taken into account, too.

The presented method can be extended to include a second dimension. This had been done to obtain field-strength and temperature dependent characteristics (see Sec. 6.1), but it is equally possible to use peak field strength $\hat{E}$ as second variable. This leads to:

$$\sigma = \sigma(|E|, \hat{E}) \approx \sum_i \sum_j \tilde{\sigma} w_i(|E|) \nu_j(\hat{E}) \tag{5.45}$$

$$\varepsilon_\mathrm{r} = \varepsilon_\mathrm{r}(|E|, \hat{E}) \approx \sum_i \sum_j \tilde{\varepsilon}_r w_i(|E|) \nu_j(\hat{E}), \tag{5.46}$$

with basis function w_i and ν_j which are not necessarily the same for conductivity σ and relative permittivity ε_r.

Some characteristics obtained in this way are shown as surface plots in Fig. 5.13 (for 15 × 12 intervals with polynomials of degree 5 × 5). This kind of characteristics are expected to provide accurate simulation results, when the electric in the examined microvaristor material oscillates indeed with a frequency of 50 Hz, the frequency for which the characterization data were obtained.

That it is possible to interpolate the obtained material characteristics to calculate currents and fields at further voltage or field strength levels is demonstrated by Fig. 5.14. It shows the minimum error according to Eq. 5.43 achieved for a specified maximum of 320 degrees of freedom, 16 in field strength direction times up to ten in peak field strength direction for conductivity and permittivity. Using every fifth measurement is sufficient to characterize the material with an error that is below 5 % according to the previously used measure of error. With increasing number of measurements taken into account to characterize the material the error converges to less than 2.9 %. Furthermore, the figure shows that the choice of splines of second or third order, equivalent to segment-wise linear or quadratic polynomials with respect to peak field strength, is preferable to higher-order basis functions for the same number of degrees of freedom.

In many cases, when the field is indeed oscillating with 50 Hz, this model may be useful. If one is interested in an analysis at another frequency, one needs another pair of characteristics, though. And for arbitrary signals, such a model is simply inadequate. Therefore, the next section discusses relaxation and the attempts to find a generally valid material model.

5.5 Relaxation

In the preceding sections the least-squares based approach had been successfully applied to characterize a microvaristor material. It had even been possible to

generate distinct characteristics for each of the 35 a.c. voltage measurements. Unexpectedly, the curves are not similar. Apart from differing with respect to the maximum covered field strength, they show a clear upward shift of conductivity and, to a lesser extent, of permittivity with respect to the peak voltage of the measurement (see again Fig. 5.11).

As an increase in temperature or any other measurement-related influence was excluded by colleague S. Blatt, one had to conclude that some kind of relaxation phenomenon is involved. The material properties depend not only on momentary field, but in some unknown way on the past evolution of the field.

The presentation of the constitutive relationships for Maxwell's equations in Sec. 3.1.2 includes an introduction into relaxation and its connection with dispersion. While relaxation can normally be deduced from an analysis in frequency domain, this is not possible in the present case. As the material is nonlinear with respect to field strength, the transformation between frequency and time domain is no longer allowed.

Nevertheless, one may assume that the microvaristor relaxation behavior is not completely different and try to use a similar model to analyze its behavior. The relaxation model of Eq. 3.16:

$$\mathbf{D}(t) = \varepsilon_0 \left(\varepsilon_\infty \mathbf{E}(t) + \int_0^\infty \dot{\Phi}(\tau) \mathbf{E}(t-\tau)\, \mathrm{d}\tau \right). \tag{5.47}$$

has to be extended to include a dependence on field strength. As it is unknown, if the observed relaxation is due to permittivity or conductivity, the same approach is used for permittivity and conductivity:

$$\mathbf{D}(t) = \varepsilon_0 \left(\varepsilon_\infty \left(|\mathbf{E}(t)|\right) \mathbf{E}(t) + \int_0^\infty \varepsilon_\mathrm{s} \left(|\mathbf{E}(t-\tau)|\right) e^{-\tau/\tau_\varepsilon} \mathbf{E}(t-\tau)\, \mathrm{d}\tau \right) \tag{5.48}$$

$$\mathbf{J}(t) = \sigma_\infty \left(|\mathbf{E}(t)|\right) \mathbf{E}(t) + \int_0^\infty \sigma_\mathrm{s} \left(|\mathbf{E}(t-\tau)|\right) e^{-\tau/\tau_\sigma} \mathbf{E}(t-\tau)\, \mathrm{d}\tau. \tag{5.49}$$

This approach corresponds to the Debye relaxation model, if the material properties are not affected by field strength. For this approach the estimated total current density becomes:

$$\begin{aligned} \tilde{J}(t) =& \sigma_\infty \left(|\mathbf{E}(t)|\right) \mathbf{E}(t) + \int_0^\infty \sigma_\mathrm{s} \left(|\mathbf{E}(t-\tau)|\right) e^{-\tau/\tau_\sigma} \mathbf{E}(t-\tau)\, \mathrm{d}\tau \\ &+ \varepsilon_0 \frac{\partial}{\partial t} \left(\varepsilon_\infty \left(|\mathbf{E}(t)|\right) \mathbf{E}(t) + \int_0^\infty \varepsilon_\mathrm{s} \left(|\mathbf{E}(t-\tau)|\right) e^{-\tau/\tau_\varepsilon} \mathbf{E}(t-\tau)\, \mathrm{d}\tau \right). \end{aligned} \tag{5.50}$$

Model	η
$\varepsilon_\mathrm{r} = \text{const.}$	23.53 %
$\sigma, \varepsilon_\mathrm{r} = f(\lvert E\rvert)$	12.07 %
$\sigma, \varepsilon_\mathrm{r} = f(\lvert E\rvert, \hat{E})$	2.89 %
relaxation	9.74 %

Table 5.1: Comparison of the attained error level with several material models. The error is significantly reduced by accepting a nonlinear permittivity and is further reduced, when peak field strength is taken into account as second parameter. For the described relaxation model, an error η of about 9.74 % has been achieved, which is better than the 12.07 % of the model relying only on present field strength, but still far from the 2.89 % of the model with peak field strength as parameter.

The parameters, on which the estimated current density $\tilde{J}$ relies, contained in the characteristics $\varepsilon_\infty(|\mathbf{E}(t)|)$, $\sigma_\infty(|\mathbf{E}(t)|)$, $\varepsilon_\mathrm{s}(|\mathbf{E}(t)|)$ and $\sigma_\mathrm{s}(|\mathbf{E}(t)|)$ as well as time constants τ_ε and τ_σ.

In principle, the material properties are estimated in the same way as in Sec. 5.4, i.e., by minimization of the difference between measured and estimated current densities:

$$\underset{\varepsilon_\infty,\sigma_\infty,\varepsilon_\mathrm{s},\sigma_\mathrm{s},\tau_\varepsilon,\tau_\sigma}{\text{minimize}} \left\| \mathbf{J}_\mathrm{obs} - \tilde{\mathbf{J}}(\varepsilon_\infty, \sigma_\infty, \varepsilon_\mathrm{s}, \varsigma_\mathrm{s}, \tau_\varepsilon, \tau_\sigma) \right\|_2 \tag{5.51}$$

Although the problem looks similar, apart from the larger number of parameters, it is much harder to solve. Because of the time constants which enter the model as a multiplicative factor, the problem is no longer linear.

Instead of solving some linear system of equations to find the optimum solution, an iterative method has to be used to solve the multidimensional nonlinear optimization problem. The Nelder-Mead simplex method, which was used, does not guarantee the discovery of a global minimum, but may converge to local minima [79].

In practice, the search for a optimum has been realized by gradually increasing the number of unknowns and manual intervention once the algorithm seemed to have reached a local minimum. This procedure does not guarantee finding the global minimum and there is no reason to assume that it has been found for the examined microvaristor material. For the calculation of the delayed material properties the periodicity of the signal had to taken into account to evaluate the integrals, as the expected relaxation times were not small with respect to the duration of the measurement data.

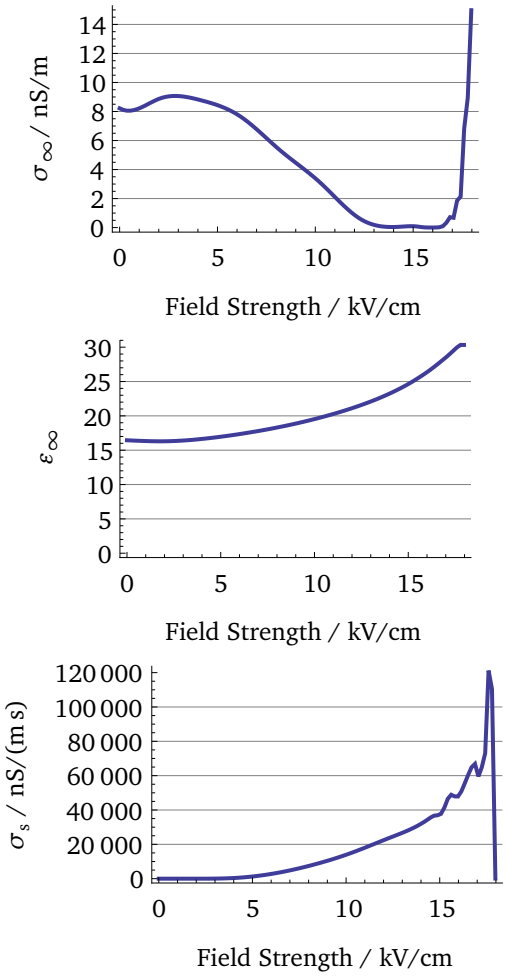

Figure 5.15: Estimated conductivity σ_∞, relative permittivity ε_∞ and the characteristic for σ_s, which describes the time-delayed resistive current. The characteristic for ε_s is not shown because of its minor contribution. The time constant associated with σ_s is $\tau_\sigma \approx 1.02\,\mathrm{ms}$.

The Table 5.1 shows that the best obtained relaxation model achieves a reduction of the error η (from Eq. 5.43) from 12.07 % to 9.74 %. This improvement is far from negligible. However, the relaxation model explains the observed material behavior much less than the model with peak field strength as variable. Unfortunately, the cost in computation time and the tendency of the solution process to end up in local minima do not let us firmly conclude, whether another model is needed or if the model is valid and only the numerical solution unsatisfactory. Much better material characteristics than those shown in Fig. 5.15 are likely to exist. For that purpose, a better search method would be of great usefulness. The relaxed permittivity is omitted in Fig. 5.15 because its contribution to the total current is negligible. With time constant $\tau_\sigma \approx 1.02\,\mathrm{ms}$, the current corresponding to σ_s is mostly of greater importance than the current related to σ_∞.

6 Surge Arrester Simulations

6.1 Computation of Stationary Operational Condition of Surge Arresters

This section is dedicated to the calculation of the thermally stationary state of a surge arrester under operating conditions, when the arrester is connected to an a.c. voltage source. The voltage may be either the normal operational voltage or an elevated voltage used for testing the thermal stability of a surge arrester. The

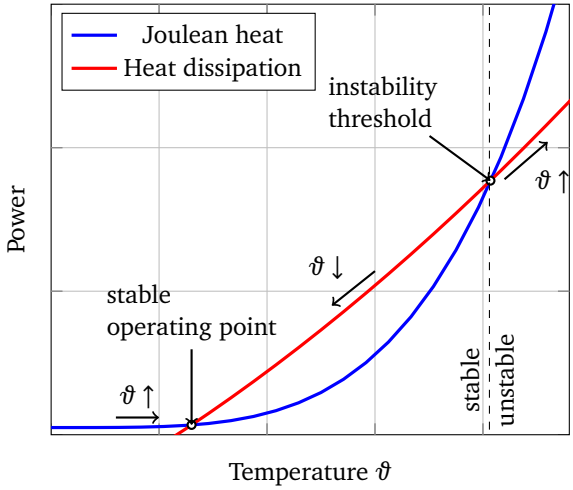

Figure 6.1: Illustration of thermal runaway. The diagram shows the Joulean heat generation and heat dissipation of a valve element. The first intersection point constitutes a thermally stable operating point. Up to the second intersection point the element is thermally stable as dissipation of heat to the environment exceeds heat input. Beyond the second intersection point between the two curves the element is thermally unstable as the injected heat is higher than the heat that is simultaneously dissipated to the environment. Adapted from Lat [64].

purpose of this simulation is to determine the stationary temperature distribution of the arrester and to verify that no thermal runaway takes place.

Varistors possess a so-called NTC behavior, which means that their electrical resistance decreases for rising temperature. Since the arrester voltage is given, the Joulean heat losses increase. Normally, this constitutes no problem. The arrester will return to its equilibrium temperature distribution, because heat dissipation increases faster than the Joulean losses. This holds true for some temperature range around the thermal equilibrium. At higher temperatures the Joulean heat losses begin to exceed heat dissipation, though, as illustrated in Fig. 6.1. If the feed-in voltage is not reduced in time, the arrester continues to heat up until it fails.

Guaranteeing thermal stability is a problem that has gained importance in the last few years along with the development of surge arresters for higher voltage levels. The greater height of ultra-high voltage (UHV) surge arresters, which reach voltage levels of 1100 kV to 1200 kV today, causes severe design problems because of the greater stray capacitances [47].

A thermal runaway does not occur spontaneously, but happens after the injection of a significant amount of thermal energy, e.g., by a series of lightning pulses. According to Cooray [54] a typical ground flash consists of four to five lightning strokes. First, a so-called stepped leader connects to the ground and initiates a return stroke that travels from ground to the cloud base. After the return stroke the current may continue to flow for some milliseconds. After the disappearance of the current, the discharge provoked by the return stroke can evolve into a dart leader traveling to ground through the previously established channel, resulting in a further return stroke. More dart leaders and return strokes may follow.

Thus, one is concerned about the likelihood of events, which lead to thermal runaway, and about the energy an arrester can absorb and still return to thermal equilibrium.

This problem is not satisfactorily solved, yet. Zheng et al. [105] claim to have succeeded in computing the thermal stability of a full-scale arrester, but rely on major model simplifications, e.g., reducing the electrical part of the problem to one dimension. The following section, Sec. 6.2, presents another approach with its own limitations. A further, more conventional method is currently examined by colleagues at TU Darmstadt.

If the problem of simulating the cooling behavior of a surge arrester over time spans of several hours continues to be a problem, the determination of the thermal equilibrium state seems to be more feasible. The idea is that of combining a transient simulation of the electric part of the problem with a static solution of the thermal problem:

$$-\operatorname{div}(\lambda \operatorname{grad} \vartheta) = \dot{w}_{\mathrm{gen}}. \tag{6.1}$$

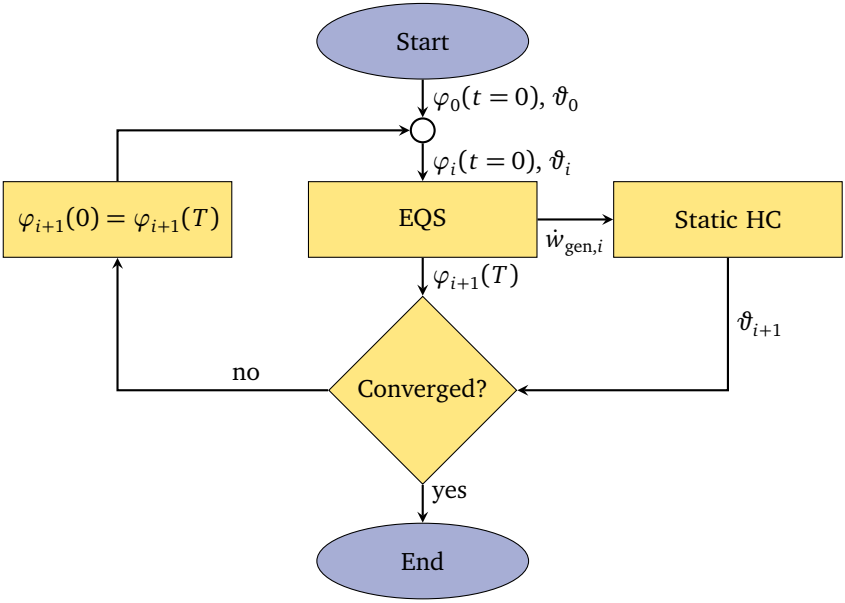

Figure 6.2: Flow chart illustrating the procedure to calculate a thermally stationary state for a nonlinear, time-periodic electric problem, for which temperature can be considered as constant. The time-averaged Joulean heat losses are calculated by means of a transient electro-quasistatic simulation. They are then used to get a temperature field by solving the static heat conduction equation. To obtain a thermal and electrical steady state after several iterations, the simulation is restarted with the thermal and last electric solution.

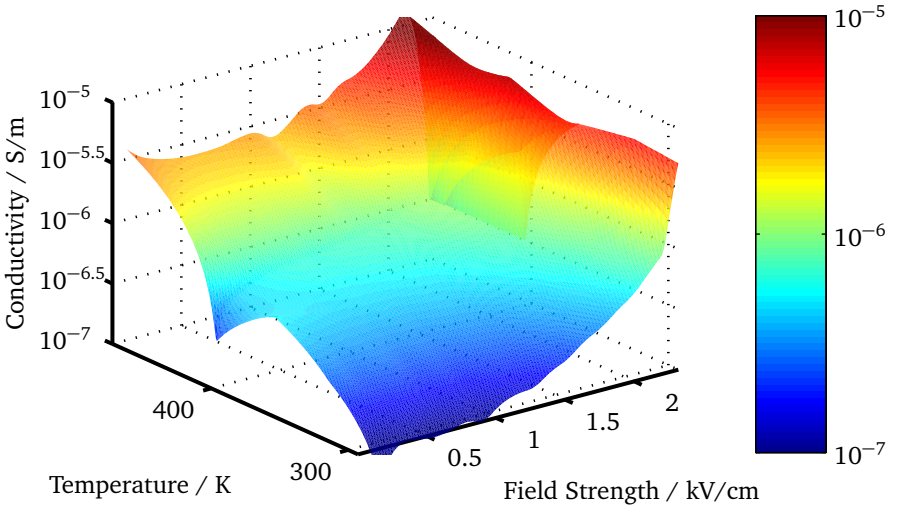

Figure 6.3: Estimated temperature and field-strength dependent electrical conductivity of a ZnO varistor.

The electric part is simulated for (at least) one period. During this simulation the Joulean heat losses per period are calculated. Using these heat losses, the static temperature distribution in the arrester can be determined. Since the losses in the arrester depend on temperature, the electric simulation is repeated for the new temperature. In parallel, the final distribution of the electric potential is used as initial solution for the next iteration. In the course of several cycles the thermal solution is expected to converge to its equilibrium distribution, while the electric initial solution converges to its steady state (see Fig. 6.2).

Using this procedure the equilibrium temperature of a four-unit surge arrester has been calculated, which is used regularly for experiments at the High-Voltage Lab of TU Darmstadt. The simulation reproduces an experiment, for which the arrester was placed without pedestal close to ground. This increases the nonhomogeneity of the voltage stress and heat losses for a given voltage level. While this is undesirable in practice, it can be useful for some experiments.

For conductivity and permittivity, field-strength and temperature dependent characteristics are used, which have been obtained in the same way as the peak field-strength dependent characteristics in Sec. 5.4.3. However, peak field strength is replaced by temperature as second parameter in Eqs. 5.45 and 5.46.

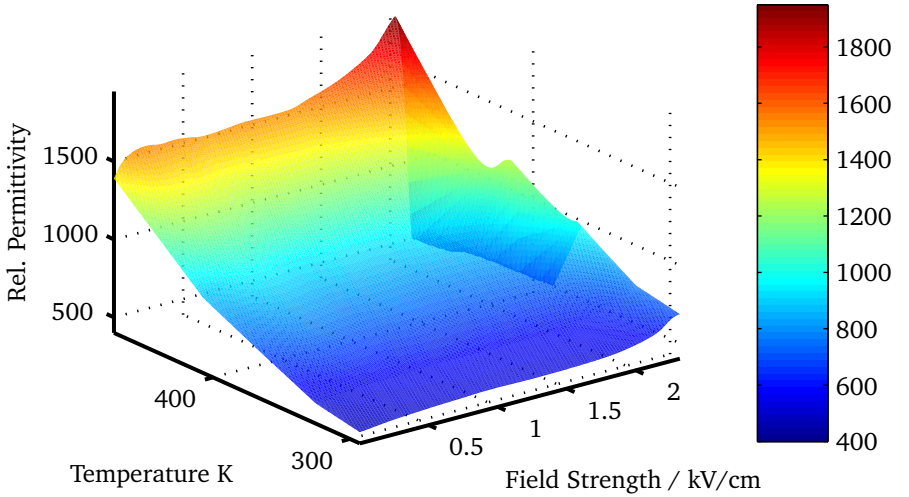

Figure 6.4: Estimated temperature and field-strength dependent relative permittivity of a ZnO varistor.

The data for the varistor characterization come from a large sequence of measurements. They were provided by the High-Voltage Lab of TU Darmstadt. The temperature spans over a range between about 20 and 200 °C. The characterization process leads to estimated conductivity values in the range between $1 \cdot 10^{-7}$ S/m and $1 \cdot 10^{-5}$ S/m, while the relative permittivity lies between 400 and close to 2000 (see Figs. 6.3 and 6.4).

To obtain better simulation results two boundary conditions are added. First, a combined convection/radiation boundary for the surface of the arrester (housing, flanges). The second boundary condition is of greater interest. It is a consequence of a suggestion by M. Tuczek that radiative heat exchange between the resistor column and the interior surface of the housing might be of importance. A complete description of the interaction between all the elements on the surface of resistor column and housing would lead to dense matrices, apart from posing questions about the respective line of sight. Therefore, a simplified boundary condition for the reciprocal heat exchange has been implemented to take into account the heat exchange in radial direction.

The resistor column is subdivided into numerous segments, essentially the surfaces of the individual varistors. Each of these segments is supposed to exchange

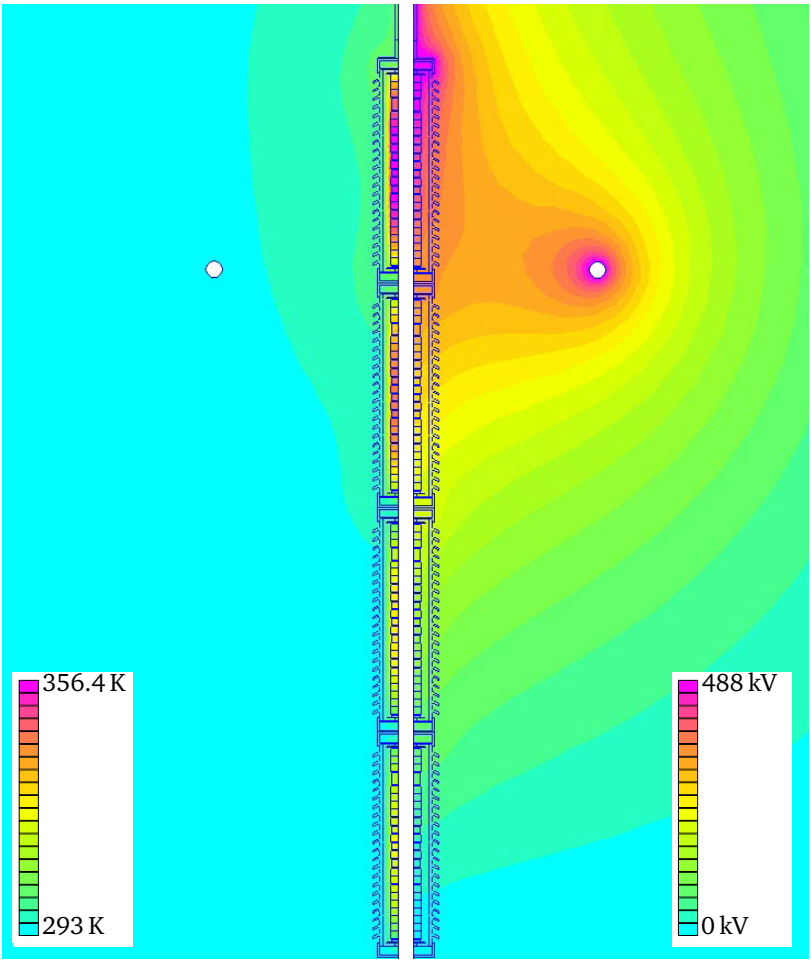

Figure 6.5: Stationary heat distribution and momentary electric potential of a surge arrester model. The model corresponds to a four-unit porcelain-housed surge arrester used for experiments at the High-Voltage Lab of TU Darmstadt. Voltage stress and heat generation are increased , because the arrester is not placed on a pedestal, as is normally the case. Boundary conditions have been chosen in accordance with the guidelines for the determination of the voltage distribution along metal-oxide surge arresters of standard IEC 60099-4 [51]. The computational domain extends in radial and upward direction beyond the shown area.

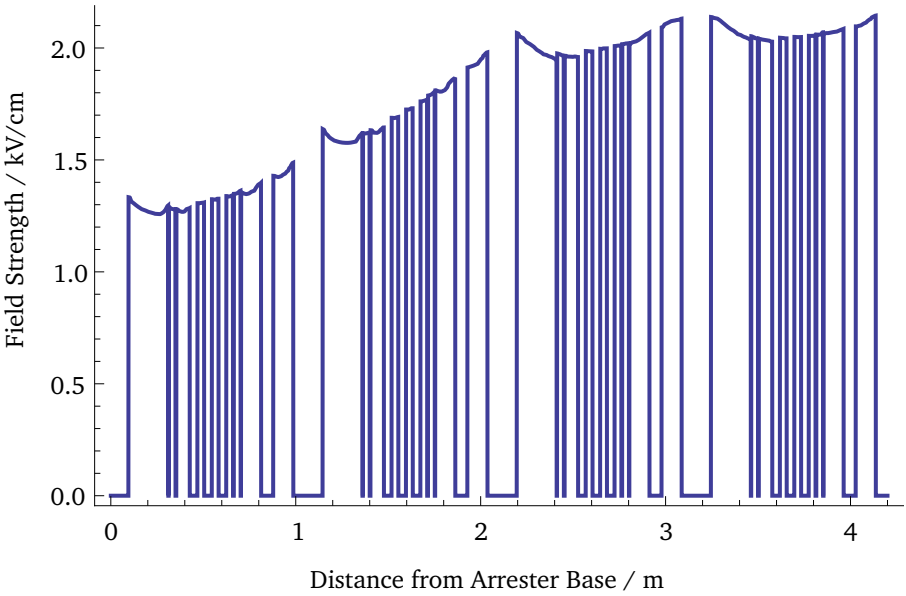

Figure 6.6: Electric field strength along the resistor column for the arrester model shown in Fig. 6.5. The voltage stress is greatest for the two topmost arrester units. The curve seems to indicate that field grading succeeds in homogenizing the voltage stress in the upper part of the arrester.

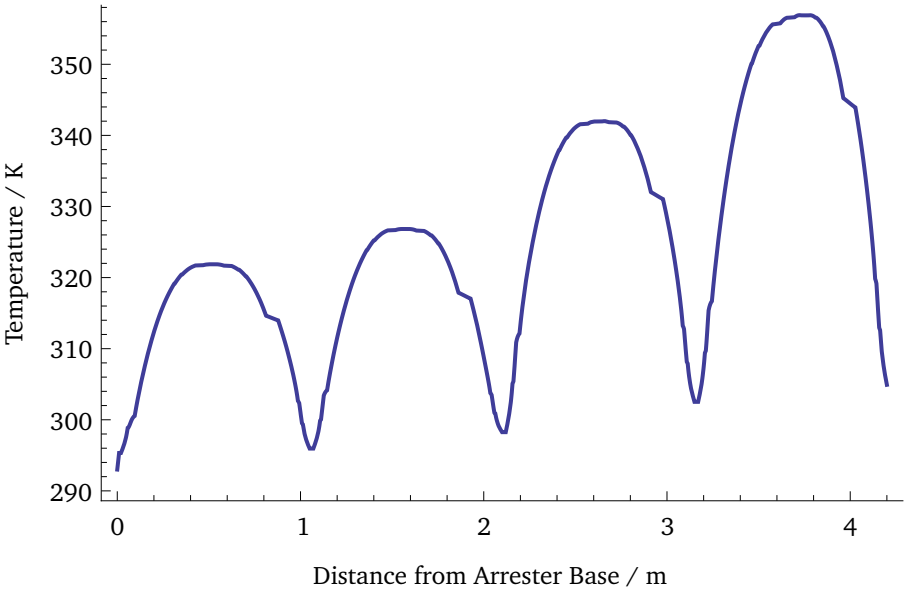

Figure 6.7: Temperature along the resistor column. At the bottom, the temperature remains close to the assumed ambient temperature of 293 K, whereas the equilibrium temperature exceeds 350 K in the upper arrester unit.

heat with a corresponding segment of the interior of the housing. Normally, radiative heat exchange is modeled by:

$$\dot{q} = \epsilon \sigma_{\mathrm{SB}} \left(\vartheta_1^4 - \vartheta_2^4 \right), \tag{6.2}$$

with a surface at unknown temperature T_1 which receives irradiated heat from another surface at temperature T_2. The second temperature is generally given and often corresponds to ambient temperature. In the present case, both temperatures are unknown. The emission of heat can be calculated normally for the surface of each finite element, whereas the irradiated heat is approximated from most recent temperature solution of the surface with the corresponding boundary condition.

For each of the reciprocal heat surface segments, the total emitted heat power is calculated by summing up the emitted heat power of the finite element surfaces which belong to this segment. An average irradiation power density is calculated by dividing this heat power through the surface area of the corresponding segment. This is done before the loop through all elements to build the local system matrices.

During the loop the emission of heat is calculated element-wise as usual, while the irradiation is imposed as additional Neumann boundary condition term. The greatest deficiency of this model is that it ignores the impact of reflections and assumes that the emitted heat from one surface is absorbed by the other one.

The simulations indicate that it is indeed possible to calculate the equilibrium temperature in the presented way. Notwithstanding the nonlinear nature of the problem, the same solution is obtained for largely varying initial conditions. If the initial temperature is not chosen too high, so that the solution process converges towards a thermal runaway solution, the same thermal equilibrium is attained. In Fig. 6.5 the equilibrium temperature distribution is shown along with the electric potential for the moment of peak excitation voltage. The temperature outside of the arrester is meaningless, though, as convective heat is not passed from the arrester to the air, but leaves the system at the housing and flange surface. The electric field strength along the resistor column can be seen in Fig. 6.6 and the temperature along the same line is shown in Fig. 6.7.

Regrettably, the results may not be compared directly with measurements. The boundary condition, a Dirichlet boundary on the circumferential surface of the simulation area, results in quite different results from those, which are obtained in the real, three-dimensional environment. Furthermore, the results may vary to a large extent with respect to variations of the thermal parameters, for which uncertainty is great. Nevertheless, the values seem to be reasonable. They are also in agreement with recent transient long-term stability simulations.

6.2 Envelope Model for Transitory Processes in Surge Arresters

After the injection of thermal energy into a surge arrester by a lightning stroke or a sequence of closely followed strokes, the arrester does not always return to its previous stationary state. Sometimes a thermal runaway takes place. Unfortunately, it is not immediately after the injection of thermal energy clear, whether the system is still inside the limits of thermal stability. Even after waiting a long time, during which the temperature seems to normalize, a thermal runaway may still materialize.

If one attempts to simulate this process, one faces the problem that one has to follow the evolution of the arrester temperature over a long time span, possibly many hours to safely exclude a thermal runaway. By contrast, the length of the time steps, at least for the electrical solution, has to be about a millisecond to resolve the exciting a.c. voltage signal and even less for the nonlinear currents. Such a simulation is currently not feasible.

A possible escape from this difficulty is the application of an envelope equation model. Such models are frequently used in optics and beam dynamics, e.g., [75, 35].

If one assumes that the electric potential inside the arrester is harmonic and sine shaped, the potential can be substituted by a complex phasor $\underline{\Phi}$. Notwithstanding that restriction, the amplitude and phase of the sine signal are allowed to vary slowly in time and differ locally.

At every moment the momentary potential is given by

$$\Phi(\mathbf{r}, t) = \mathrm{Re}\left\{\underline{\Phi}(\mathbf{r}, t) e^{j\omega t}\right\}. \tag{6.3}$$

The phasor $\underline{\Phi}$ is defined in terms of an amplitude $\hat{\Phi}$ and phase angle α, which depend on location $\mathbf{r}$ and time t:

$$\underline{\Phi}(\mathbf{r}, t) = \hat{\Phi}(\mathbf{r}, t) e^{j\alpha(\mathbf{r},t)}. \tag{6.4}$$

If this equation is inserted into the electro-quasistatics equation, one obtains:

$$\mathrm{div}\left(\frac{\partial}{\partial t}\left(\varepsilon_\mathrm{r}\varepsilon_0 \,\mathrm{grad}\,\underline{\Phi}\right)\right) + \mathrm{div}\left((\sigma + j\omega\varepsilon_\mathrm{r}\varepsilon_0)\,\mathrm{grad}\,\underline{\Phi}\right) = 0. \tag{6.5}$$

As long as $\underline{\Phi}$ varies slowly, time steps many times as large as the period of the harmonic signal are possible.

In the case of an arrester, one faces two questions with respect to this approach. The first question refers to the assumption of an essentially harmonic potential. Due to the nonlinearity of the varistors, it is not ensured that the real potential does not deviate significantly from a sine shape. Even when such a signal is imposed at its terminals, the potential is expected to deviate to some extent inside the resistor column, because of stray capacitances and nonlinear varistor behavior.

Fortunately, a uniform distribution of the electric field along the resistor is a major design goal for surge arresters. Therefore, one can hope that the deviation is sufficiently small to justify the application of the envelope equation model.

The second question is related to the material parameters that one has to insert into the equation. Every time step spans over many periods and during each of them conductivity varies significantly along with field strength. The question is, which value of conductivity has to be used to get a field solution that is close to the true one. Certainly, the conductivity has to be in some way an average value of the real conductivity in that time span.

Two different conductivities have been examined. The first conductivity relies on a power equivalence: The Joulean losses per period with equivalent conductivity $\overline{\sigma}_\mathrm{p}$ are supposed to be equal to the losses with nonlinear conductivity $\sigma(E)$:

$$\int_0^T \overline{\sigma}_\mathrm{p} E^2(t)\,\mathrm{d}t = \int_0^T \sigma(E(t)) E^2(t)\,\mathrm{d}t, \tag{6.6}$$

with period length T and sinusoidal field strength $E(t) = \hat{E}\sin(\omega t)$.

This leads to:

$$\overline{\sigma}_{\mathrm{P}} = \frac{\int_0^T \sigma(E(t))E^2(t)\,\mathrm{d}t}{\int_0^T E^2(t)\,\mathrm{d}t}. \tag{6.7}$$

The second conductivity is based on an equivalence in current terms. The time-averaged current with a conductivity σ_{I} is required to be equal to the current with real conductivity $\sigma(E)$:

$$\int_0^{T/4} \overline{\sigma}_{\mathrm{I}} E(t)\,\mathrm{d}t = \int_0^{T/4} \sigma(E(t))E(t)\,\mathrm{d}t, \tag{6.8}$$

where an interval between 0 and $T/4$ has been chosen instead of 0 to T because the integration over a whole period leads to a value of zero.

Hence, the equivalent conductivity $\overline{\sigma}_{\mathrm{I}}$ becomes:

$$\overline{\sigma}_{\mathrm{I}} = \frac{\int_0^{T/4} \sigma(E(t))E(t)\,\mathrm{d}t}{\int_0^{T/4} E(t)\,\mathrm{d}t}. \tag{6.9}$$

Numerical Experiments with the Envelope Equation

The potential of the envelope equation model is examined in two ways. For both, the simplified model of multi-unit surge arrester from IEC standard 60099-4 is used. The first test consists of a parameter study, where the local and total heat generation of the envelope equation model is compared to the results of a normal time-domain simulation. This comparison is realized for various material characteristics with different degree of nonlinearity and voltage levels. The second study compares the voltage stress along the resistor column with reference values cited in the mentioned standard.

For the parameter study a varistor conductivity, which follows the power law kE^{α} plus an additional term σ_0 for conductivity at low field strength is assumed:[1]

$$\sigma(E) = \sigma_0 + kE^{\alpha}. \tag{6.10}$$

[1] Note that $\sigma \propto E^{\alpha}$ implies $I \propto U^{(\alpha+1)}$, and not $I \propto U^{\alpha}$.

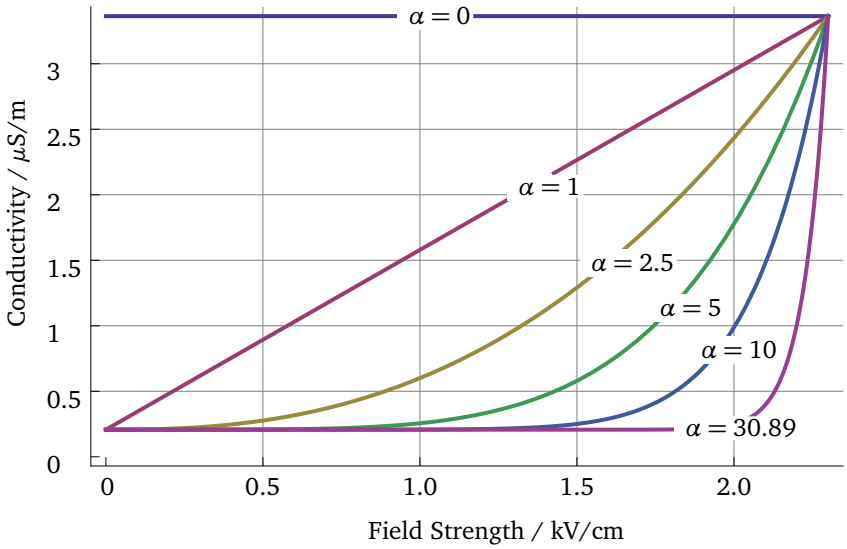

Figure 6.8: Extracted conductivity characteristic of a ZnO varistor fitted to a model of the type $\sigma(E) = \sigma_0 + kE^{\alpha}$. with a nonlinearity coefficient of $\alpha = 30.89$ as well as several fictitious characteristics with lower degree of nonlinearity, but spanning the same range of conductivity values. These characteristics were among those used to test the envelope equation model.

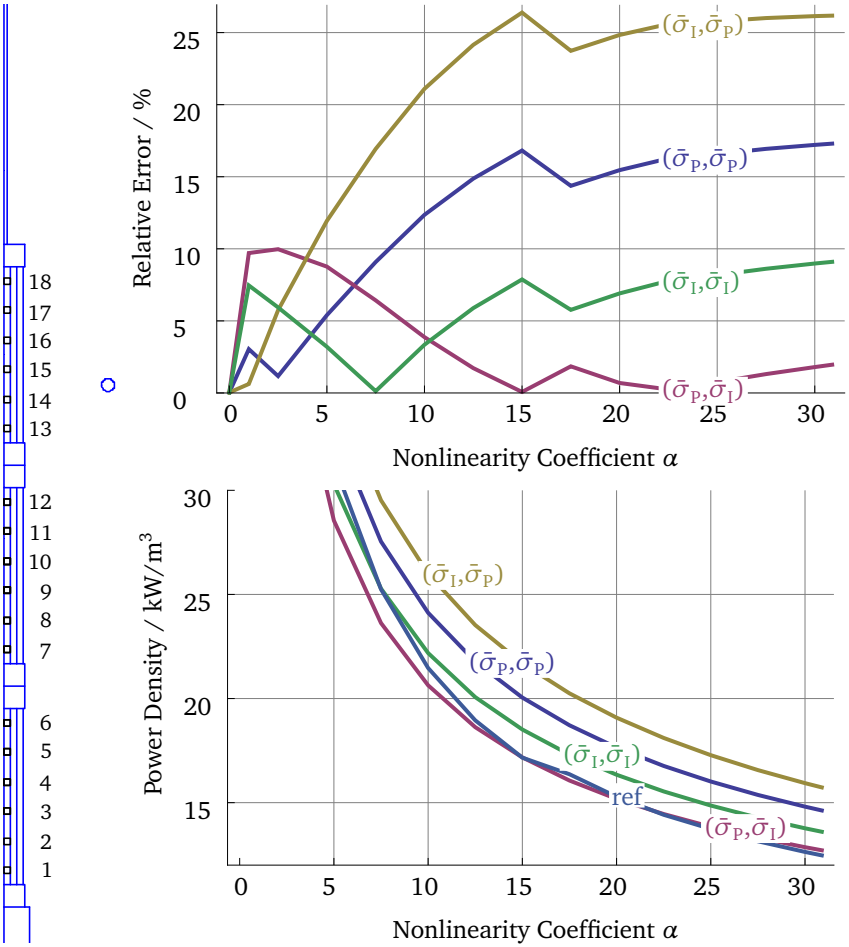

Figure 6.9: The upper diagram shows the relative error of the envelope equation model for nonlinearity coefficients α between 0 and 30.89 for the simplified multi-unit surge arrester at measurement point 18 (left). The surge arrester is excited with peak voltage $\hat{U} = 570\,\mathrm{kV}$, about 332 kV rms. The names of the curves indicate, whether Eq. 6.11 or 6.12 has been used to calculate the electric potential or Joulean heat generation. For example, the solution obtained from using $\overline{\sigma}_\mathrm{I}$ for electric potential and $\overline{\sigma}_\mathrm{P}$ for heat generation is named $(\bar{\sigma}_\mathrm{I},\bar{\sigma}_\mathrm{P})$. The lower diagram shows the calculated time-averaged heat losses for the different $\overline{\sigma}_\mathrm{I}/\overline{\sigma}_\mathrm{P}$-combinations as well as the reference solution (ref).

This leads to equivalent conductivities $\overline{\sigma}_\mathrm{P}$ and $\overline{\sigma}_\mathrm{I}$:

$$\overline{\sigma}_\mathrm{P} = \sigma_0 + \frac{2k\Gamma\left(\frac{3+\alpha}{2}\right)}{\sqrt{\pi}\Gamma\left(2+\frac{\alpha}{2}\right)}\hat{E}^\alpha, \tag{6.11}$$

$$\overline{\sigma}_\mathrm{I} = \sigma_0 + \frac{\sqrt{\pi}k\Gamma\left(1+\frac{\alpha}{2}\right)}{2\Gamma\left(\frac{3+\alpha}{2}\right)}\hat{E}^\alpha, \tag{6.12}$$

with gamma function Γ, an extension of the factorial to non-integer values, and peak field strength $\hat{E}$.

The fitting of the material characteristic of a real varistor, which had been realized in a similar way to that described in Sec. 5.4, has led to the model:

$$\sigma(E) \approx 2.07 \cdot 10^{-7} + \left(\frac{E}{3.47 \cdot 10^5\,\mathrm{V/m}}\right)^{30.89}\ \mathrm{S/m}. \tag{6.13}$$

Therefore, an envelope equation model for the simulation of varistor-related problems should manage to provide satisfactory results for nonlinearity coefficients of $\alpha = 30$ and beyond.

To examine the limits of the model, fictitious material characteristics were generated, which cover the same range of conductivity values, but exhibit a lower degree of nonlinearity α (see Fig. 6.8). The multi-unit arrester was studied for various peak voltages $\hat{U}$ and conductivity characteristics. The time-averaged heat generation $\bar{w}$ was calculated for a number of specified points in the resistor column, which are shown on the left-hand side of Fig. 6.9. Normal electro-quasistatic simulations over several periods to obtain a solution close to steady state provided reference values for comparison with results for the envelope equation model.

In the simulations the peak voltage $\hat{U}$ ranges from 235 kV to 564 kV and the nonlinearity coefficient α from 0 to 30.89. For the highest simulated voltage levels at 517 and 564 kV convergence and stability problems were observed for high values of α leading to incomplete results. Therefore, the discussion will have to concentrate on the results for a peak voltage of 470 kV, at which the problem is already markedly nonlinear

Fig. 6.9 shows some of the simulation results for a peak voltage of 470 kV, which corresponds to a rms voltage of about 332 kV. In the upper part of the figure the relative difference of the calculated Joulean heat losses between the simulations with the envelope equation model and the transient electro-quasistatic reference solution can be seen. As expected, the results are practically identical for a nonlinearity coefficient of $\alpha = 0$. In that case the problem is completely linear and the envelope equation model is exact, irrespective of the choice of equivalent conductivity.

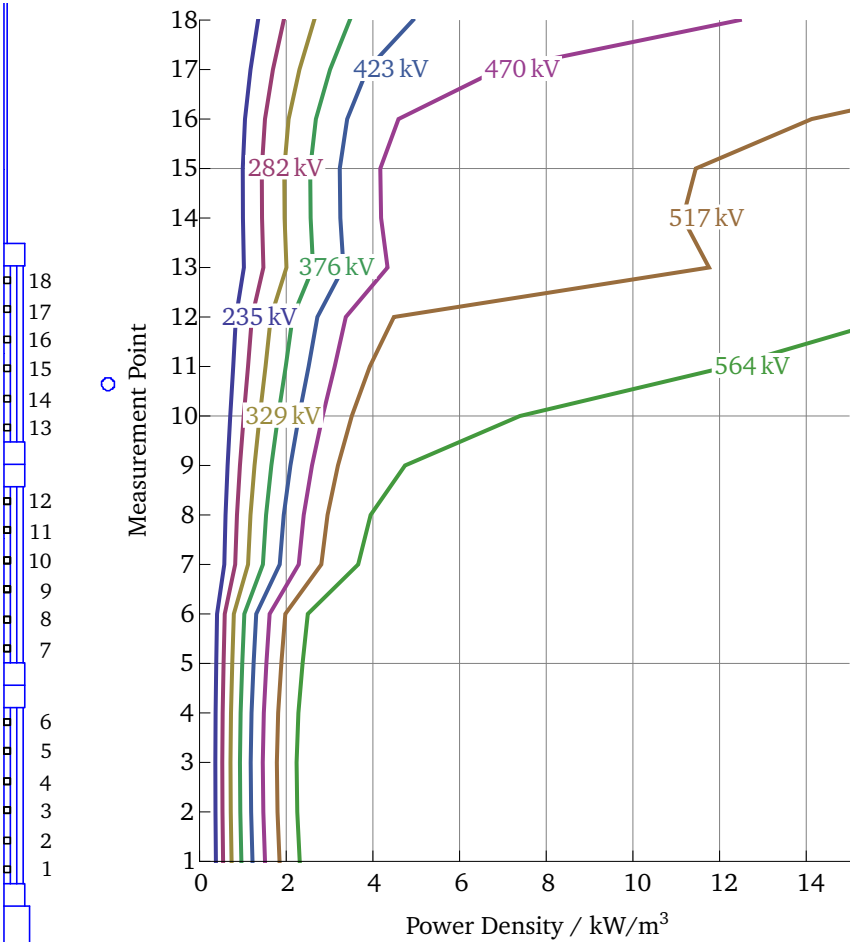

Figure 6.10: Volumetric heat generation due to Joulean losses at the 18 observation points along the resistor column of the surge arrester shown on the left. In an ideal arrester without the presence of stray capacitances the electric field and heat losses are uniform. In practice, locally enhanced fields are observed in the upper part of the arrester. The enhanced electric fields, especially when they start exceeding the switching field strength, lead to significantly higher losses, as can be observed for the curves corresponding to peak voltages above 423 kV.

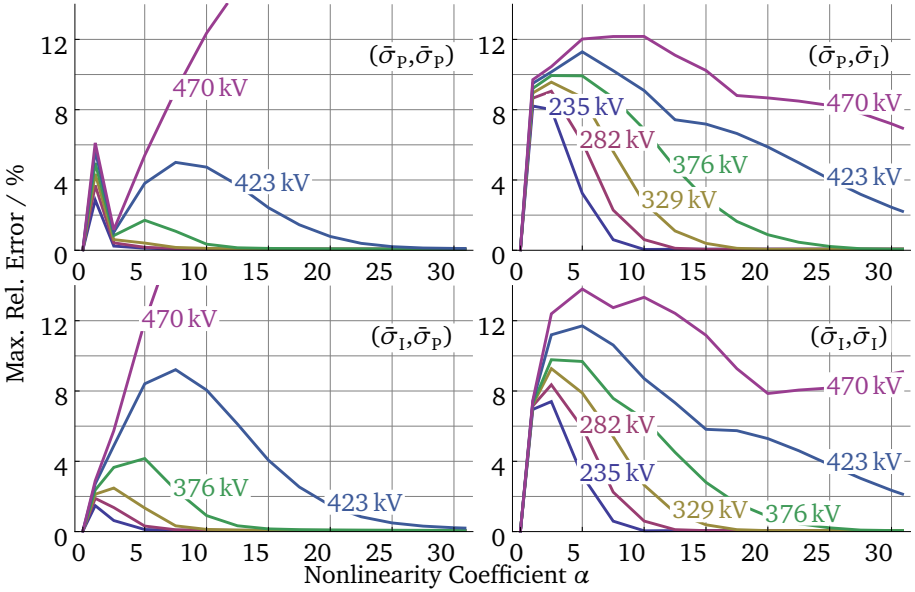

Figure 6.11: Maximum relative error for each of the four equivalent conductivity combinations as function of the nonlinearity coefficient α depending on the labeled peak voltage. The maximum relative error is the highest value among the 18 simultaneously observed relative errors. Generally the maximum error is observed at a point in the upper arrester unit, but not necessarily at the very top.

For $\alpha > 0$ the error of the envelope equation model depends on the chosen combination for the equivalent conductivity. The equivalent conductivity is used in two contexts. First, it is used in the electro-quasistatic envelope equation model of Eq. 6.5. Second, the conductivity is used to calculate the time-averaged Joulean losses according to:

$$\bar{w} = \frac{1}{2}\bar{\sigma}_i \hat{E}^2, \tag{6.14}$$

where $\bar{\sigma}_i$ stands for either $\bar{\sigma}_\mathrm{I}$ or $\bar{\sigma}_\mathrm{P}$. In Fig. 6.9 the curves for relative error and heat losses are designated according to the possible combinations. The first symbol stands for the equivalent conductivity used for the field simulation and the second one for the Joulean heat losses. For example, ($\bar{\sigma}_\mathrm{I}$,$\bar{\sigma}_\mathrm{P}$) stands for the result with equivalent conductivity $\bar{\sigma}_\mathrm{I}$ used for the field simulation and $\bar{\sigma}_\mathrm{P}$ for heat generation.

According to the figure, the combination of using the power-equivalent conductivity for the field simulation and the current-equivalent conductivity for the Joulean heat generation delivers the best results. The relative error is consistently below 10 % and is even lower than 3 % for high degrees of nonlinearity, The error of the other approaches tends to rise with increasing degree of nonlinearity, although it is still less than 10 % over the entire range of α-values for the combination ($\bar{\sigma}_\mathrm{I}$,$\bar{\sigma}_\mathrm{I}$).

It might have have been a reasonable guess to assume that the power-equivalent conductivity is the preferable choice for the calculation of the power losses and that current equivalence gives eventually a better field solution, but this is apparently not the case.

Given that the field at the chosen observation point 18 close to the top of the arrester is larger and more nonlinear than elsewhere, such relatively small errors seem to indicate that the envelope equation model works reasonably well.

Below, the absolute value of volumetric Joulean heat generation is plotted for the different equivalent conductivity combinations as well as the reference solution. Unsurprisingly, the losses decrease with increasing degree of varistor nonlinearity.

Fig. 6.10 plots the volumetric Joulean heat generation of the reference solutions at the 18 observation points, as shown on the left-hand side, for different peak voltages between 235 and 564 kV. The previously discussed results correspond to the topmost point of the 470 kV curve with losses exceeding 12 kW/m^3. Evidently, this voltage is close to the protective level of the arrester. The resistance of the resistor column decreases and current rises sharply.

The Fig. 6.11 offers a more complete visual representation of the errors of the envelope equation model. It shows the maximum value of the relative error observed along the resistor column for the four equivalent conductivity combinations as function of nonlinearity coefficient α for peak voltages up to 470 kV. While the maximum error is generally observed somewhere in the upper arrester unit,

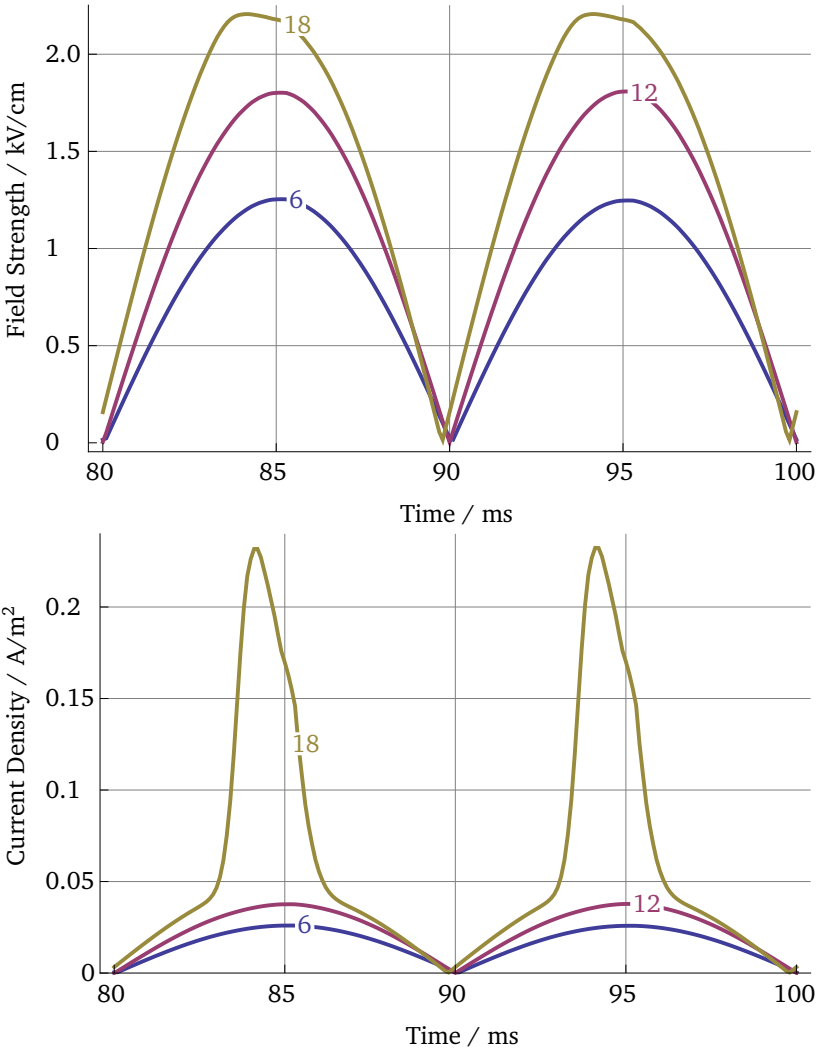

Figure 6.12: Absolute value of field strength and resistive current density at various points of the simulated arrester as function of time. The field-strength data were obtained from the simulation for the reference solution at $\hat{U} = 470\,\mathrm{kV}$ with $\alpha = 30.89$, while the current density values were generated with Eq. 6.13. The curves correspond to measurement points (6, 12 and 18) close to the top of the three arrester units, as shown in Fig. 6.10 (left).

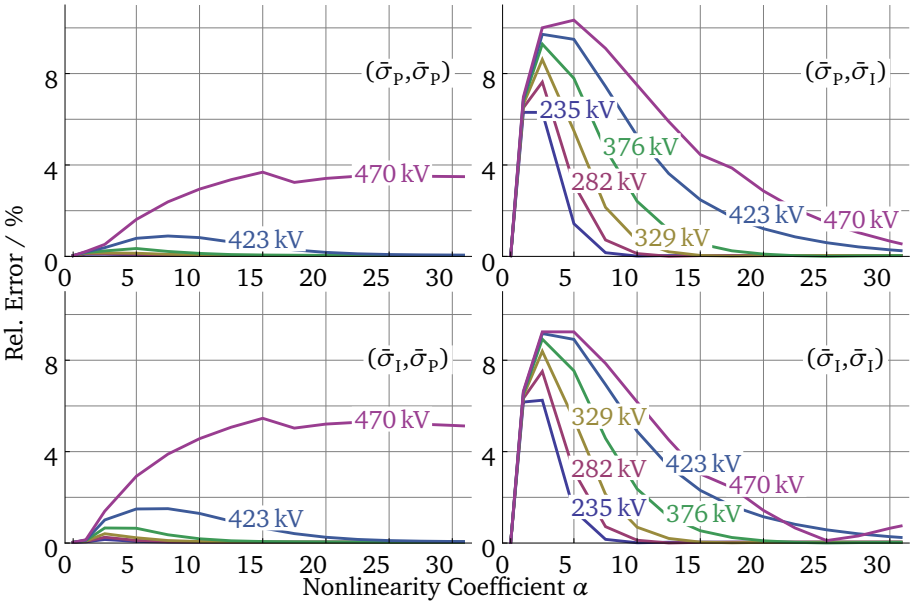

Figure 6.13: Relative error of the total heat dissipation in the resistor column of the surge arrester, approximated by the sum of the Joulean losses at the observation points, as function of nonlinearity coefficient α for the four equivalent conductivity combinations. The different curves correspond to the peak voltage of the respective simulations. Especially the two equivalent conductivity combinations on the right-hand side provide good estimates of total Joulean heat losses for high degrees of material nonlinearity.

its maximum value is not necessarily reached at the topmost observation point. Therefore, the error of the 470 kV curve for $\alpha = 30.89$ is about 7 % instead of the previously cited 3 %

The subsequent Fig. 6.12 shows the absolute value of electric field strength recorded during a normal, i.e., without envelope equation, electro-quasistatic simulation of the simplified model of a multi-unit surge arrester for peak voltage $\hat{U} = 470\,\mathrm{kV}$ and nonlinearity coefficient $\alpha = 30.89$. Below, the resistive current density that is calculated from these field strengths is plotted.

The shape of the field strength, and in consequence of the potential, deviates visibly from a sine shape for the curve obtained at the uppermost observation point 18. There, the peak field strength is reduced due to the varistor material entering the nonlinear regime. Still, the corresponding points of the lower arrester units show no significant distortion. For much of the arrester, the assumption of the envelope equation model, which posits that the potential is essentially harmonic, is valid, even when the arrester operates close to its threshold voltage. The figure also shows that there is a minor phase shift between the different observation points.

The reduction of peak field strength for the uppermost observation point is accompanied by a significant increase of conductivity and resistive current, as shown for the corresponding curve in the lower part of the figure. The high nonlinearity of the varistors leads to a sharp rise of the resistive current during a sub-interval of the voltage period. To put this increase into context, it has to be noted that the peak capacitive current is still twice as large as the peak resistive current.

Finally, Fig. 6.13 shows the relative error for the sum of the extracted Joulean heat losses in the resistor column. The curves prove that the injection of electric energy into the surge arrester is calculated quite accurately for each of the equivalent conductivity combinations. However, for high degrees of nonlinearity, the two combinations on the right-hand side are clearly preferable with relative errors falling below 1 %.

The second test of the envelope equation model consists of a voltage stress comparison. Apart from including a second guard ring, the geometry is the same as before, but the previously used power-law characteristic is replaced by a characteristic derived from Fig. L.4 of standard IEC 60099-4. The characteristics for $\bar{\sigma}_\mathrm{P}$ and $\bar{\sigma}_\mathrm{I}$ are obtained by numerical integration of equations 6.7 and 6.9. The model corresponds to case C of the standard, a 2D computation with two grading rings and consideration of resistive effects. The expected maximum voltage of the three units is given as 41 %/m (top), 39 %/m (middle) and 29 %/m (bottom). With respect to accuracy, it is stated that *[d]eviations of* 1 %/m *to* 2 %/m *may typically be expected.*

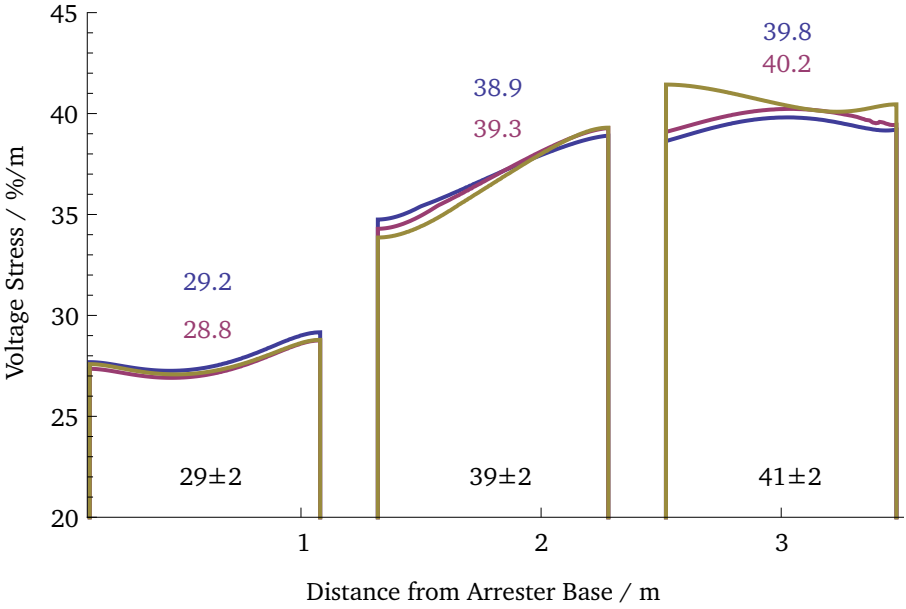

Figure 6.14: Voltage stress along the resistor column between bottom and top of the surge arrester. The blue curve is obtained, when a power-equivalent conductivity is assumed, whereas the violet curve is based on the current-equivalent conductivity. The numbers in the plot indicate that all results lie within the range considered as acceptable according to standard IEC 60099-4 Annex L. However, the brown curve, which represents the solution of a normal time-domain solution, shows that there is a notable difference.

In Fig. 6.14 the results of the finite element simulations are shown. As heat generation is of no importance, the figure presents only two solutions for the envelope-equation model and the solution of a normal transient simulation. The deviation of envelope-equation model solutions lies well within the the expected range. It reaches at most 0.8 %/m for the current-equivalent and 1.2 %/m for the power-equivalent conductivity. Thus, the results of the envelope equation model satisfy the requirements of standard IEC 60099-4. However, that does not mean that the envelope equation model provides indeed entirely satisfactory results. The figure shows that the obtained voltage stress curves differ nonetheless substantially from the curve obtained by means of a normal transient simulation.

Concluding Remarks on the Envelope Equation Model

The approach described as envelope equation model represents a major simplification of the real problem. This leads inevitably to a loss of accuracy. Given the difficulty of solving the problem without simplifications, this sacrifice of accuracy may be tolerated, if it is not too large. To determine the extent of this sacrifice, many simulations of a surge arrester model have been realized.

While the results of the presented studies confirm the limitations of the model, the error is not unacceptably high, if the right equivalent material characteristics are used. Even if the nonlinearity of the material properties and stray capacitances lead to potentials, which are not perfectly harmonic, the validity of the envelope equation model for surge arrester simulations is strongly supported by the effects of field grading and high varistor permittivity, which was set to $\varepsilon_r = 800$ in accordance with IEC 60099-4.

The error with respect to heat generation depends strongly on the degree of nonlinearity α of electrical conductivity. While the results are exact for linear materials, the error generally reaches its maximum for low values of α and decreases as the nonlinearity increases further. A possible explanation is that the model leads to relatively good results, if either the resistive or capacitive currents dominate, whereas the error is greatest during the transition between these two states.

The total heat generation by Joulean losses in the surge arrester is quite accurately estimated, if the appropriate equivalent conductivity is chosen. For high values of α the observed error lies in the range of no more than 1 %. This low level of error can be seen as a confirmation of the envelope equation model.

The distribution of the heat losses is subject to greater error. Nevertheless, the maximum observed error of local heat generation does not exceed 10 %. This is astonishing, given the sensibility of this value with respect to field strength, as heat generation increases proportionally to $\hat{E}^{\alpha+2}$.

A second test has been the comparison of the voltage stress along the resistor column for the envelope equation model with reference values given in a standard and results of a normal transient field simulation. Given that the degree of nonlinearity is relatively low, below six, one may expect a larger error following the preceding observations. Nevertheless, the deviation of the calculated voltage stress from its reference values lies comfortably inside the range of tolerance. The comparison with the results of the normal transient simulation shows that the stress curves of the envelope equation model differ significantly from their expected shape.

Even if the envelope equation model has been applied only to purely electric problems until now, there are no relevant obstacles to its application for the examination of the thermal stability of surge arresters. The displayed results are promising, although it has to be seen to which extent an envelope equation model can be used for the simulation of surge arresters or other nonlinear problems.

7 Nonlinear Circuit Model for Varistor-Based Stress Control

7.1 Capacitance and Conductance Matrices

The relationship between electric potentials and charges in linear media is described by a matrix $\mathbf{C}_{\text{inf}}$:

$$\mathbf{Q} = \mathbf{C}_{\text{inf}}\,\varphi. \tag{7.1}$$

Consequently, the vector of currents $\mathbf{I}$ is related to the time derivative of the potentials by:

$$\mathbf{I} = \mathbf{C}_{\text{inf}}\,\dot{\varphi}, \tag{7.2}$$

and the energy W stored in the electric field is:

$$W = \varphi^T \mathbf{C}_{\text{inf}} \varphi. \tag{7.3}$$

The matrix $\mathbf{C}_{\text{inf}}$ that unites these three properties is commonly called capacitance matrix.

However, the name is ambiguous. In accordance with Lehner [65] and Kupfmüller [62] the name capacitance matrix will be given to another matrix, which will be introduced soon. Instead, the name matrix of influence coefficients is used as name for matrix $\mathbf{C}_{\text{inf}}$.

Under the assumption $\varphi(\mathbf{r}) = \sum_l \varphi_l w_l(\mathbf{r})$, the matrix of influence coefficients can be derived from GAUSS's law. The charge Q_k of conductor k depends on the potential φ_l of every conductor l (including $l = k$) [7]:

$$Q_k = \int_{\partial\Omega} \mathbf{D} \cdot \mathrm{d}\mathbf{A} \tag{7.4}$$

$$= -\int_{\partial\Omega} \varepsilon \operatorname{grad}\varphi \cdot \mathrm{d}\mathbf{A} \tag{7.5}$$

$$= \sum_l \varphi_l \left(-\int_{\partial\Omega} \varepsilon \operatorname{grad} w_l \cdot \mathrm{d}\mathbf{A} \right) \tag{7.6}$$

$$= \sum_l c_{kl}\,\varphi_l. \tag{7.7}$$

The coefficients c_{kl}, which are found in the k-th row and l-th column of the matrix of influence coefficients, represent some normalized electric flux out of conductor k due to the potential at conductor l. An important property of this matrix is its symmetry, as the boundary $\partial\Omega$ can be moved from surrounding conductor k to surrounding the respective conductor l in the step of Eq. 7.6. This is shown by Lehner [65] for a homogeneous background material, or more generally by Simonyi [89].

The matrix of influence coefficients $\mathbf{C}_{\text{inf}}$ is closely related to the capacitance matrix and can be converted easily into capacitance matrix $\mathbf{C}$. While the matrix of influence coefficients $\mathbf{C}_{\text{inf}}$ is characterized by satisfaction of Eq. 7.1, the characteristic property of capacitance matrix $\mathbf{C}$ is the physical meaning of its matrix coefficients. The individual coefficients can be considered as the capacitance values of capacitors in an equivalent circuit. While the off-diagonal coefficient C_{kl} can be seen as the capacitance of a capacitor connecting the conductors k and l, the entries on the diagonal C_{kk} define the self-capacitance of conductor k, i.e., the capacitance between conductor k and ground.

The charge Q_k at conductor k of the equivalent circuit can be calculated by

$$Q_k = C_{kk}\varphi_k + \sum_{\substack{l \\ (l \neq k)}} C_{kl}\,(\varphi_k - \varphi_l)\,. \tag{7.8}$$

Comparing the previous equation with Eq. 7.1 reveals the relationship between the coefficients C_{kl} of the capacitance matrix and the coefficients c_{kl} of the matrix of influence coefficients and how to convert them:

$$C_{kl} = \begin{cases} \sum_m c_{km}, & \text{if } k = l \\ -c_{kl}, & \text{if } k \neq l \end{cases}, \tag{7.9}$$

$$c_{kl} = \begin{cases} \sum_m C_{km}, & \text{if } k = l \\ -C_{kl}, & \text{if } k \neq l \end{cases}. \tag{7.10}$$

In analogy to $\mathbf{C}_{\text{inf}}$ and $\mathbf{C}$, conductance matrices $\mathbf{G}_{\text{inf}}$ and $\mathbf{G}$ can be introduced. Matrix $\mathbf{G}$ will be called conductance matrix and $\mathbf{G}_{\text{inf}}$ matrix of conductance coefficients. The matrix of conductance coefficients $\mathbf{G}_{\text{inf}}$ relates a vector of resistive currents $\mathbf{I}$, which flow out of a conductor, to the potential of the conductors:

$$\mathbf{I} = \mathbf{G}_{\text{inf}}\varphi. \tag{7.11}$$

In place of 7.4, one has:

$$I_k = \int_{\partial\Omega} \mathbf{J} \cdot \mathrm{d}\mathbf{A} \tag{7.12}$$

$$= -\int_{\partial\Omega} \sigma \operatorname{grad} \varphi \cdot \mathrm{d}\mathbf{A} \tag{7.13}$$

$$= \sum_l \varphi_l \left(-\int_{\partial\Omega} \sigma \operatorname{grad} w_l \cdot \mathrm{d}\mathbf{A} \right) \tag{7.14}$$

$$= \sum_l g_{kl} \varphi_l . \tag{7.15}$$

Similar to the coefficients C_{kl}, the coefficients of the conductance matrix G_{kl} can be interpreted as the conductance values between conductors k and l. The dependence of the current at conductor k on the coefficients of the conductance matrix is given by:

$$I_k = G_{kk} \varphi_k + \sum_{\substack{l \\ (l \neq k)}} G_{kl} \left(\varphi_k - \varphi_l \right) . \tag{7.16}$$

Thus, the conversion rules of Eqs. 7.9 and 7.10 can be used in effectively the same way to convert between G_{kl} and g_{kl}.

Thanks to linearity, the matrices can be extracted easily from a few static field simulations. One possible way is using Eq. 7.1. For a system of n conductors, one needs at most n simulations of the static electric field with linearly independent potentials imposed as boundary condition to estimate $\mathbf{C}_{\mathrm{inf}}$. For example, if one sets the potential of one conductor k to one and the others to zero and calculates the charges at the conductors by integrating the electric flux density flowing through their surface, one obtains all values in the k-th column of matrix $\mathbf{C}_{\mathrm{inf}}$, since the value of the charge is equal to the value in the corresponding row. The matrix $\mathbf{G}_{\mathrm{inf}}$ can be obtained similarly from simulations of the stationary current field.

In cases, when capacitive current $\mathbf{I}_{\mathrm{c}}$ and resistive current $\mathbf{I}_{\mathrm{r}}$ are not of completely different magnitude, one has to calculate the total current by using matrix $\mathbf{C}_{\mathrm{inf}}$ as well as $\mathbf{G}_{\mathrm{inf}}$:

$$\mathbf{I} = \mathbf{I}_{\mathrm{r}} + \mathbf{I}_{\mathrm{c}} \tag{7.17}$$

$$= \mathbf{G}_{\mathrm{inf}} \varphi + \mathbf{C}_{\mathrm{inf}} \dot{\varphi} . \tag{7.18}$$

This equation allows the calculation of currents $\mathbf{I}(t)$ for an externally imposed evolution of the potential φ.

7.2 Nonlinear Matrices and Equivalent Circuits

The above introduction relied on the assumption of linearity and the applicability of the superposition principle, e.g., by assuming $\Phi(\mathbf{r}) = \sum_l \Phi_l w_l(\mathbf{r})$.

The superposition principle says that the influence of every source can be determined individually and that the total influence can be obtained by adding the contributions of the individual sources [92]. If capacitance or conductance is nonlinear, the assumption is no longer valid.

For example, consider a capacitor with a voltage-dependent capacitance $C(U)$, so that $Q = C(U)\,U$, and another, arbitrary voltage αU. The superposition principle is in general violated as:

$$C(\alpha U) \neq \frac{\alpha Q}{\alpha U} = \frac{Q}{U} = C(U). \tag{7.19}$$

Hence, the coefficients of any matrix relating charges and potentials have to be functions of the potential of the conductors.

Furthermore, the equations involving currents or energy are no longer fulfilled at the same time. There is no longer a single matrix that satisfies all the properties of Eq. 7.1 to 7.3 in the presence of nonlinear materials. The distinction between

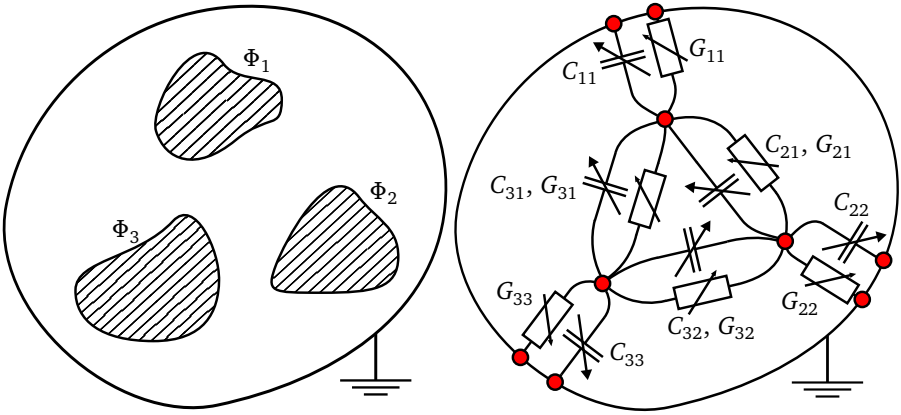

Figure 7.1: Three conductors at potential $\Phi_1, \ldots \Phi_3$ with grounded boundary (left) and an equivalent circuit representation (right) with variable capacitors and resistors. The circuit elements represent self- and mutual capacitances, respectively self- and mutual conductances.

capacitance and differential capacitance, which has already described in the section about nonlinear capacitances (Sec. 5.1), has to be taken into account.

While a nonlinear capacitance matrix can not completely substitute its linear equivalent, one can require that it satisfies at least one of the conditions. In the following, the nonlinear matrix of influence coefficients is supposed to satisfy the relationship $\mathbf{Q} = \mathbf{C}_{\mathrm{inf}}\varphi$. Similarly, the matrix of conductance coefficients has to satisfy $\mathbf{I} = \mathbf{G}_{\mathrm{inf}}\varphi$.

In analogy to Eq. 7.18, knowledge of these two matrices allows an approximate calculation of the currents which depends only on the vector of conductor potentials φ:

$$\mathbf{I}(t) = \mathbf{G}_{\mathrm{inf}}(\varphi(t))\,\varphi(t) + \frac{\mathrm{d}}{\mathrm{d}\,t}\Big(\mathbf{C}_{\mathrm{inf}}(\varphi(t))\;\varphi(t)\Big). \tag{7.20}$$

As shown, the matrices $\mathbf{C}_{\mathrm{inf}}(\varphi(t))$ and $\mathbf{G}_{\mathrm{inf}}(\varphi(t))$ are convertible into $\mathbf{C}(\varphi(t))$ and $\mathbf{G}(\varphi(t))$, from which a nonlinear equivalent circuit can be built. Such a nonlinear equivalent circuit with three conductors is shown in Fig. 7.1.

The following section presents a method to extract the properties of the circuit elements of an equivalent circuit. The data for the estimation of the properties are obtained from numerical field simulations, or possibly measurements. After extraction of the equivalent circuit parameters the matrices of influence coefficients $\mathbf{C}_{\mathrm{inf}}(\varphi(t))$ and of conductance coefficients $\mathbf{G}_{\mathrm{inf}}(\varphi(t))$ can be assembled and the currents flowing between the conductors can be calculated.

7.3 Extraction of Nonlinear Circuit Parameters

Normally the capacitance matrix is obtained from a series of electrostatic numerical simulations. This procedure becomes problematic in the presence of nonlinear materials. The straightforward approach described in Sec. 7.2, which consists of setting the potential of the individual conductors successively to one or any other value and observe the resulting charge to assemble the capacitance matrix, fails as the values of the coefficients depend on potential. While it is possible to repeat the calculation for different potential values and interpolate the matrix coefficients, this does not resolve the problem.

The principal reason for the inadequacy of such an approach is the fact that the capacitive coupling is no direct function of the conductor potentials. The coupling between two conductors depends principally on the potential difference and not on the absolute values of the potentials. Therefore, the approach will not provide satisfactory results for nonlinear problems, unless the potential of all nearby conductors is close to zero, if one conductor is excited.

By contrast, the method, which is described in the following, depends implicitly on the difference between the conductor potentials. Its starting point is the estimation of the circuit element parameters of a nonlinear equivalent circuit. In many respects it is similar to the approach described in Sec. 5.4 for the characterization of materials. In fact, its principal practical differences are the extension of the previous approach from scalar to matrix values and its different purpose. Whereas the extraction of parameters by means of least squares had been presented as an approach to characterize materials from measurement data, it is now employed to create models with reduced number of unknowns from field simulations.

The capacitance and conductance of each capacitor or conductor in an equivalent circuit according to Fig. 7.1 is supposed to depend only on the difference in potential between their terminal nodes. For example, the capacitance between the conductors k and l is assumed to be a function of $|\Phi_k - \Phi_l|$:

$$C_{kl} = C_{kl}(|\Phi_k - \Phi_l|). \tag{7.21}$$

The function which describes the voltage-dependency is not known, but it is required to depend linearly on some unknown parameters C_{kl}^i:

$$C_{kl}(\Delta\Phi) = \sum_i C_{kl}^i w_i(\Delta\Phi), \tag{7.22}$$

where $\Delta\Phi$ is the absolute value of the potential difference $\Delta\Phi = |\Phi_k - \Phi_l|$ and w_i some basis functions, as in Sec. 5.4. For example, if the capacitance is estimated as a polynomial of second order, the equation becomes:

$$C_{kl}(\Delta\Phi) = C_{kl}^0 + C_{kl}^1 \Delta\Phi + C_{kl}^2 \cdot \Delta\Phi^2. \tag{7.23}$$

This means that the extraction of an entry C_{kl} of the capacitance matrix requires the determination of $n+1$ unknowns for a polynomial ansatz of order n. As the equivalent circuit of a multiconductor system with m conductors has $m(m+1)/2$ capacitors, one has to determine $(n+1)m(m+1)/2$ unknowns for the capacitance matrix and an equivalent number of unknowns for the conductance matrix. Thus, the number of unknowns can easily become large, although it will always be much lower than for a field simulation.

In the case of the material characterization the parameters are estimated by minimizing the difference between measured and simulated current densities. In the present case, the procedure is similar. The simulated total current $\mathbf{I}_{\text{sim}}$ of the equivalent circuit at a certain moment t_i is the sum of resistive and capacitive current:

$$\mathbf{I}_{\text{sim}}(t_i) = \mathbf{G}_{\text{inf}}(t_i)\varphi(t_i) + \frac{\mathrm{d}}{\mathrm{d}\,t}\Big(\mathbf{C}_{\text{inf}}(t)\varphi(t)\Big)_{|_{t=t_i}}. \tag{7.24}$$

Its value depends on the value of the parameters C_{kl}^{i} and G_{kl}^{i} that indirectly characterize the matrix of influence coefficients $\mathbf{C}_{\text{inf}}$ and of conductance coefficients $\mathbf{G}_{\text{inf}}$, as well as on the vectors φ and $\dot{\varphi}$ that describe the potential and its time derivative for all conductors. $\mathbf{I}_{\text{sim}}(t_i)$ is a vector which describes the current flowing out of each of the conductors at moment t_i. This equation can be written in the form of a system of linear equations with respect to the unknown parameters C_{kl}^{i} and G_{kl}^{i}. By concatenating the systems for a certain number of time moments, e.g., p, a matrix with $m\,p$ rows and $(n+1)\,m\,(m+1)/2$ columns is obtained:

$$\begin{pmatrix} \mathbf{I}_{\text{sim}}(t_1) \\ \vdots \\ \mathbf{I}_{\text{sim}}(t_p) \end{pmatrix} = \begin{pmatrix} \mathbf{G}_{\text{inf}}(t_1)\varphi(t_1) & + \frac{\mathrm{d}}{\mathrm{d}\,t}\left(\mathbf{C}_{\text{inf}}(t)\varphi(t)\right)_{|_{t=t_1}} \\ \vdots & \vdots \\ \mathbf{G}_{\text{inf}}(t_p)\varphi(t_p) & + \frac{\mathrm{d}}{\mathrm{d}\,t}\left(\mathbf{C}_{\text{inf}}(t)\varphi(t)\right)_{|_{t=t_p}} \end{pmatrix}. \tag{7.25}$$

However, the parameters are defined as coefficients for the conductors and capacitors of an equivalent circuit. The current $I_{\text{sim},k}$ flowing out of conductor k at an arbitrary moment can be moment can be written as:

$$\begin{aligned} I_{\text{sim},k} =& G_{kk}(|\Phi_k|)\Phi_k + \sum_{\substack{l \\ (k\neq l)}} G_{kl}(|\Phi_k - \Phi_l|)\,(\Phi_k - \Phi_l) \\ &+ \frac{\mathrm{d}}{\mathrm{d}\,t}\left(C_{kk}(|\Phi_k|)\Phi_k + \sum_{\substack{l \\ (k\neq l)}} C_{kl}(|\Phi_k - \Phi_l|)\,(\Phi_k - \Phi_l) \right) && (7.26) \\ =& G_{kk}(|\Phi_k|)\Phi_k + \sum_{\substack{l \\ (k\neq l)}} G_{kl}(|\Phi_k - \Phi_l|)\,(\Phi_k - \Phi_l) \\ &+ C_{kk}(|\Phi_k|)\dot{\Phi}_k + \sum_{\substack{l \\ (k\neq l)}} C_{kl}(|\Phi_k - \Phi_l|)\,(\dot{\Phi}_k - \dot{\Phi}_l) && (7.27) \\ &+ \frac{\mathrm{d}\,C_{kk}(|\Phi_k|)}{\mathrm{d}\,t}\,\Phi_k + \sum_{\substack{l \\ (k\neq l)}} \frac{\mathrm{d}\,C_{kl}(|\Phi_k - \Phi_l|)}{\mathrm{d}\,t}\,(\Phi_k - \Phi_l). && (7.28) \end{aligned}$$

The parameters are finally estimated by minimizing the difference between the simulated total current I_{sim} of the equivalent circuit and the reference solution I_{ref}:

$$\underset{C_{kl}^{i},G_{kl}^{i}}{\text{minimize}} \left\| \mathbf{I}_{\text{sim}} - \mathbf{I}_{\text{ref}} \right\|_2, \tag{7.29}$$

where $\mathbf{I}_{\text{ref}}$ is a vector of values extracted from numerical field simulations. It assumes the position that measured current density $\mathbf{J}_{\text{meas}}$ had for the material characterization. $\mathbf{I}_{\text{sim}}$ is the product of a matrix $\mathbf{A}$ with a vector of the unknown parameters, which describe the circuit elements:

$$\underset{G_{ij}^k, C_{ij}^k}{\text{minimize}} \left\| \mathbf{A} \begin{pmatrix} \vdots \\ G_{ij}^k \\ \vdots \\ C_{ij}^k \\ \vdots \end{pmatrix} - \mathbf{I}_{\text{ref}} \right\|_2 . \tag{7.30}$$

After solution of the least-square problem, the properties of the circuit elements and the entries of the capacitance matrix $\mathbf{C}$ and conductance matrix $\mathbf{G}$ can be calculated for any given set of conductor potentials φ. The current flowing between the conductors is calculated by determining the numerical values of the capacitance and conductance matrix from present potentials, converting the matrices into matrix of influence coefficients $\mathbf{C}_{\text{inf}}$ and matrix of conductance coefficients $\mathbf{G}_{\text{inf}}$, and finally using Eq. 7.20.

To apply the described procedure, data from a reference solution $\mathbf{I}_{\text{ref}}$ are needed, which were said to be obtained from numerical field simulations. More precisely, they are obtained from an electro-quasistatic time-domain simulation of the multiconductor model. The conductors are excited by linearly independent excitation signals, ideally similar in frequency and amplitude to the signals, for which one wishes to obtain the equivalent circuit model. At the individual time steps t_i, the potentials $\varphi_l(t_i)$, the current flowing out of the respective conductor $I_l(t_i)$ and possibly the time-derivative value $\dot{\varphi}_l(t_i)$ are recorded to a file. The current $I_l(t_i)$ is calculated by integration over the surface of the conductor l:

$$I_l = \int_{\partial\Omega_l} \left(\mathbf{J} + \frac{\partial \mathbf{D}}{\partial t} \right) \cdot \mathrm{d}\mathbf{A} \tag{7.31}$$

$$= -\int_{\partial\Omega_l} \left((\sigma(|\operatorname{grad}\varphi|) \operatorname{grad}\varphi - \frac{\partial}{\partial t} (\varepsilon_{\text{r}}(|\operatorname{grad}\varphi|)\, \varepsilon_0 \operatorname{grad}\varphi) \right) \cdot \mathrm{d}\mathbf{A} \tag{7.32}$$

These recorded data contain all the information that is needed to estimate the parameters of the equivalent circuit model and its associated matrices.

7.4 Nonlinear Equivalent Circuit of Multi-Conductor Cable

The calculation of currents between the conductors of a multiconductor system is shown for a cable configuration with fictional nonlinear properties. A nonlinear

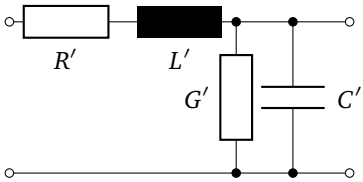

Figure 7.2: Equivalent circuit of an elementary component of a two-wire transmission line system, which allows the calculation of voltage and current along the line by solving the telegrapher's equation. Application of the equivalent-circuit characterization approach leads to an estimation of nonlinear capacitance C' and conductance G' per unit length.

equivalent-circuit based model with low number of degree of freedom can be derived that provides results, which are similar to those of the computationally much more expensive field simulation.

In the case of a cable, the extracted equivalent circuit can be interpreted as describing the conductance and capacitance per unit length, as represented by G' and C' in Fig. 7.2 for a simple two-conductor system. Therefore, the method provides half of the information needed to simulate the propagation of a current and

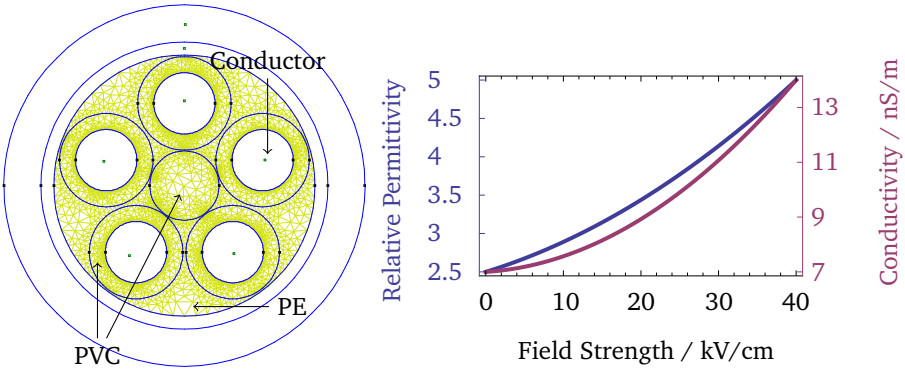

Figure 7.3: Geometry of the studied cable model, a screened PVC control cable and the fictional material properties of the PVC material. Neither the material properties nor the excitation is realistic for the given cable, but they serve to compare the results of a nonlinear equivalent circuit model with those from a field simulation.

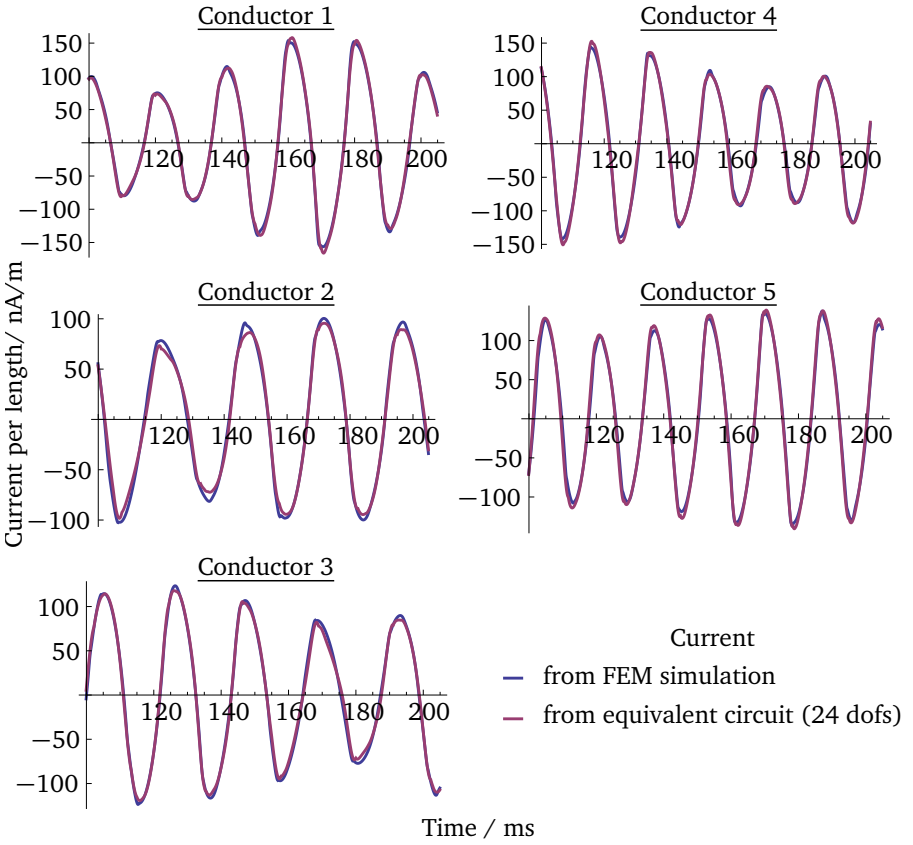

Figure 7.4: Comparison of currents according to an electro-quasistatic finite element simulation and the derived nonlinear equivalent circuit. The capacitors and conductors of the equivalent circuit are modeled as polynomials of order three. Under consideration of symmetry, this leads to a model with only 24 degrees of freedom (dofs). The calculated current using the capacitance and conductance matrices derived from the nonlinear equivalent circuit largely agrees with the current from the field simulations and shows the same distorted sine shape. Differences between finite element and equivalent circuit currents can be observed close to current peaks.

voltage signal along a nonlinear transmission line. However, the other parameters, R' and L', have to be obtained otherwise.

For the purpose of demonstrating the method, a model with more than two wires is used. Its geometry corresponds to the cross section of a common screened polyvinyl chloride (PVC) control cable, sold under the name (see Fig. 7.3), but the material properties have been altered.

First, the conductivity of the PVC material has been raised to a level at which the resistive currents are comparable in magnitude to the capacitive ones at about 50 Hz. Thereby, none of the two matrices is negligible and the estimation of both matrices makes sense. Second, conductivity and permittivity of the PVC material have been replaced by second-order polynomials with respect to field strength to obtain a nonlinear problem (see Fig. 7.3).

The model is simulated by solving the electro-quasistatics equation in time domain. Each of the conductors is excited by a voltage signal with the same amplitude, but different initial phase angle and frequency, which differ by some percent from 50 Hz.

The results of this simulation are used to generate a model of reduced order. This order depends on the number of coupling conductances and capacitances. Since the simulated cable consists of five wires plus ground, its equivalent circuit has 15 conductors and capacitors. However, this number is reduced to three thanks to symmetry:

- Capacitance/Conductance between conductor and ground.
- Capacitance/Conductance between two neighboring conductors.
- Capacitance/Conductance between two distant conductors.

As permittivity and conductivity are quadratic functions of field strength, the capacitances and conductances are necessarily also at least quadratic. Thus, each of the three equivalent conductors and capacitors has at least three parameters, leading to a minimum total number of 18. Since the field between the conductors is non-homogeneous and the order of the material nonlinearity does not translate directly to the cable geometry, a higher order might be necessary for the equivalent conductors and capacitors. In any case, the equivalent circuit model is of much lower order than the field simulation model.

In Fig. 7.4 the model with nonlinear capacitance and conductance matrix is compared to the original electro-quasistatic finite element results. The figure shows the sum of resistive and capacitive current per meter flowing from the individual conductors to the other conductors and ground. The matrices have been obtained by evaluation of the finite element results for the interval 0 s to 1 s. However, given the spread of the conductor excitation frequencies, the current and voltage data

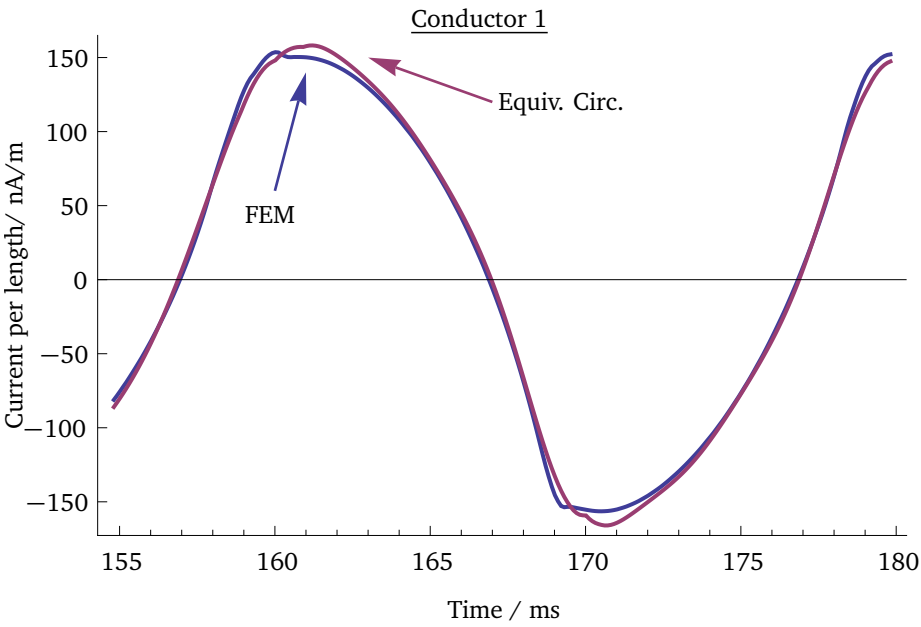

Figure 7.5: Enlarged view of the current flowing out of the first wire obtained from an electro-quasistatic field simulation and the derived equivalent circuit model. Although the two curves are clearly distinct, at least close to the current peaks, the equivalent circuit model is capable of largely reproducing the field simulation current.

provide few new information after about 0.2 s or 10 periods. Thus, a much shorter simulation duration is sufficient for the purpose of extracting the nonlinear matrices. By contrast, the voltage and current data of the first few milliseconds have to be excluded, as the initial field distribution influences the quality of the nonlinear capacitance and conductance matrix in "steady state".

The blue curves represent the current from the finite element simulation. In combination with the voltage information these curves constitute the input data for the derivation of an equivalent circuit model with nonlinear capacitance and conductance matrices. In purple, the currents calculated from these nonlinear capacitances and conductances are shown. The model consists of six circuit elements, the three above-mentioned conductors and capacitors, of third polynomial order, which leads to 24 degrees of freedom. The current calculated with this equivalent

circuit model agrees relatively well with the finite element current. Differences can be seen at the current peaks. Increasing the polynomial degree of the model reduces the difference, though only by a limited amount. For example, the average of the error $|I_i^{Eq} - I_i^{FEM}|/|I_i^{FEM}|$, with conductor number i, decreases from 5.96 % to 5.85 %, when the properties of the circuit elements are modeled as fifth-order polynomials instead of third-order polynomials. Most of the error has to be attributed to the limitations of the model, as ignoring the influence of third conductors.

In Fig. 7.5 a part of the previous figure is shown enlarged. The purple curve of the equivalent-circuit based model is quite similar to the blue finite element solution with some differences close to the current peaks.

8 Summary and Outlook

The last chapters of this thesis presented possible solutions to various problems related to varistors and microvaristors. While the individual sections treat diverse, independent problems, some of the sections can be considered as forming part of a chain of actions. The chain reaches from the characterization of a material for the creation of a numerical model to the generation of a simple equivalent circuit from numerical field simulations.

The simple, yet apparently unknown least-squares based characterization method presented in Ch. 5 is a powerful tool to estimate the electrical properties of a material. Both, conductivity and relative resistivity are estimated simultaneously as field-strength dependent functions. This characterization method possesses two great advantages: It requires relatively few measurement data and the shape of the excitation signal can be (almost) arbitrary. If necessary, an entire characteristic curve can be extracted directly from a single lightning-current pulse measurement.

The application of this approach to a test sample consisting of microvaristor-embedded silicone rubber has led to a better understanding of this material. As variously suspected, the nonlinearity of (micro-)varistor materials includes relative permittivity. This assumption is strongly supported by the presented results.

Furthermore, the results from a more detailed examination of the data indicate the presence of some kind of previously unknown memory effect. Section 5.5 describes the first attempts to combine nonlinear material behavior with relaxation. While the results can hardly be considered satisfactory, they are hopefully of use for later studies.

Once the material characteristics are known, one can continue with numerical field simulations. As already mentioned in the introduction of this thesis, the simulation of a lightning-current pulse injected into a high-voltage surge arrester has been excluded, although this had initially been the principal objective. By contrast, the chapter on surge arrester simulations (Ch. 6) contains a short section on the calculation of a thermally stationary state by iteratively coupling a transient electro-quasistatic simulation with the static heat conduction problem. By using this method, a stationary state in thermal equilibrium is obtained. Reassuringly the same stationary state is reached for different initial conditions. The main questions concerning this kind of simulation are the importance of knowing the thermally stationary state, opposed to knowing the limits of thermal stability, and the accuracy, given the uncertainty about the modeling parameters. Maybe the

possibility to calculate the thermally stationary state can be used in conjunction with measurements to reduce the modeling parameter uncertainty.

The second presented approach for the simulation of surge arresters introduces for the first time an envelope equation model to electrical power engineering. The purpose of this innovative approach is to help with the determination of the thermal stability limits. This important problem is computationally too expensive for a brute force simulation. While the results are clearly better than expected by the author and show the potential of this ansatz, they demonstrate also the limitations of this method. One has to observe, whether the envelope equation can compete with alternative methods in development.

After the numerical field simulation the results have to be evaluated. Often the simulations serve to extract capacitance and other matrices, which can then be inserted into other programs. In Ch. 7 an approach to derive an equivalent circuit with nonlinear resistors and capacitors from a transient electro-quasistatic field simulation is presented. This nonlinear equivalent circuit constitutes an intermediate step towards nonlinear capacitance and conductance matrices. These matrices can be used as a tool to simulate the propagation of signals on wires with nonlinear resistive stress control materials or other nonlinear problems.

Appendix

Acronyms

a.c.	alternating current
ABC	absorbing boundary condition
BEM	boundary element method
d.c.	direct current
DFG	Deutsche Forschungsgemeinschaft
dof	degree of freedom
EQS	electro-quasistatic
FD	finite differences (method)
FDTD	finite differences in time domain (method)
FEM	finite element method
FIT	finite integration technique
GRP	glass-reinforced plastic
HV	high-voltage
IBC	impedance boundary condition
IGBT	insulated-gate bipolar transistor
MCOV	maximum continuous operating voltage
MO	metal oxide
MoM	method of moments
MOV	metal-oxide varistor
NTC	negative temperature coefficient
OLS	ordinary least squares
PML	perfectly matched layer
PVC	polyvinyl chloride
RC	resistor-capacitor

rms	root mean squared
SDIRK	singly-diagonally implicit Runge-Kutta (method)
SiC	silicon carbide
SPD	surge-protective device
SVD	singular value decomposition
UHV	ultra-high voltage
VDR	voltage-dependent resistor
ZnO	zinc oxide

Lists of Symbols

Notational Conventions

$\mathbf{x}$	vector named x
$\mathbf{A}$	matrix named A
$\dot{x}$	time derivative of x
$\tilde{x}$	estimate or prediction of x
$\hat{x}$	peak value of x
$\underline{x}$	phasor of x
j	imaginary unit
x'	distributed quantity x
x_{sim}	quantity x obtained through numerical simulation
x_{ref}	quantity x used as reference for comparisons
$\mathbf{x}^{\text{T}}$	transposed of $\mathbf{x}$
$\mathbf{X}^{-1}$	inverse of $\mathbf{X}$

Electrical Symbols

α	nonlinearity coefficient	
$\mathbf{B}$	magnetic flux density	T
C	capacitance	F
c	wave propagation speed	m/s
C_{d}	differential capacitance	F
$\mathbf{C}_{\text{inf}}$	matrix of influence coefficients	F
C'	distributed capacitance	F/m
$\mathbf{C}$	capacitance matrix	F

$\mathbf{D}$	displacement flux density	$\mathrm{C/m^2}$
$\mathbf{E}$	field strength	V/m
ε	permittivity	F/m
$\hat{\varepsilon}$	permittivity (per second) of a linear, inert material	F/(m s)
ε_∞	high-frequency limit of dielectric permittivity	F/m
ε_0	electric constant (or vacuum permittivity)	F/m
ε_r	relative permittivity	1
ε_s	low-frequency limit of dielectric permittivity	F/m
f	frequency	Hz
G	conductance	S
$\mathbf{G}_\mathrm{inf}$	matrix of conductance coefficients (in analogy to $\mathbf{C}_\mathrm{inf}$)	S
G'	distributed conductance	S/m
$\mathbf{G}$	conductance matrix	S
$\mathbf{H}$	magnetic field strength	A/m
I	(static) current	A
i	(time-varying) current	A
$\mathbf{I}$	vector of currents	A
$\mathbf{I}_\mathrm{c}$	vector of capacitive currents	A
$\mathbf{I}_\mathrm{r}$	vector of resistive currents	A
$\mathbf{J}$	current density	$\mathrm{A/m^2}$
$\mathbf{J}_\mathrm{c}$	capacitive current density	$\mathrm{A/m^2}$
$\mathbf{J}_\mathrm{r}$	resistive current density	$\mathrm{A/m^2}$
λ	wave length	m
L'	distributed inductance	H/m
μ	permeability	$\mathrm{kg\,m/(A^2\,s^2)}$
μ_0	permeability of free space	H/m
μ_r	relative permeability	1
ω	angular frequency	1/s
$\mathbf{P}$	polarization density	T
$\mathbf{p}_\mathrm{n}$	electric dipole moment (of particle n)	C m
φ	scalar potential	V
$\underline{\Phi}$	phasor potential	V
φ	vector of potentials	V
q	electric charge	C
$\mathbf{Q}$	vector of charges	C
ϱ	charge density	$\mathrm{C/m^3}$
ϱ_0	initial charge density	$\mathrm{C/m^3}$
R'	distributed resistance	Ω/m
σ	electrical conductivity	S/m

$\bar{\sigma}_\mathrm{I}$	current-equivalent conductivity (Sec. 6.2)	S/m
$\bar{\sigma}_\mathrm{P}$	power-equivalent conductivity (Sec. 6.2)	S/m
$\hat{\sigma}$	conductivity (per second) of a linear, inert material	S/(m s)
σ_∞	conductivity at high frequency	S/m
σ_s	conductivity at low frequency	S/m
T	period length	s
τ	characteristic time	s
τ_diff	diffusion time constant	s
τ_0	relaxation time constant	s
τ_relax	(dielectric) relaxation time constant	s
U	(static) voltage	V
u	(time-varying) current	A
U_c	maximum continuous operating voltage (MCOV)	V
U_s	maximum rms voltage of system	V
W	energy	J
w_e	electric energy density	$\mathrm{J/m^3}$
w_m	magnetic energy density	$\mathrm{J/m^3}$

Thermodynamic Symbols

α	diffusivity	$\mathrm{m^2/s}$
c_p	specific heat capacity	J/(kg K)
c_v	volumetric heat capacity	$\mathrm{J/(m^3\,K)}$
ϵ	emissivity	1
h	heat transfer coefficient	$\mathrm{W/m^2}$
λ	thermal conductivity	W/(K m)
$\dot{Q}$	(net) heat flux	W
$\dot{\mathbf{q}}$	heat flux density	$\mathrm{W/m^2}$
ϱ	mass density	$\mathrm{kg/m^3}$
σ_SB	Stefan–Boltzmann constant	$\mathrm{W/(K^4\,m^2)}$
ϑ	temperature	K
ϑ_∞	far-field temperature in a gas/fluid	K
ϑ_sur	temperature of the surrounding environment	K
$\bar{w}$	time-averaged heat generation	$\mathrm{W/m^3}$
$\dot{w}_\mathrm{gen}$	heat generation density	$\mathrm{W/m^3}$

Finite Element Symbols

$\mathbf{B}$	matrix associated with boundary conditions

$\mathbf{K}_\varepsilon$	Stiffness matrix associated with electric permittivity
$\mathbf{K}_\lambda$	Stiffness matrix associated with thermal conductivity
$\mathbf{K}_\sigma$	Stiffness matrix associated with electric conductivity
$\mathbf{M}_{c_p\varrho}$	Mass matrix associated with volumetric heat capacity
N_i	i-th basis function
θ	Factor characterizing the θ-method for time integration ($0 \leq \theta \leq 1$)
r	residual
w_i	i-th weighting function
$\mathbf{w}_\mathrm{V}$	vector associated with volumetric heat generation

General and Other Symbols

A	area	m^2
B_{ij}	i-th B-Spline of order j	
d	thickness	m
δ	Dirac operator	
Δt	length of time interval	s
η	relative error	1
L	characteristic length	m
$\mathbf{r}$	location vector	m
t	time	s
$\mathbf{x}$	vector of unknowns	

List of Figures

List of Tables

Bibliography

[1] H. D. Baehr and K. Stephan, *Heat and Mass Transfer*. Berlin: Springer, 2006.

[2] C. A. Balanis, *Advanced Engineering Electromagnetics*, 2nd ed. New York: Wiley, 1989.

[3] C. M. Barrado, E. R. Leite, P. R. Bueno, E. Longo, and J. A. Varela, "Thermal conductivity features of ZnO-based varistors using the laser-pulse method," *Materials Science and Engineering A*, vol. 371, no. 1-2, pp. 377–381, Apr. 2004. [Online]. Available: http://www.sciencedirect.com/science/article/B6TXD-4C09KCG-3/2/b43fbdb98c7c6594107adb9eecba8130

[4] M. Bartkowiak, "Energy handling capability of ZnO varistors," *J. Appl. Phys.*, vol. 79, no. 11, pp. 8629–8633, Jun. 1996.

[5] M. Bartkowiak, M. G. Comber, and G. D. Mahan, "Failure modes and energy absorption capability of ZnO varistors," *IEEE Transactions on Power Delivery*, vol. 14, no. 1, p. 152–162, Jan. 1999.

[6] K.-J. Bathe, *Finite-Elemente-Methoden*. Berlin: Springer, 2002.

[7] R. Bauer, "Numerische Berechnung von Kapazitäten in dreidimensionalen Verdrahtungsstrukturen," Dissertation, Technische Universität Wien, Wien, Nov. 1994. [Online]. Available: http://www.iue.tuwien.ac.at/phd/bauer/diss.html

[8] G. Benderskaya, "Numerical methods for transient field-circuit coupled simulations based on the finite integration technique and a mixed circuit formulation," Dissertation, Technische Universität Darmstadt, Darmstadt, 2007.

[9] D. R. Clarke, "Varistor ceramics," *Journal of the American Ceramic Society*, vol. 82, no. 3, pp. 485–502, 1999. [Online]. Available: http://dx.doi.org/10.1111/j.1151-2916.1999.tb01793.x

[10] R. W. Clough, "The finite element method in plane stress analysis," in *Proceedings, 2nd Conference on Electronic Computation, A.S.C.E. Structural Division*, Pittsburgh, 1960.

[11] R. Courant, “Variational methods for the solution of problems of equilibrium and vibrations,” *Bull. Amer. Math. Soc*, vol. 49, no. 1, p. 23, 1943.

[12] Y. A. Çengel, *Heat transfer : a practical approach*. Boston, Mass.: WBC McGraw-Hill, 1998.

[13] A. J. Davies, *The finite element method : an introduction with partial differential equations*. Oxford; New York: Oxford University Press, 2011.

[14] C. De Boor, “B(asic)-spline basics,” in *Fundamental Developments of Computer-Aided Geometric Modeling*. London: Academic Press, 1993, pp. 27–49.

[15] C. de Boor, *A practical guide to splines*. New York: Springer, 2001.

[16] F. Denz, E. Gjonaj, T. Weiland, M. Tuczek, and V. Hinrichsen, “Electric and thermal reaction of zinc oxide to current impulses,” in *30th ICLP 2010, Cagliari, Italy, 12.-16.9.2010, paper 6B-1331*, 2010. [Online]. Available: http://tubiblio.ulb.tu-darmstadt.de/48583/

[17] F. Denz, E. Gjonaj, and T. Weiland, “Nonlinear characterization and simulation of zinc-oxide surge arresters,” in *Scientific Computing in Electrical Engineering SCEE 2010*, ser. Mathematics in Industry, B. Michielsen and J.-R. Poirier, Eds. Springer Berlin Heidelberg, 2012, pp. 213–221. [Online]. Available: http://dx.doi.org/10.1007/978-3-642-22453-9_23

[18] P. Deuflhard and F. Bornemann, *Numerische Mathematik 2: Gewöhnliche Differentialgleichungen*. Berlin: Walter de Gruyter, 2008.

[19] L. Donzel, T. Christen, R. Kessler, F. Greuter, and H. Gramespacher, “Silicone composites for HV applications based on microvaristors,” in *Solid Dielectrics, 2004. ICSD 2004. Proceedings of the 2004 IEEE International Conference on*, vol. 1, 2004, pp. 403–406.

[20] L. Donzel, F. Greuter, and T. Christen, “Nonlinear resistive electric field grading part 2: Materials and applications,” *Electrical Insulation Magazine, IEEE*, vol. 27, no. 2, pp. 18–29, 2011.

[21] K. Eda, “Zinc oxide varistors,” *Electrical Insulation Magazine, IEEE*, vol. 5, no. 6, pp. 28–30, 1989. [Online]. Available: 10.1109/57.44606

[22] ——, “Destruction mechanism of ZnO varistors due to high currents,” *Journal of Applied Physics*, vol. 56, no. 10, pp. 2948–2955, 1984. [Online]. Available: http://link.aip.org/link/?JAP/56/2948/1

[23] R. Einzinger, “Metal oxide varistor action – a homojunction breakdown mechanism,” *Applications of Surface Science*, vol. 1, no. 3, pp. 329–340, May 1978. [Online]. Available: http://www.sciencedirect.com/science/article/B6X3T-46RVJJ5-2/2/aae00132aa9fa5169f6c646f77cb97dc

[24] ——, “Metal oxide varistors,” *Annual Review of Materials Science*, vol. 17, no. 1, pp. 299–321, 1987. [Online]. Available: http://arjournals.annualreviews.org/doi/abs/10.1146/annurev.ms.17.080187.001503

[25] G. Engeln-Müllges and F. Reutter, *Numerik-Algorithmen*. Düsseldorf: VDI Verlag, 1996.

[26] A. C. Eringen, *Electrodynamics of continua*. New York: Springer-Verlag, 1990, vol. 1.

[27] R. Eymard, T. Gallouët, and R. Herbin, “Finite volume methods,” *Handbook of numerical analysis*, vol. 7, pp. 713–1018, 2000.

[28] Y. Feldman, A. Puzenko, and Y. Ryabov, “Dielectric relaxation phenomena in complex materials,” in *Fractals, Diffusion, and Relaxation in Disordered Complex Systems*, ser. Advances in Chemical Physics. John Wiley & Sons, 2006, vol. 133.

[29] F. Fernández and R. Diáz, “Metal-oxide surge arrester model for fast transient simulations,” in *Proceedings of the IPST’01*, Rio de Janeiro, Jun. 2001.

[30] S. H. Foulger, “Electrical properties of composites in the vicinity of the percolation threshold,” *Journal of Applied Polymer Science*, vol. 72, no. 12, pp. 1573–1582, 1999. [Online]. Available: http://dx.doi.org/10.1002/(SICI)1097-4628(19990620)72:12<1573::AID-APP10>3.0.CO;2-6

[31] J. B. J. Fourier, *Théorie analytique de la chaleur*. Paris: Firmin Didot, Père et Fils, 1822.

[32] J. B. J. Fourier and S. D. Poisson, “Mémoire sur la propagation de la chaleur dans les corps solides,” in *Oeuvres de Fourier*. Paris: Gauthiers-Villars et Fils, 1890, vol. 2. [Online]. Available: http://gallica.bnf.fr/ark:/12148/bpt6k33707/f220

[33] R. W. Freund and R. H. Hoppe, *Stoer, Bulirsch: Numerische Mathematik 1*. Berlin: Springer, 2007.

[34] L. Gaul, M. Kögl, and M. Wagner, *Boundary Element Methods for Engineers and Scientists. An Introductory Course with Advanced Topics.* Berlin: Springer, 2003.

[35] G. Genty, P. Kinsler, B. Kibler, and J. Dudley, "Nonlinear envelope equation modeling of sub-cycle dynamics and harmonic generation in nonlinear waveguides," *Optics express*, vol. 15, no. 9, p. 5382–5387, 2007.

[36] G. H. Golub and C. F. Van Loan, *Matrix computations*, 3rd ed. Baltimore: Johns Hopkins University Press, 1996.

[37] U. Grigull and H. Sandner, *Wärmeleitung*. Berlin; Heidelberg; New York; London; Paris; Tokyo; Hong Kong: Springer, 1990.

[38] T. K. Gupta, "Application of Zinc Oxide Varistors," *Journal of the American Ceramic Society*, vol. 73, no. 7, p. 1817–1840, 1990. [Online]. Available: http://dx.doi.org/10.1111/j.1151-2916.1990.tb05232.x

[39] R. Göhler, M. Tuczek, and V. Hinrichsen, "Optimierung der Potentialverteilung von MO-Überspannungsableitern durch externe Steuerung," in *Feldsteuernde Isoliersysteme: Werkstoffe, Design, Prüfung und Simulation ; Vorträge des ETG-Workshops vom 22. bis 23. November 2011 in Darmstadt*. Berlin: VDE-Verlag, 2011.

[40] A. Haddad, "ZnO surge arresters," in *Advances in High Voltage Engineering*, ser. IEE Power & Energy. London: IEE, 2009, no. 40, pp. 191–244.

[41] C. Hafner, *Post-modern electromagnetics : using intelligent Maxwell solvers*. Chichester; New York: John Wiley, 1999.

[42] M. Hanke-Bourgeois, *Grundlagen der Numerischen Mathematik und des Wissenschaftlichen Rechnens*. Wiesbaden: Vieweg + Teubner, 2009.

[43] J. Harnden, F. Martzloff, W. Morris, and F. Golden, *Metal-Oxide Varistor: A New Way to Suppress Transients*. New York: Electronics, Oct. 1972.

[44] H. Haus and J. R. Melcher, *Electromagnetic Fields and Energy*. Englewood Cliffs: Prentice-Hall (downloadable from Massachusetts Institute of Technology: MIT OpenCourseWare), 1989, Licence: Creative Commons Attribution – NonCommercial – Share Alike. [Online]. Available: http://ocw.mit.edu

[45] A. R. Hileman, *Insulation Coordination for Power Systems*, ser. Power Engineering. New York: Marcel Dekker, 1999, no. 9.

[46] V. Hinrichsen, "Metal-oxide surge arrester fundamentals," *Siemens AG,*, no. 1, 2001.

[47] V. Hinrichsen, R. Göhler, M. Clemens, T. Steinmetz, and P. Riffon, "External grading systems for UHV metal-oxide surge arresters a new approach to numerical simulation and dielectric testing," in *Cigré Session*, Paris, Aug. 2008.

[48] J. R. Howell, R. Siegel, and M. P. Mengüuç, *Thermal radiation heat transfer*, 5th ed. Boca Raton, Fla.: CRC Press, 2011.

[49] A. Hrennikoff, "Solution of problems of elasticity by the framework method," *Journal of applied mechanics*, vol. 8, no. 4, pp. 169–175, 1941.

[50] IEC, "IEC 60038 ed. 6.2," Geneva, 2007.

[51] ——, "IEC 60099-4 ed. 2.1," Geneva, 2007.

[52] IEEE Working Group 3.4.11 Application of Surge Protective Devices Subcommittee Surge Protective Devices, "Modeling of metal oxide surge arresters," *Power Delivery, IEEE Transactions on*, vol. 7, no. 1, pp. 302–309, Jan. 1992. [Online]. Available: http://ieeexplore.ieee.org/xpls/abs_all.jsp?arnumber=108922

[53] F. P. Incropera, D. P. Dewitt, T. L. Bergman, and A. S. Lavine, *Principles of Heat and Mass Transfer*. Singapore: John Wiley & Sons, 2013.

[54] Institution of Electrical Engineers, *The lightning flash*, ser. IEE power & energy series. London: Institution of Electrical Engineers, 2003, no. 34.

[55] J. D. Jackson, *Classical electrodynamics*. New York: Wiley, 1999.

[56] A. Janotti and C. G. V. d. Walle, "Fundamentals of zinc oxide as a semiconductor," *Reports on Progress in Physics*, vol. 72, no. 12, p. 126501, 2009. [Online]. Available: http://stacks.iop.org/0034-4885/72/i=12/a=126501

[57] M. Kaviany, *Essentials of Heat Transfer*. Cambridge University Press, 2011.

[58] H. Klingbeil, *Elektromagnetische Feldtheorie. Ein Lehr- und Übungsbuch*. Wiesbaden: Vieweg + Teubner, 2011.

[59] M. Kobayashi, M. Mizuno, T. Aizawa, M. Hayashi, and K. Mitani, "Development of zinc-oxide non-linear resistors and their applications to gapless surge arresters," *IEEE Transactions on Power Apparatus and Systems*, vol. PAS-97, no. 4, pp. 1149–1158, Jul. 1978. [Online]. Available: http://ieeexplore.ieee.org/lpdocs/epic03/wrapper.htm?arnumber=4181542

[60] C. Kravaris and J. H. Seinfeld, "Identification of spatially varying parameters in distributed parameter systems by discrete regularization," *Journal of mathematical analysis and applications*, vol. 119, no. 1, p. 128–152, 1986.

[61] A. Küchler, *Hochspannungstechnik: Grundlagen - Technologie - Anwendungen*, 3rd ed. Heidelberg: Springer, 2009. [Online]. Available: http://site.ebrary.com/id/10313511

[62] K. Küpfmüller, *Theoretische Elektrotechnik. Eine Einführung*. Berlin; Heidelberg: Springer, 2008. [Online]. Available: http://d-nb.info/989924491/34

[63] K. Langeheinecke, P. Jany, and G. Thieleke, *Thermodynamik für Ingenieure*. Wiesbaden: Vieweg + Teubner, 2011.

[64] M. Lat, "Thermal properties of metal oxide surge arresters," *Power Apparatus and Systems, IEEE Transactions on*, vol. PAS-102, no. 7, pp. 2194–2202, 1983.

[65] G. Lehner, *Elektromagnetische Feldtheorie für Ingenieure und Physiker*. Berlin: Springer-Verlag, 2006. [Online]. Available: http://site.ebrary.com/id/10228862

[66] R. Lerch, *Elektrische Messtechnik. Analoge, digitale und computergestützte Verfahren*, 4th ed. Berlin, Heidelberg: Springer-Verlag Berlin Heidelberg, 2007.

[67] L. M. Levinson and H. R. Philipp, "The physics of metal oxide varistors," *Journal of Applied Physics*, vol. 46, no. 3, p. 1332, 1975. [Online]. Available: http://link.aip.org/link/JAPIAU/v46/i3/p1332/s1&Agg=doi

[68] C. A. Mack, "Fifty years of Moore's law," *Semiconductor Manufacturing, IEEE Transactions on*, vol. 24, no. 2, p. 202–207, 2011.

[69] G. D. Mahan, L. M. Levinson, and H. R. Philipp, "Single grain junction studies of ZnO varistors – theory and experiment," *Applied Physics Letters*, vol. 33, no. 9, p. 830, 1978. [Online]. Available: http://link.aip.org/link/APPLAB/v33/i9/p830/s1&Agg=doi

[70] H.-J. Martin, *Die Ferroelektrika*, ser. Technisch Physikalische Monographien. Leipzig: Akademische Verlagsgesellschaft Geest & Portig K.-G., 1964, vol. 15.

[71] M. Matsuoka, "Nonohmic properties of zinc oxide ceramics," *Japanese Journal of Applied Physics*, vol. 10, no. 6, pp. 736–746, Jun. 1971.

[72] M. Matsuoka, "Development of zinc oxide varistor-ceramic surge absorber, its nativity and growing process," *Hoden Kenkyu*, vol. 48, no. 3, p. 5–17, 2005.

[73] J. C. Maxwell, "A dynamical theory of the electromagnetic field," *Philosophical Transactions of the Royal Society of London*, vol. 155, no. 0, pp. 459–512, Jan. 1865. [Online]. Available: http://rstl.royalsocietypublishing.org/cgi/doi/10.1098/rstl.1865.0008

[74] D. McHenry, "A lattice analogy for the solution of stress problems," *Journal of the ICE*, vol. 21, no. 2, pp. 59–82, 1943.

[75] A. Mizuno, H. Dewa, T. Taniuchi, H. Tomizawa, H. Hanaki, and E. Hotta, "Multiple beam envelope equations for electron injectors using a bunch segmentation model," *Physical Review Special Topics - Accelerators and Beams*, vol. 15, no. 6, Jun. 2012. [Online]. Available: http://link.aps.org/doi/10.1103/PhysRevSTAB.15.064201

[76] M. Modest, *Radiative Heat Transfer*, ser. Chemical, Petrochemical & Process. Academic Press, 2003.

[77] G. E. Moore, "Cramming more components onto integrated circuits," *Electronics*, vol. 38, no. 8, pp. 114–117, 1965.

[78] T. N. Narasimhan, "Fourier's heat conduction equation: History, influence, and connections," *Reviews of Geophysics*, vol. 37, no. 1, p. 151, 1999. [Online]. Available: http://www.agu.org/pubs/crossref/1999/1998RG900006.shtml

[79] J. A. Nelder and R. Mead, "A simplex method for function minimization," *The Computer Journal*, pp. 308–313, 1965.

[80] X.-M. Pan, W.-C. Pi, M.-L. Yang, Z. Peng, and X.-Q. Sheng, "Solving problems with over one billion unknowns by the MLFMA," *Antennas and Propagation, IEEE Transactions on*, vol. 60, no. 5, p. 2571–2574, 2012.

[81] P. Pinceti and M. Giannettoni, "A simplified model for zinc oxide surge arresters," *Power Delivery, IEEE Transactions on*, vol. 14, no. 2, pp. 393–398, 1999. [Online]. Available: 10.1109/61.754079

[82] W. Polifke and J. Kopitz, *Wärmeübertragung : Grundlagen, analytische und numerische Methoden*. München [u.a.]: Pearson, 2005.

[83] F. Rapetti and G. Rousseaux, "On quasi-static models hidden in Maxwell's equations," *Applied Numerical Mathematics*, Dec. 2012. [Online]. Available: http://linkinghub.elsevier.com/retrieve/pii/S0168927412002036

[84] M. Reinhard, "Experimentelle Untersuchungen zum Einzelimpulsenergieaufnahmevermögen von Metalloxidwiderständen eingesetzt in Hochspannungsnetzen unter Berücksichtigung eines komplexen Fehlerkriteriums," Ph.D. dissertation, TU Darmstadt, Aug. 2008.

[85] K. G. Ringler, P. Kirkby, C. C. Erven, M. V. Lat, and T. A. Malkiewicz, "The energy absorption capability and time-to-failure of varistors used in station-class metal-oxide surge arresters." *IEEE Transactions on Power Delivery*, vol. 12, no. 1, pp. 203–212, Jan. 1997.

[86] E. Sakshaug, J. Kresge, and S. Miske, "A new concept in station arrester design," *IEEE Transactions on Power Apparatus and Systems*, vol. 96, no. 2, pp. 647–656, Mar. 1977. [Online]. Available: http://ieeexplore.ieee.org/lpdocs/epic03/wrapper.htm?arnumber=1601978

[87] T. B. A. Senior and Institution of Electrical Engineers, *Approximate boundary conditions in electromagnetics*. London: Institution of Electrical Engineers, 1995.

[88] P. Silvester, "A general high-order finite-element analysis program waveguide," *IEEE Transactions on Microwave Theory and Techniques*, vol. 17, no. 4, pp. 204–210, Apr. 1969. [Online]. Available: http://ieeexplore.ieee.org/lpdocs/epic03/wrapper.htm?arnumber=1126932

[89] K. Simonyi, *Foundations of Electrical Engineering. Fields-Networks-Waves*, 1st ed. Oxford: Pergamon Press, 1963.

[90] B. C. Steele, Ed., *Electrical Ceramics*. British Ceramic Society, 1985.

[91] T. Steinmetz, G. Wimmer, and M. Clemens, "Numerical simulation of transient electro-quasistatic fields using advanced projection techniques," *Advances in Radio Science*, vol. 4, pp. 49–53, 2006. [Online]. Available: www.adv-radio-sci.net/4/49/2006/

[92] R. Süße, P. Burger, U. Diemar, B. Marx, and T. Ströhla, *Theoretische Grundlagen der Elektrotechnik 1*. Wiesbaden: B.G. Teubner Verlag, 2005.

[93] R. Süße and B. Marx, *Theoretische Elektrotechnik. Band 5: Elektrische Netzwerke - Berechnung und Synthese von Schaltungen für vorgegebenes Bifurkationsverhalten*. Ilmenau: Wissenschaftsverlag Ilmenau, 2002, vol. 5.

[94] A. Taflove, *Computational electrodynamics: the finite-difference time-domain method*. Boston: Artech House, 1995.

[95] ——, *Computational electrodynamics: the finite-difference time-domain method*, 3rd ed., ser. Artech House antennas and propagation library. Boston: Artech House, 2005.

[96] M. Tao, B. Ai, O. Dorlanne, and A. Loubiere, "Different "single grain junctions" within a ZnO varistor," *Journal of Applied Physics*, vol. 61, no. 4, p. 1562, 1987. [Online]. Available: http://link.aip.org/link/JAPIAU/v61/i4/p1562/s1&Agg=doi

[97] L. T. Tenek and J. H. Argyris, *Finite element analysis for composite structures*, ser. Solid mechanics and its applications. Dordrecht ; Boston: Kluwer Academic Publishers, 1998, no. 59.

[98] L. N. Trefethen and D. Bau, *Numerical linear algebra*. Philadelphia: Society for Industrial and Applied Mathematics, 1997.

[99] U. van Rienen, *Numerical methods in computational electrodynamics : linear systems in practical applications*. Berlin; New York: Springer, 2001.

[100] D. Weida, T. Steinmetz, and M. Clemens, "Electro-quasistatic high voltage field simulations of large scale insulator structures including 2-d models for nonlinear field-grading material layers," *IEEE Trans. Magn.*, vol. 45, no. 3, pp. 980–983, Mar. 2009. [Online]. Available: http://ieeexplore.ieee.org/lpdocs/epic03/wrapper.htm?arnumber=4787325

[101] T. Weiland, "A discretization model for the solution of Maxwell's equations for six-component fields," *Archiv Elektronik und Uebertragungstechnik*, vol. 31, pp. 116–120, Mar. 1977.

[102] E. L. Wilson and R. E. Nickell, "Application of the finite element method to heat conduction analysis," *Nuclear Engineering and Design*, vol. 4, no. 3, pp. 276–286, Oct. 1966. [Online]. Available: http://www.sciencedirect.com/science/article/pii/0029549366900513

[103] K. S. Yee, "Numerical solution of initial boundary value problems involving Maxwell's equations in isotropic media," *IEEE Trans. Antennas and Propagation*, pp. 302–307, 1966.

[104] Q.-H. Zhang and D.-J. Chen, "Percolation threshold and morphology of composites of conducting carbon black/polypropylene/EVA," *Journal of Materials Science*, vol. 39, no. 5, pp. 1751–1757, Mar. 2004. [Online]. Available: http://dx.doi.org/10.1023/B%3AJMSC.0000016180.42896.0f

[105] Z. Zheng, S. A. Boggs, T. Imai, and S. Nishiwaki, "Computation of arrester thermal stability," *IEEE Trans. Power Delivery*, vol. 25, no. 3, pp. 1526–1529, Jul. 2010. [Online]. Available: http://ieeexplore.ieee.org/lpdocs/epic03/wrapper.htm?arnumber=5477225

[106] O. C. Zienkewicz, R. Taylor, and J. Zhu, *The Finite Element Method. Its Basis & Fundamentals*, 6th ed. Oxford: Elsevier Science & Technology, 2005.

[107] O. C. Zienkiewicz, "The birth of the finite element method and of computational mechanics," *International Journal for Numerical Methods in Engineering*, vol. 60, no. 1, pp. 3–10, 2004.

[108] O. C. Zienkiewicz and Y. K. Cheung, "Finite elements in the solution of field problems," *The Engineer*, vol. 220, no. 6, pp. 507–510, 1965.

Acknowledgements

Lastly, I wish to thank everybody who helped me in one way or another to write this thesis. My particular thanks go to:

- Prof. Dr.-Ing. Thomas Weiland for his invitation to join TEMF and his role as thesis supervisor,
- PD Dr. rer. nat. Erion Gjonaj for his immeasurably valuable advice as tutor,
- Max Tuczek, Sébastien Blatt, Jan Debus and Prof. Dr.-Ing. Hinrichsen at the High Voltage Labs of TU Darmstadt for their contributions and cooperation,
- Prof. Dr.-Ing. Binder and all other colleagues from research group FOR 575,
- Sebastian Schöps, Annette Fröhlcke, Moritz Gorath, Thomas Weiland and many others who were willing to give me moral support,
- Dragos Munteanu, Heike Seiler, Achim Veuskens and Marianne Dorn for ensuring good working conditions,
- all other colleagues for their valuable input, a nice time and many memorable and great moments.

A special thanks goes to my parents and brother.

Darmstadt, Octobre 2014